HYBRID DYNAMIC SIMULATION FOR PERFORMANCE OPTIMIZATION OF LEGGED MECHANISMS

by

DANIEL MONTRALLO FLICKINGER

Presented to the Faculty of the Graduate School of
The University of Texas at Arlington in Partial Fulfillment
of the Requirements
for the Degree of

DOCTOR OF PHILOSOPHY

THE UNIVERSITY OF TEXAS AT ARLINGTON

May 2011

To Oriana, and in memoriam to Jay Lepreau.

ACKNOWLEDGEMENTS

Thank you to Dr. Alan Bowling for his guidance and support in this work. Thanks to the current and former members of the Robotics, Biomechanics and Dynamic Systems laboratory at the University of Texas at Arlington: Adrian Rodriguez, Nesreen Alsmadi, Mahdi Haghshenas, Michael Tadros, Ryan Robertson, George Teng, and Drew Morgan. Thanks to the former members of the robotics and dynamic systems laboratory at the University of Notre Dame: Jeremy Newkirk and David Post. Thanks to Mable and Oriana for their patience and support.

Thank you to my previous advisor, Dr. Mark Minor for his support and continuing encouragement. And thanks to everyone at the Flux research group during my time at the University of Utah, especially David Johnson, Russ Fish, Kirk Webb, Tim Stack, Eric Eide, Rob Ricci, Anton Burtsev, and Jay Lepreau.

Thanks to my advisory committee: Dr. Dereje Agonafer, Dr. Panos Shiakolas, Dr. Kent Lawrence, Dr. Daejong Kim, and Dr. Robert Woods.

Finally, thank you Mary Campbell.

April 15, 2011

ABSTRACT

HYBRID DYNAMIC SIMULATION FOR PERFORMANCE OPTIMIZATION OF LEGGED MECHANISMS

DANIEL MONTRALLO FLICKINGER, Ph.D.

The University of Texas at Arlington, 2011

Supervising Professor: Alan Bowling

Agile locomotion is needed for mobile robots to efficiently navigate challenging terrain. The ability of an agile legged mobile robot to abruptly change trajectory allows it to quickly react to obstacles and successfully operate in environments usually more suited for legged animals. The research presented herein aims to increase the agility and performance of legged robots.

Using hybrid dynamic simulation, novel methods are developed to model the interaction of a legged robot with the ground. In considering robot agility, an accurate model of the events that occur while in contact is needed. Methods are developed to model ground interaction where oblique angled impacts occur, and to address the well known issues with energy consistency when using rigid body models for dynamic systems.

The contact model in this work is investigated with three multibody benchmark cases. A cable driven single leg jumping robot is modeled to research agility. An optimization of the initial posture of the robot, and its effect on jumping performance and agility is presented. Configuration optimization during the stance phase of a non-periodic jumping motion is performed, utilizing the directional dynamic capability equations. This optimiza-

tion maximizes the time the mechanism is in contact with the ground, minimizes actuation effort, and reduces the likelihood of slipping and stumbling.

TABLE OF CONTENTS

LIST OF FIGURES

LIST OF TABLES

CHAPTER 1

INTRODUCTION

This research aims to increase the agility of legged robots. Agility in the context of this work is defined as the *ability of a robot to abruptly change its state in a highly controlled manner* to react to a changing, uncertain environment. Robots operating in open environments, such as forests, urban areas, disaster zones, and roadways must be capable of rapidly altering their trajectories to maneuver around obstacles and react to complex, varying terrain. The speed of locomotion is related to agility. The more agile a robot, the faster it can travel through complex terrain. Speed can be a result of agility, but high speed capability does not necessarily make a robot agile.

To understand agility, consider some examples from the animal kingdom. Many animals demonstrate agility when interacting with their environments. For example, large cats routinely outrun and outmaneuver their prey by abruptly changing direction while running through uncertain terrain. Mountain goats are capable of agile locomotion, rapidly climbing ninety percent grades, and utilizing footholds not much larger than their feet while climbing and descending challenging rocky terrain. They must quickly react and continuously change trajectory to avoid falls. Jumping spiders interact with an environment where obstacles are larger than their body size. They must routinely jump long distances to navigate through terrain found in their usual environment. Jumping requires an abrupt change in state in order to achieve the initial velocity required to propel the body upward. When spiders jump, they do so in a controlled manner, landing in a precise location and posture.

The current state of the art in agile robotics significantly lags behind the level of agility present in the animal kingdom. Three general options are currently employed to tra-

verse complex terrain. A fourth alternate option is presented in this work. The first option is a slow, careful method. The robot plans every step and remains quasi-static [1–3]. Robots using this method slowly place feet in desirable footholds, or move at a rate slow enough that dynamics do not dominate the motion. The second option of locomotion through complex terrain uses a brute force approach [4–6]. This method uses a robust robot to traverse challenging areas using high momentum and predefined repeating motions, and methods of recovery when tripping, slipping or stumbling [7]. These systems can be capable of traversing complex terrain, but they lack the ability to abruptly react to alter their trajectories.

The third locomotion option is to avoid challenging terrain altogether by flying or jumping over it. Robots can use slow charging, rapid discharging actuation systems like springs to hop or jump long distances. However, when using this mode of jumping it is difficult to control the trajectory. This uncontrollability reduces the system's agility. Jumping robots typically leap long distances to clear single obstacles, or minimize the amount of interaction with challenging terrain.

The alternate option of locomotion is to move through challenging terrain in an agile manner. Agile robots efficiently traverse rough terrain, outperforming the cautious or brute force approaches. Without quasi-static assumptions, agile robots move quicker through challenging terrain, and dispense with computationally intensive planning algorithms. Agile robots also avoid slips and falls, compared to non-agile robots. Robots that use agile locomotion can be designed to have less bulk compared to robots designed for brute force approaches, saving energy and increasing overall capability.

Research into agility requires the simulation of systems of interconnected rigid bodies experiencing simultaneous multiple point contact with terrain. Hard impact and contact is considered in this work, where surface deformation is negligible. Consideration is made for Coulomb friction and energy consistency. The focus of this research is to use the theory developed here to build a simulation with the characteristics of impact and contact, such as

slip transitions and changing contact states. A reasonably accurate representation of these characteristic behaviors in the modeled system supports research into the agility of legged robots. The intent of this research is to produce a more dynamically consistent, mathematically valid, model of contact an impact than currently exists in the literature of multibody dynamics.

Dynamic simulation is used in this work to investigate agile locomotion because it speeds development as compared to implementation on actual robotic hardware. Agility is determined by the ability of the robot to use ground contact and impact to accelerate itself. The interaction of a mechanism with the ground is referred to as contact dynamics. The dynamic simulation must utilize a *dynamically consistent* model of contact and impact that addresses sticking and slipping for multiple contact points with friction. Two types of dynamic inconsistencies have been addressed in this work: 1) energy gains because of arbitrary choice of coefficients of restitution, and 2) infeasible post-impact velocities attributable to an arbitrary choice of coefficients of friction.

Even though current models contain these dynamic inconsistencies, they are still widely-accepted and widely-used because they provide a reasonable approximation of reality. The goal of this work is to provide some remedy for the inconsistencies discussed above. It is not expected that these methodologies will be exact, but that they will correct the mathematical issues in the current methods which should lead to a reasonable approximation of experimentally observed behaviors during contact and impact. Simulations are run to test whether the methods discussed in this work predict the expected, physically-meaningful behavior of the system; however, experimental validation is not pursued here.

A discrete algebraic approach to modeling contact and impact is used in this work. Current algebraic methods utilize the complementarity conditions along with a coefficient of restitution which is often arbitrarily chosen. It is commonly known in the field of multibody dynamics that this approach can lead to kinetic energy gains from an impact

event [8–15]. This represents a dynamic inconsistency because it is generally accepted that an impact event does not increase the total energy of a system of interconnected rigid bodies. This assumption is especially true for terrestrial locomotion where impact with the ground accounts for the largest loss of energy in the system. To ameliorate these energy gains, a method for attenuating post impact velocities was developed and is presented in Chapter 5.

A particular case when current methods for discrete impact modeling yield infeasible post-impact velocities is when the impact occurs at an oblique incidence angle. Oblique impacts are commonplace when simulating agile motion, especially jumping. Legs often meet the ground at oblique angles before take-off, and after landing. Assumptions about friction in contact dynamics that consider only perpendicular contact can result in infeasible velocities. Novel methods are presented in this work for modeling oblique impacts of multiple points on multibody mechanisms. Further discussion of oblique impacts is in Chapter 4. Feasible post impact velocities depending on incidence angle are calculated and used to provide a more accurate model of impacting and sliding robot feet.

One active and two passive multibody mechanisms are modeled and simulated to verify the new contact models. These mechanisms are discussed in Chapter 2. A custom simulation system using MATLAB is used in this work. The goal of this system is to model and simulate jumping of a cable actuated, single leg robot in order to investigate its agility.

Legged systems can control translational acceleration only through ground interaction. The efforts that occur during the time in contact, i.e., the stance phase, directly control what occurs during the entire duration of a jump. Once airborne, the trajectory of the center of mass of the system follows a parabolic trajectory which cannot be altered through any action of the robot. It is desired to maximize the duration of the stance phase to increase the control capability. A longer contact duration allows more acceleration to be transformed into a larger initial velocity, yielding a higher or longer jump. The initial posture of a

jumping mechanism can have an effect on the length of the stance phase, and therefore the robot's performance and agility. Animals routinely crouch before jumping or pouncing. This behavior can help maximize the amount of actuator effort available to use for the impending jump. Similarly, a robotic system can move to a posture that maximizes acceleration capability to improve jumping performance.

The development of a computer based hybrid dynamic simulation is given in Chapter 2. In this chapter, the dynamic equations of motion for a system of interconnected bodies are introduced. The methods to create dynamic simulations of multibody systems are discussed. Three multibody dynamic system models are introduced, with system parameters and diagrams. The implementation and computational performance of the simulations discussed in this work is also presented.

The development of the contact model is discussed in Chapter 3. Beginning with the complementarity conditions, an impact law is realized, which is used to obtain a solution for contact forces. Preliminary simulation results with the planar dynamic systems are presented and discussed.

The development of a solution for post impact forces is also discussed in Chapter 3. The results of this development are demonstrated again with the planar system models.

The modeling of oblique impacts is discussed in Chapter 4. The development of an energy dissipation principle is introduced, and demonstrated with oblique impacts of a multiple contact planar system model. A method to optimize post impact tangential velocities on this system is discussed in detail.

Energy consistency in simulation is discussed in Chapter 5. A method to handle increases in kinetic energy during simulation is introduced. This work addresses a known problem with the application of the contact modeling discussed in Chapter 3. Further development to address the energy consistency problem is addressed, integrating the solution

into the post impact velocity solution discussed in Chapter 4. Simulation results showing the performance of these energy limiting methods are also presented.

Agility through configuration optimization is discussed in Chapter 6. Methods to maximize the possible acceleration of a mechanism by changing the initial posture of a robot are introduced. A summary of this research and future work is in Chapter 7.

CHAPTER 2

HYBRID DYNAMIC SIMULATION

Computer simulations are commonly used to solve dynamic equations for multibody systems where impact is involved [16, 17]. Hybrid dynamic systems are continuous systems that have discrete state changes. Simulated models of multibody systems are used in this work to research agility. These systems have continuously changing states, but at impact events, a discontinuity in states is present. The simulation discussed in this chapter addresses this discontinuity, and the following chapters discuss the calculation of the discrete state changes during impacts.

As agility is dependent on robot ground interaction, the simulation of contact and impact is needed. This chapter details the simulation of rigid body impact dynamics, including an overview of the numerical integration used in this work. Event based, adaptive integration is used to determine the dynamics of the system, especially near times where contact states change.

Three models are used for analysis in this research: a planar double pendulum as a benchmark system in Section 2.3, a planar bicycle system to research multiple point contact, impact, and rolling, in Section 2.4. And, a single leg jumping robot to research agility, acceleration capability, and jumping performance, in Section 2.5. Discussion concerning the implementation of these models in MATLAB is presented in Section 2.6.

2.1 Rigid Body Impact Dynamics

Determination of contact forces is a widely used approach in impact and contact simulation [18–20]. The approach used in this research is most similar to that in [21],

which examined a Newton-Euler formulation for non-colliding contact at multiple points between multiple unconnected rigid bodies. The difference in the work presented here is in the examination of collisions involving impact and contact for systems of interconnected rigid bodies. The goal is to determine the post-impact forces required to achieve desired post-impact accelerations.

Resolving the effects of contact and impact involves the use of the equations of motion:

$$A(\mathbf{q})\,\ddot{\mathbf{q}} \;+\; \mathbf{b}(\mathbf{q},\dot{\mathbf{q}}) \;+\; \mathbf{g}(\mathbf{q}) \;=\; J^{T}(\mathbf{q})\,\mathbf{F} \;+\; \Gamma \tag{2.1}$$

where $\mathbf{q} \in \mathbb{R}^{n}$ contains the generalized/joint coordinates and $\dot{\mathbf{q}}$ and $\ddot{\mathbf{q}}$ contain their time derivatives, generalized speeds and accelerations. Terms $\mathbf{b} \in \mathbb{R}^{n}$, $\mathbf{g} \in \mathbb{R}^{n}$, $\mathbf{F} \in \mathbb{R}^{p}$, and $\Gamma \in \mathbb{R}^{n}$ are the velocity, gravity, impact and/or contact, and other forces where $p \leq n$. Terms $J^{T} \in \mathbb{R}^{n\times m}$ and $A \in \mathbb{R}^{n\times n}$ are the Jacobian and inertia matrices respectively.

The contact and impact forces in (2.1) are

$$J^{T}\,\mathbf{F} \;=\; J^{T}\,P \begin{bmatrix} \mathbf{F}_{p} + \mathbf{F}_{pc} \\ \\ \mathbf{F}_{cc} \end{bmatrix} \;=\; J^{T}\,\mathbf{F}_{c} \;+\; J_{p}^{T}\,\mathbf{F}_{p} \tag{2.2}$$

where $\mathbf{F}_{p} \in \mathbb{R}^{p}$, $\mathbf{F}_{cc} \in \mathbb{R}^{c}$, $\mathbf{F}_{c} \in \mathbb{R}^{m}$ ($m = p + c \leq n$) contain impact and contact forces and P is a permutation matrix; $\mathbf{F}_{pc}$ contains the contact forces associated with the impact points [22].

The following developments rely heavily on the dual nature of the Jacobian which expresses a relationship between forces and velocities [23]:

$$\vartheta = \begin{bmatrix} \boldsymbol{\nu}_{1} \\ \boldsymbol{\omega}_{1} \\ \vdots \end{bmatrix} = J\,\dot{\mathbf{q}}\,, \quad \mathbf{F} = \begin{bmatrix} \mathbf{f}_{1} \\ \mathbf{m}_{1} \\ \vdots \end{bmatrix} = \begin{bmatrix} \mathbf{f}_{t_{1}} \\ f_{n_{1}} \\ \mathbf{m}_{t_{1}} \\ m_{n_{1}} \\ \vdots \end{bmatrix} \tag{2.3}$$

$$\dot{\vartheta} = \dot{J}\,\dot{q} + J\,\ddot{q}\,. \tag{2.4}$$

The terms $v_i \in \mathbb{R}^3$ and $f_i \in \mathbb{R}^3$ are the translational velocity of, and force acting at the i^{th} impact point, while $\omega_i \in \mathbb{R}^3$ and $m_i \in \mathbb{R}^3$ are the rotational velocity of, and the moment acting on the body containing the i^{th} impact point. The 't' and 'n' subscripts indicate forces, velocities, and accelerations normal and tangential to the impacting surface. One of the key elements in determining the behavior at the impact points is the complementarity conditions which are discussed in Section 3.1.

2.2 Event Based Adaptive Integration

In this work contact is treated as a succession of impacts so that they both can be addressed using the same framework [22]. An event-based numerical integration scheme is used which can distinguish between impact and contact. When an impact event occurs, the simulation is stopped, the post-impact velocities are resolved, and the simulation is restarted using the new velocities as initial conditions. This process is illustrated in Figure 2.1. The details of this algorithm are discussed in [24, 25]. In order to illustrate the methods discussed in the following chapters, impact between a system of interconnected rigid bodies and an immobile surface is considered. The method can be extended to moving bodies by determining expressions for their relative motion.

The program flow to calculate post-impact velocities is illustrated in Figure 2.2. The solution for tangential velocities for impacts at oblique angles is discussed in Chapter 4. The method of enforcing energy consistency through velocity attenuation is discussed in Chapter 5.

2.3 Benchmark Example: Double Pendulum

This example is meant as a benchmark case to show that the methods in this work produce expected characteristic behaviors. The double pendulum presents a useful benchmark case to test that the mechanism transitions from slipping to sticking and eventually comes to rest. The stick-slip transition is a major characteristic behavior of dynamic systems in contact. Systems simulated with methods that neglect this transition typically do not come to rest, and are subject to Painlevé's paradox. The paradox is likened to *getting chalk to screech on a blackboard* [26]. If the discontinuity in friction between slipping and sticking is not considered, the solution for the post-impact velocities can become infeasible. The paradox is resolved in this work through the use of a discontinuity in the coefficient of friction to transition between slipping and sticking. The methods discussed in Chapter 4 find feasible velocities and coefficients of friction to further address this problem.

The parameters of the double pendulum simulation are given in Table 2.1. The integrator step is not a time value for a fixed step integrator, but the maximum time interval to save system states as output. A value of 1 is chosen for e_* to enforce that kinetic energy after an impact is less than or equal to the kinetic energy before impact.

2.4 Multiple Contact Example: Planar Bicycle

The bicycle system shown in Figure 2.4 is used here to illustrate the method developed in the previous sections. Gravity acts downward in the -$\mathbf{N}_2$ direction. A slender rod, body 'B', is pin connected to the two circular bodies, 'C' and 'D', at their mass centers; bodies 'C' and 'D' are identical. The mass center of the rod is located at point 'B_o' and the standard formulas for its moments of inertia are used. The standard moments of inertia for circular bodies are also used. The physical properties of the bicycle are given in Table 2.2. The step size was reduced in order to possibly catch some events that the MATLAB event

Table 2.1. Physical properties of the double pendulum system

Parameter	Value
μ_s	0.74
μ_d	0.57
L_1	1.0 meters
L_2	1.0 meters
L_3	1.5 meters
Width of bars	0.05 meters
Depth of bars	0.01 meters
ρ	8080 kg / m^3 (steel)
M_A	4.04 kg
M_B	4.04 kg
ν_s	10^{-5} m / s
α	1
Integrator step	0.01 seconds
Absolute integrator error	10^{-9}
Relative integrator error	10^{-8}

function might miss, a larger step could have been used. The two wheels are pin-connected to the bar through their mass centers, points C_o and D_o. Their rotation is measured by the generalized coordinates q_4 and q_5. The position vector $\mathbf{P}_{OB_o}$ points from 'O' to 'B_o'. Both wheels are identical.

Table 2.2. Physical properties and parameters for bicycle simulations

Parameter	Value
d	1 meter
h	10 meters
L_1	1 meter
m_B	1 kilogram
m_C	2 kilograms
m_D	2 kilograms

The bicycle simulations are similar to those of the double pendulum in Section 2.3. The contact points on the wheels are indicated regardless of whether the wheels are in contact or not. The plotted trajectory corresponds to the geometric center of the rigid bar connecting the two wheels. Again, estimates of the impact forces are used only to indicate where an impact event occurred. The bicycle is only drawn when there is an impact event and the simulation is stopped and restarted, plus at the initial and final configurations.

2.5 Three Dimensional Example: Jumping Leg

A dynamic model of a legged robot is presented in this work to research agility. The model was created using Autolev [27], and simulated using MATLAB. The example presented in this paper is of a one-legged hopping robot. This mechanism is a single leg of a quadruped robot. The system is evaluated to analyze the jumping performance of a less complex mechanism with fewer degrees of freedom.

The jumping leg presented in Figure 2.5 consists of a main body containing three motors. These motors drive three leg segments through cables. The effects of the rotating mass of the motors are built in to the model. Connected to the body in series are the coxa, femur, and tibia. Selected physical properties of the jumping leg model are given in Table 2.3. A single contact point at the distal end of the tibia is considered in the model. This contact point has three associated forces, but no moments. The robot is in hard contact with the ground at the distal end of the tibia, meaning that there is no penetration of the surface or deformation of the bodies.

The body has a full six degrees of freedom, which correspond to the configuration parameters q_1 through q_6. The first three configuration parameters, q_1, q_2, and q_3 are the translations of the center of mass of the body, in N_1, N_2, and N_3 respectively. The rotations q_4, q_5, and q_6 are rotations of the body about axes N_1, N_2, and N_3 respectively.

The configuration parameters q_7, q_8, and q_9 describe motor rotations for actuators driving the coxa, femur, and tibia. As the legs are cable driven, actual joint rotation angles depend on pulley ratios. Torsion springs at each joint are modeled to add compliance to the system to aid numerical integration and moderately control the angles of the leg during the passive flight phase of the jump.

Table 2.3. Physical properties of jumping leg model

Body	Parameter	Value
Body	mass	0.1 kg
Motors	rotating mass	0.004 kg
Coxa	mass	0.018 kg
	axial length	0.03 m
	spring constant	5.0 N-m / radian
	spring zero position	0
Femur	mass	0.024 kg
	axial length	0.0646 m
	spring constant	5.0 N-m / radian
	spring zero position	$5\pi/36$
Tibia	mass	0.022 kg
	axial length	0.09 m
	spring constant	5.0 N-m / radian
	spring zero position	$-\pi/4$

2.6 Implementation

All models discussed in this chapter were modeled in Autolev [27], then implemented in MATLAB. The dynamic equations generated by Autolev were used to create machine generated MATLAB code, which was subsequently modified and extended to in-

clude contact modeling and data logging. The MATLAB functions fmincon and ode45 are used for optimization and integration respectively.

Table 2.4 gives the computation times for the simulation results presented in this work. All simulation runs were on a 64 bit Linux system with 8 Intel Xeon processors running at 2 GHz and with 8 GB of RAM. The CPU times given were reported by the cputime MATLAB command.

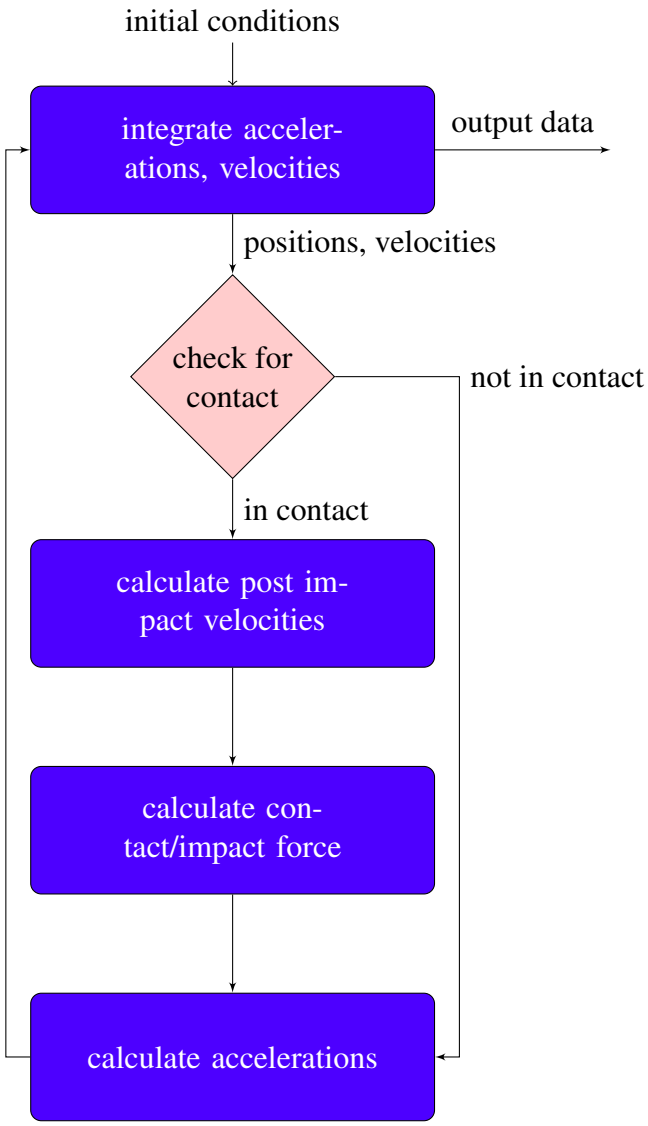

Figure 2.1. Calculating the post impact velocities.

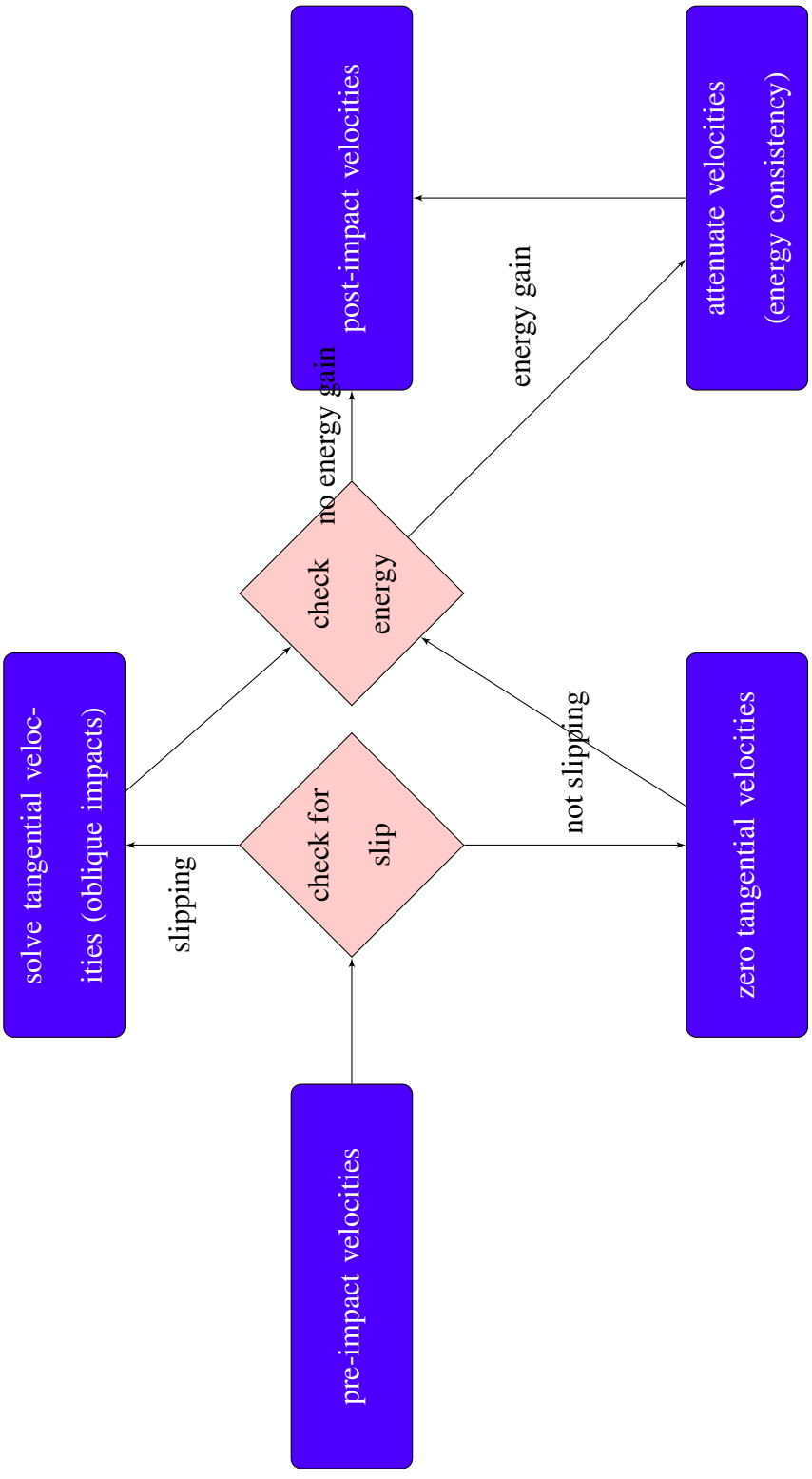

Figure 2.2. Calculating the post impact velocities

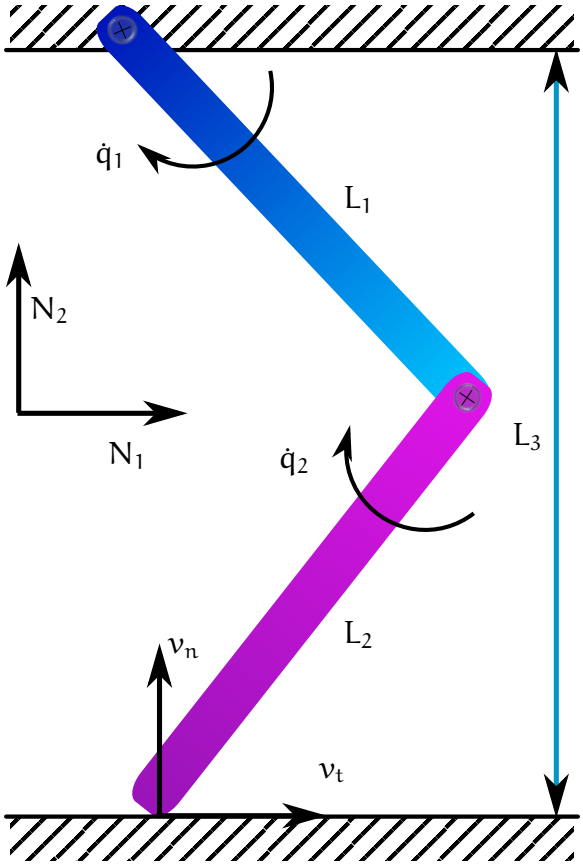

Figure 2.3. Double pendulum system.

$$r_{OB_o} = q_1 \mathbf{N}_1 + q_2 \mathbf{N}_2$$

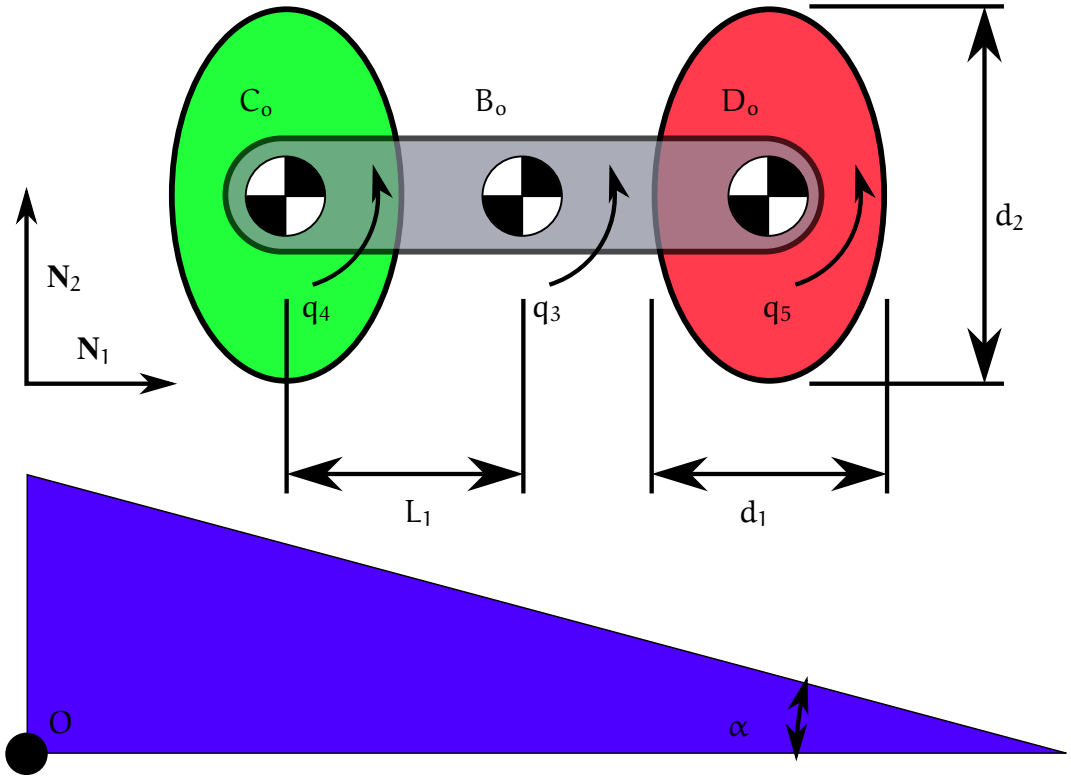

Figure 2.4. Bicycle-like System.

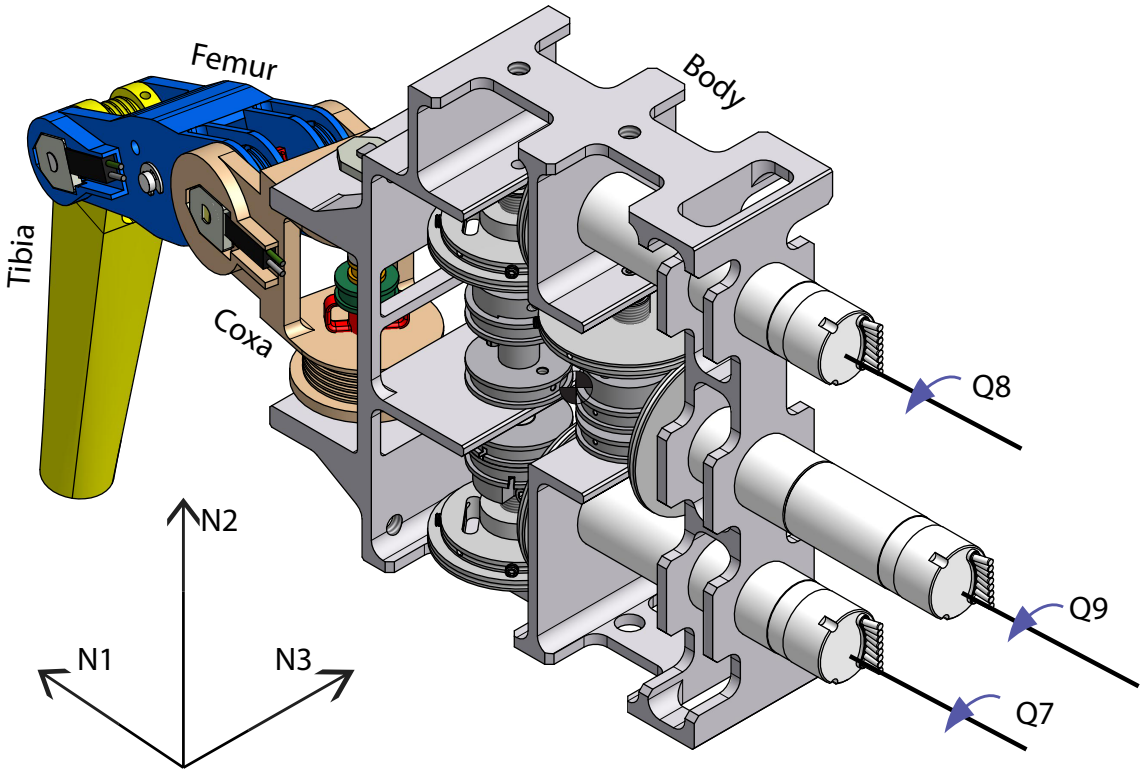

Figure 2.5. Jumping leg robot.

Table 2.4. Execution time for all simulations

Simulation	Section	CPU time	
Double pendulum with no energy control	Section 3.4.1	849.45	
Double pendulum with low COR	Section 3.6.1	490.86	
Double pendulum with minimum energy control	Section 5.2.1	54.32	
Double pendulum moderate energy control	Section 5.2.2	67.04	
Double pendulum moderate energy control, low COR	Section 5.2.3	63.88	
Double pendulum, with velocity attenuation	Section 5.5	91.42	
Double pendulum, with energy constraint	Section 5.5	244.73	
Bicycle oblique impacts, $\alpha = 0$	Section 4.2	89.96	
Bicycle oblique impacts, $\alpha = 15$	Section 4.2	30.71	
Bicycle oblique impacts, $\alpha = 30$	Section 4.2	29.61	
Bicycle oblique impacts, $\alpha = 45$	Section 4.2	406.05	
Bicycle with no energy control	Section 3.4.2	416.70	
Bicycle with high COR	Section 3.7.1	69.11	
Bicycle with moderate COR	Section 3.7.2	580.33	
Bicycle with low COR	Section 3.7.3	1321.12	

CHAPTER 3

CONTACT MODELING

The interaction of multiple bodies with the ground is termed *contact modeling*. In this text it is defined as a body touching the surface of the ground. A force is present at the point where body and ground are coincident. Velocities at contact points are constrained.

Impact is defined as contact with abrupt velocity changes. Impacts are considered as either elastic, or inelastic. Elastic impacts result in a rebound, where the impacting body is only in contact for an instant. Fully inelastic impacts result in a transition to contact after impact. Hard impact is considered in this work, where deformation of impacting bodies and surfaces is negligible.

A distinction is made between impact forces of short duration and contact forces of long duration relative to the numerical integration step size. Impulsive forces result from integrating impact forces over the short duration of the impact event. Although it can be argued that impact forces appear to be infinite when examined at the large time scale of the numerical integration [28], they are assumed to be finite if examined at a small time scale.

Contact is treated as a succession of impacts in this work to avoid the need to alter the dynamic equations of the modeled system as contact states change. The consideration of contact as successive impacts allows impact and contact to be modeled within the same framework so that simultaneous contacts and impacts can be addressed. This approach eliminates the need to remove generalized coordinates in order to enforce contact constraints, as is done in [17], which can be an arbitrary process [19]. It also allows contact points to easily alternate between *sticking* and *slipping* tangentially to the surface.

Contact models found in the literature are classified as either continuous, or discrete. In continuous contact models, the penetration of impacting bodies is considered, and a resulting *penalty force* is created. Penalty force models commonly utilize models of stiff springs to represent contact and impact forces [29].

A discrete model is used to avoid the high-frequency vibrations created when stiff springs are used to model hard impacts [30–33]. In a hard impact or contact there is negligible surface deformation, so stiff springs are required if a *continuous* impact modeling approach is followed.

Discrete models can be classified as *differential* or *algebraic*. Differential approaches use an additional numerical integration in impulse space to capture phenomena occurring during the short duration impact event [34, 35]. In order to avoid the added computations, an algebraic approach is developed here. The goal is to define enough equations to algebraically solve for the post-impact velocities. There are multiple ways to do this, see [11, 30], but the methods used in the research presented here are unique.

The work presented in [36–38] is closest to the method used in this research because of the use of rotational, translational, and tangential CORs, in addition to Newton's COR in the normal direction. *Impulse ratios* were also defined in [36–38] to provide a sufficient number of equations to obtain an algebraic solution. These ratios are useful for parameterizing experimental data [39, 40]. However, when used for predictive purposes, they only represent slipping and thus can actually disallow a solution to the problem; see the discussion of Painlevé's problem in [26].

Friction is examined as a *complementarity* problem in Section 3.1, which defines the *complementarity conditions* for sticking and slipping at the impact or contact points in the direction tangential to the surfaces. In conjunction with these conditions, a coefficient of restitution (COR) is used to describe the rebound between surfaces in the direction normal to the surfaces [12, 13, 15, 41, 42]. Complementarity conditions define the conditions un-

der which contact and impact points will stick or slip [43]. When slipping occurs, these relations are insufficient to determine the post-impact velocities unless all impacting points stick. The complementarity conditions used in this work are introduced in Section 3.1.

During pauses in the integration for impacts, the post impact generalized velocities are calculated using complementarity conditions and a dissipation principle. Post impact forces at contact points are calculated, and integration is resumed with the post impact states as initial conditions. The development of an impact law to calculate post impact forces is discussed in Section 3.2, and the calculation of contact forces is discussed in Section 3.3. Baseline results of the contact modeling in simulation are presented in Section 3.4, as applied to the two planar models introduced in Section 2.3 and Section 2.4. Additional work on the determination of impact forces is discussed in Section 3.5, with simulation results in Section 3.6.

3.1 Complementarity Conditions

The complementarity conditions are a well established means for describing the relationships between friction, contact forces, velocities, and accelerations [11]. These states are split into orthogonal pairs, denoted by *normal* and *tangential*. The normal and tangential directions are typically in relation to the contact surface. Assuming that the distance between the impacting points equals zero, the complementarity conditions are dependent on the value of the pre-impact normal velocities and accelerations, $v_{n_i}(t)$ and $\dot{v}_{n_i}(t)$. The complementarity conditions are represented as,

$$\begin{cases} v_{n_i}(t) < 0 & \text{impact or contact} \\ v_{n_i}(t) = 0 \quad \text{and} \quad \begin{cases} \dot{v}_{n_i}(t) \leq 0 & \text{contact} \\ \dot{v}_{n_i}(t) > 0 & \text{separation} \end{cases} \\ v_{n_i}(t) > 0 & \text{separation} \end{cases} \tag{3.1}$$

A transition occurs when the pre-impact normal velocity equals zero. The pre-impact acceleration must be checked to determine whether impact forces will exist.

When the pre-impact normal velocity indicates impact or contact, its post-impact value is

$$v_{n_i}(t+\epsilon) \;=\; -e_{n_i}\, v_{n_i}(t)\;. \tag{3.2}$$

Rebound is modeled by $e_{n_i} \neq 0$. A threshold value of velocity is used herein below which the impact point is considered not to rebound.

According to classical Coulomb friction, the post-impact tangential velocities, $\dot{\boldsymbol{v}}_{t_i}$, satisfy,

$$\begin{cases} \boldsymbol{v}_{t_i} = \mathbf{0} \text{ and } \dot{\boldsymbol{v}}_{t_i} = \mathbf{0} & \text{then} \quad \|\mathbf{f}_{t_i}\| \leq \mu_s\, |f_{n_i}| \\ \boldsymbol{v}_{t_i} = \mathbf{0} \text{ and } \dot{\boldsymbol{v}}_{t_i} \neq \mathbf{0} & \text{then} \quad \|\mathbf{f}_{t_i}\| = \mu_s\, |f_{n_i}| \\ \boldsymbol{v}_{t_i} \neq \mathbf{0} & \text{then} \quad \|\mathbf{f}_{t_i}\| = \mu_d\, |f_{n_i}| \end{cases} \tag{3.3}$$

where μ_s and μ_d are the static and dynamic coefficients of friction [11]. The relations between the tangential and normal friction forces forms a friction cone, shown in Figure 3.1. The friction force vector must lie within the bounds of the cone to avoid slipping. The relationships in (3.1) and (3.3) are the basis for what is referred to as complementarity problem [20]. The complimentary conditions apply to both contact and impact forces independently.

The no-slip condition is defined by the first relation in (3.3), the stick-slip transition is defined by the second, and slipping is defined by the third. In (3.3) there is a discontinuous change in the coefficient of friction, and thus a discontinuous change in the friction forces. The boundary between sticking and slipping is visualized as the friction cone. Other friction models have been proposed which provide a continuous transition between sticking and slipping including the Karnopp model [44, 45].

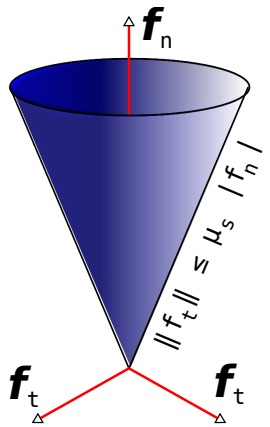

Figure 3.1. Friction cone.

In this work, the impulsive forces are used to check the no-slip condition. The complementarity conditions in terms of impulses are presented in [46],

$$\begin{cases} \boldsymbol{\nu}_{t_i} = \mathbf{0} \text{ and } \dot{\boldsymbol{\nu}}_{t_i} = \mathbf{0} & \text{then} \quad \|\mathbf{p}_{t_i}\| \leq \mu_s \, |p_{n_i}| \\ \boldsymbol{\nu}_{t_i} = \mathbf{0} \text{ and } \dot{\boldsymbol{\nu}}_{t_i} \neq \mathbf{0} & \text{then} \quad \|\mathbf{p}_{t_i}\| = \mu_s \, |p_{n_i}| \quad . \\ \boldsymbol{\nu}_{t_i} \neq \mathbf{0} & \text{then} \quad \|\mathbf{p}_{t_i}\| = \mu_d \, |p_{n_i}| \end{cases} \tag{3.4}$$

Similar complementarity conditions can be developed for moments [47, 48].

Using classical rigid body impact dynamics, the impulsive forces, $\mathbf{p}$, are defined as

$$A \ (\ \dot{\mathbf{q}}(t+\epsilon) \ - \ \dot{\mathbf{q}}(t) \ ) \ = \ J^T \, \mathbf{p} \tag{3.5}$$

assuming that contact is considered as a succession of impacts. Combining (2.2) and (3.5) yields an expression for the impulsive forces:

$$\left(J \, A^{-1} J^T \right)^{-1} \left(\vartheta(t+\epsilon) - \vartheta(t) \right) = \ \mathbf{p} \ = \begin{bmatrix} \mathbf{p}_{t_1} \\ p_{n_1} \\ \vdots \end{bmatrix} \tag{3.6}$$

where $\vartheta(t)$ is known. In addition, it is assumed that the other parameters contained in J and A are also known. Therefore, $\mathbf{p}_{t_i}$ and p_{n_i} are linear functions of the elements in $\vartheta(t+\epsilon)$.

The no-slip case is the only one where all velocities are known; the tangential velocities equal zero. It is enforced using a matrix of normal and tangential CORs [36–40]

$$\vartheta(t+\epsilon) \;=\; E\,\vartheta(t) \tag{3.7}$$

where E is a diagonal matrix with a COR for each velocity in ϑ; $E_{ii} \in \{e_{n_i}, e_{t_{ij}}\}$ are CORs for point i in the directions normal and tangent to the impact surface where $j \in \{1,2\}$. The e_i do not have to be equal, but are considered constant for the duration of the impact. Although $0 \geq e_{n_i} \geq -1$ no such constraint is placed on the tangential COR $e_{t_{ij}}$. The no-slip case is checked by setting $e_{t_{ij}} = 0$.

In the slipping case, the complementarity conditions alone do not yield a unique solution for the forces, velocities, or accelerations [26]. The unilateral and zero-nonzero constraints in the complementarity conditions only define feasible ranges of values for velocities, accelerations, and forces/moments. Additional constraints are required, which are formulated in terms of the dissipation principle discussed in Section 4.1.

Combining (3.11), (3.6), and (3.7) yields a general impact law for determining the post-impact velocities

$$\dot{\mathbf{q}}(t+\epsilon) \;=\; \left[I - \bar{J}\,J\right]\dot{\mathbf{q}}(t) \;+\; \bar{J}\,E\,J\,\dot{\mathbf{q}}(t) \tag{3.8}$$

$$\bar{J} \;=\; A^{-1}J^{T}\left(J\,A^{-1}J^{T}\right)^{-1}\,. \tag{3.9}$$

3.2 Impact Law

Classical rigid body impact dynamics begins with an examination of impulses and momenta. Impulsive forces result from integrating the impact forces over the short duration of the impact event, ϵ. Although it can be argued that impact forces are infinite when examined at the large time scale of the numerical integration [28], they are assumed to be

finite if examined at a small time scale [49]. When contact is considered as a succession of impacts, a definite integration of the dynamic model over a small time period ϵ yields,

$$\int_t^{t+\epsilon} (A\,\ddot{\mathbf{q}} + \mathbf{b}(\mathbf{q},\dot{\mathbf{q}}) + \mathbf{g})\,dt = \int_t^{t+\epsilon} J^T\mathbf{F}\,dt \tag{3.10}$$

where only the impact forces survive:

$$A\,(\,\dot{\mathbf{q}}(t+\epsilon) - \dot{\mathbf{q}}(t)\,) = J^T\,\mathbf{p} \tag{3.11}$$

assuming that contact is considered as a succession of impacts. The unknowns in (3.11) are $\dot{\mathbf{q}}(t+\epsilon)$ and $\mathbf{p}$.

The consideration of contact as successive impacts allows impact and contact to be modeled within the same framework so that simultaneous contacts and impacts can be addressed. This approach eliminates the need to remove generalized coordinates in order to enforce contact constraints, as is done in [17], which can be an arbitrary process [19]. It also allows contact points to alternate between *sticking* and *slipping* tangentially to the surface, without requiring any modifications to the dynamic equations of motion.

Multiplying (3.11) through by the mass matrix inverse yields

$$\dot{\mathbf{q}}(t+\epsilon) - \dot{\mathbf{q}}(t) = A^{-1}J^T\,\mathbf{p} \tag{3.12}$$

which can be an over-constrained system of equations since $m \leq n$. Thus only a subset of all possible $\dot{\mathbf{q}}$ contribute to $\mathbf{p}$. It is assumed that this subset can be expressed in terms of the velocities of the impact points,

$$\vartheta(t+\epsilon) - \vartheta(t) = J\,A^{-1}J^T\,\mathbf{p} \tag{3.13}$$

which gives a one-to-one mapping between the velocities and forces at the impact points.

Substituting (3.7) into (3.13) yields the impulsive forces

$$\left(J\,A^{-1}J^T\right)^{-1}(E-I)\,\underbrace{J\,\dot{\mathbf{q}}(t)}_{\vartheta(t)} = \mathbf{p}\,. \tag{3.14}$$

The coupling between the velocities in $\vartheta(t)$ and the impulses in $\mathbf{p}$ allows for the possibility that impact/contact at one point can affect the state of the other points.

Assuming that the CORs can be determined, combining (3.11) and (3.14) yields

$$\dot{\mathbf{q}}(t+\epsilon) \;=\; \left[I - \bar{J}\,J\right]\dot{\mathbf{q}}(t) \;+\; \bar{J}\,E\,J\,\dot{\mathbf{q}}(t) \tag{3.15}$$

$$\bar{J} \;=\; A^{-1}J^{T}\left(J\,A^{-1}J^{T}\right)^{-1}\;. \tag{3.16}$$

This relation defines the velocities for the entire system. The first term on the right of (3.15) determines the portion of the generalized velocity $\dot{\mathbf{q}}(t+\epsilon)$ not defined by the impact points, those in the null space of J. The second term adds any non-zero post-impact velocities of the impact points, as defined by the COR, to $\dot{\mathbf{q}}(t+\epsilon)$.

The advantage of using the tangential CORs is the clear decomposition of the velocities associated with impact and non-impact points. There are two conditions under which (3.14), and therefore (3.8), is valid

1. J is full rank,
2. $m \leq n$.

If J is not full rank one must determine an independent set of constraints which defines J.

The second condition implies that the number of degrees-of-freedom (DOFs) of the system, n, limits the number of impact points that can be considered using this approach. In general, examination of more than $n/2$ or $n/3$ impact points requires more DOFs, depending on whether the system is planar or spatial. This can be accomplished by examining flexibility or deformation in the system as is done to resolve static indeterminacy in statics and solid mechanics.

In order to determine the CORs, a physically meaningful guess at their values can be made which correspond to sticking. This is the only case where the tangential velocities are known, $\boldsymbol{\nu}_t(t+\epsilon) = \mathbf{0}$ and therefore $e_{t_{ij}} = 0$. The normal CORs have their specified values. The specification of normal CORs assumes that the post-impact motion in the

normal direction is known beforehand. The no-slip condition is checked for correctness using the impulsive forces in (3.14) along with the complementarity conditions.

If any of the impact points slip, then all of the tangential velocities and CORs are unknown; it is incorrect to make any assumptions concerning the state of any impact point. This is because the result was obtained as the simultaneous solution of a system of equations. Therefore altering the state of one impact point may alter all of them. However, this only occurs if the state of each impact point is coupled to every other, as is expected in a system of interconnected bodies.

3.3 Solution for Contact Forces

This solution is only used only for the points in contact, and impact points which do not rebound; it is assumed that rebounding points do not experience a contact force at time $t+\epsilon$. The solution technique is illustrated here with an example. It is assumed that contact point 1 sticks and point 2 slips. The known contact accelerations are included in (4.1) using a selection matrix defined as

$$\dot{\vartheta}_c^* = J\,\dot{\mathbf{q}}^* = \begin{bmatrix} \dot{\boldsymbol{\nu}}_{ct_1}^* \\ \dot{\nu}_{cn_1}^* \\ \dot{\boldsymbol{\nu}}_{ct_2}^* \\ \dot{\nu}_{cn_2}^* \end{bmatrix} = \begin{bmatrix} 0 \\ \mathbf{0} \\ I \\ \mathbf{0} \end{bmatrix} \dot{\boldsymbol{\nu}}_{ct_2}^* = B_1\,\dot{\boldsymbol{\nu}}_{ct_2}^* \tag{3.17}$$

where $B_1 \in \mathbb{R}^{6\times 2}$. If all contact points stick then $B_1 = [\,]$. The known contact forces are included as

$$\mathbf{F}_c = \begin{bmatrix} \mathbf{f}_{ct_1} \\ f_{cn_1} \\ \mathbf{f}_{ct_2} \\ f_{cn_2} \end{bmatrix} = \underbrace{\begin{bmatrix} I & \mathbf{0} & \mathbf{0} \\ \mathbf{0} & 1 & 0 \\ 0 & 0 & -\mu_2 \dfrac{\boldsymbol{\nu}_{t_2}}{\|\boldsymbol{\nu}_{t_2}\|} \\ \mathbf{0} & 0 & 1 \end{bmatrix}}_{B_2} \begin{bmatrix} \mathbf{f}_{ct_1} \\ f_{cn_1} \\ f_{cn_2} \end{bmatrix} \tag{3.18}$$

where $B_2 \in \mathbb{R}^{6\times 4}$. Combining (4.1), (3.17) and (3.18) yields

$$\begin{bmatrix} \dot{\boldsymbol{\nu}}^*_{ct_2} \\ \mathbf{f}_{ct_1} \\ f_{cn_1} \\ f_{cn_2} \end{bmatrix} = \left(M_c^T M_c\right)^{-1} M_c^T \lambda \tag{3.19}$$

$$M_c = \begin{bmatrix} B_1 & -J A^{-1} J^T B_2 \end{bmatrix} \tag{3.20}$$

$$\lambda = J A^{-1} \left(\boldsymbol{\Gamma} - \mathbf{b}(\mathbf{q}, \dot{\mathbf{q}}^*) - \mathbf{g} + J_p^T \mathbf{F}_p\right) + \dot{J}\, \dot{\mathbf{q}}^* \tag{3.21}$$

where $M_c \in \mathbb{R}^{6\times 6}$. The solution should be checked to see if the normal contact forces are positive; see (3.1). These contact forces are substituted back into the equations of motion to obtain the post-impact accelerations.

3.4 Initial Simulation Results

The two planar models discussed in Chapter 2 are tested in simulation to demonstrate the results obtained with the contact modeling introduced in this chapter. The simulations produce data on the positions and velocities of the bodies in the mechanisms, along with data on the contact and impact forces, and energy states. The results presented in this section are preliminary, and do not include the subsequent modeling and calculations discussed in later chapters. The plots here are for systems modeled using techniques already found in the literature. This establishes a baseline in simulation, and highlights the problems that are addressed in this research.

3.4.1 Double pendulum with No Energy Control

The double pendulum system introduced in Section 2.3 is released from rest from a horizontal position as a demonstration of the contact modeling discussed in Section 3.3. The initial configuration for the simulation in this section is given in Table 3.1. The pen-

dulum is drawn only when there is an impact event and the simulation was stopped and restarted, in addition to the initial and final configurations.

Table 3.1. Initial conditions of the double pendulum system

Parameter	Value
q_1	0 (initial)
q_2	0 (initial)
$\dot{q}_1$	0.0 s^{-1} (initial)
$\dot{q}_2$	0.0 s^{-1} (initial)

Figure 3.2 shows several rebounding impacts at the tip of the pendulum and it doesn't come to rest within 10 seconds of simulation time. This case should represent a perfectly elastic collision although energy is still lost to tangential friction forces. However, the energy plot in Figure 3.4 shows that the total system energy increases at least twice during the simulation. The energy-modifying coefficient of restitution introduced in Chapter 5 addresses this situation. These energy increases can cause the estimate of the impact force to go negative, as is evident in Figure 3.3b. Some of the tangential forces in Figure 3.3a are small relative to the large peaks, and do not appear in these plots.

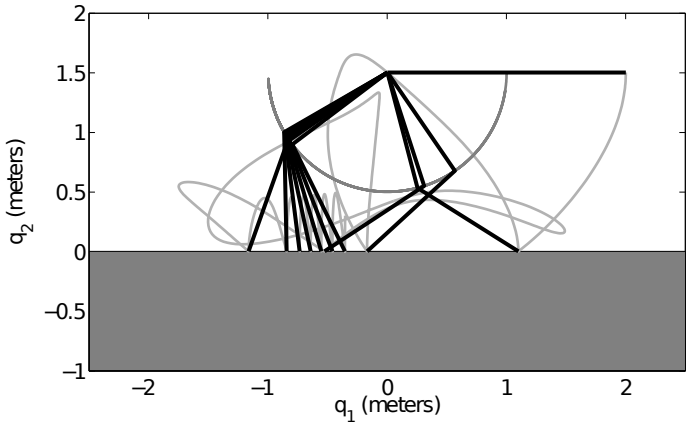

Figure 3.2. Double pendulum trajectory: $e_{n_i} = 1$, $e_* = 5$ (no energy control).

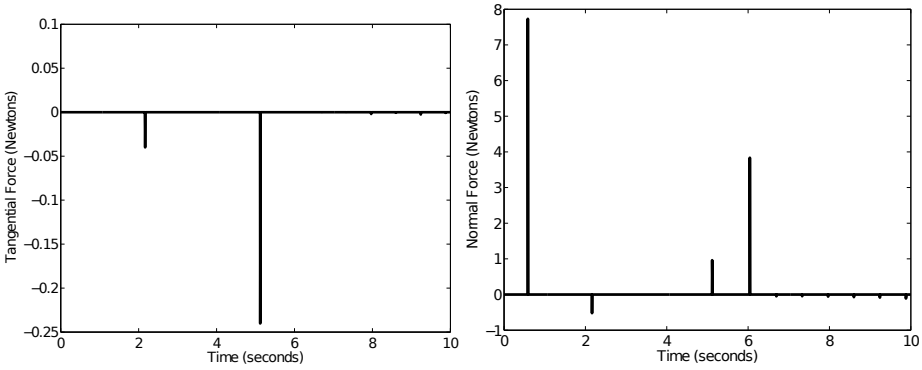

(a) (b)

Figure 3.3. Double pendulum contact forces: $e_{n_i} = 1$, $e_* = 5$, (a) tangential, (b) normal (no energy control).

3.4.2 Bicycle mechanism with No Energy Control

An initial simulation is run with no energy control. The parameters and initial conditions of the simulation are shown in Table 3.2. The resulting trajectory is given in Figure 3.5 which shows the bicycle bouncing but never coming to rest.

The forces corresponding to the series of impacts for both wheels are shown in Figure 3.6a and Figure 3.6b. The key attributes of these plots are in the energy increases shown in Figure 3.7. These will be removed in subsequent simulations using the energy-modifying COR.

3.5 Determination of Impact Forces

Before determining the impact forces, the velocities should be corrected to obtain the desired energy levels so that $\dot{\mathbf{q}}^*$ is used to minimize the impact forces. The velocity correction methods are discussed in Section 5.4 and Section 5.4. An impact force minimization is required to resolve impact forces which cannot be determined solely by the complementar-

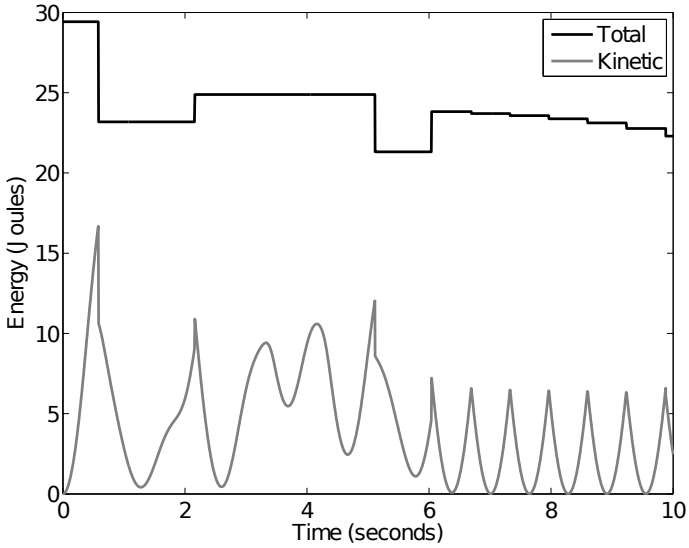

Figure 3.4. Double pendulum energy: $e_{n_i} = 1$, $e_* = 5$ (no energy control).

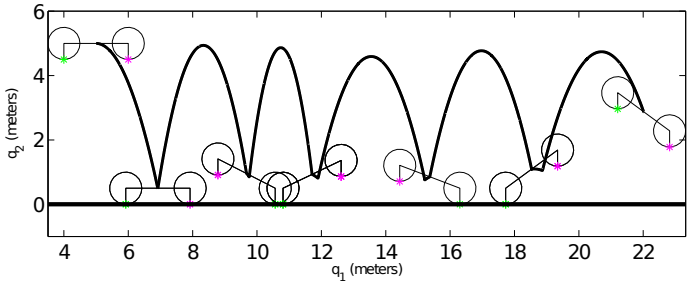

Figure 3.5. Bicycle trajectory: $e_{n_i} = 1.0$, $e_* = 5.0$.

ity conditions. The constraints on the minimization enforce energy consistency using the *Work-Energy Theorem* [50],

$$T(\dot{\mathbf{q}}^*) - T(\dot{\mathbf{q}}(t)) = W_\epsilon = \int_t^{t+\epsilon} J_p^T \, \mathbf{F}_p(t) \cdot \dot{\mathbf{q}}(t) \, dt \, . \tag{3.22}$$

The integration variable can be changed using $d\mathbf{q} = \dot{\mathbf{q}} \, dt$ with a change of limits

$$T(\dot{\mathbf{q}}^*) - T(\dot{\mathbf{q}}(t)) \; = \; \int_{\mathbf{q}(t)}^{\mathbf{q}(t+\epsilon)} J_p^T \, \mathbf{F}_p(t) \cdot d\mathbf{q} \, . \tag{3.23}$$

Table 3.2. Initial conditions for bicycle simulation

Parameter	Value
q_1	5 meters
q_2	5 meters
q_3	0°
q_4	0°
q_5	0°
$\dot{q}_1$	2 meters/second
$\dot{q}_2$	0 meters/second
$\dot{q}_3$	0
$\dot{q}_4$	0
$\dot{q}_5$	0
d_1	0.5 meters
d_2	0.5 meters

However, over this small time interval $\mathbf{q}$ is considered constant so it is not a function of t, and t is not a function of $\mathbf{q}$, therefore

$$\begin{aligned} T(\dot{\mathbf{q}}^*) - T(\dot{\mathbf{q}}(t)) &= J_p^T \left(\mathbf{F}_p(t+\epsilon)\cdot\mathbf{q}(t+\epsilon) - \mathbf{F}_p(t)\cdot\mathbf{q}(t)\right) \\ &= J_p^T\, \mathbf{F}_p(t+\epsilon)\cdot\mathbf{q}(t+\epsilon) \end{aligned} \tag{3.24}$$

since $\mathbf{F}_p(t) = \mathbf{0}$.

When all post-impact velocities are known the following problem is solved to minimize the impact forces

$$\begin{aligned} \min_{\dot{\vartheta}_p^*} \quad & \text{obj} := \mathbf{F}_p^T(t+\epsilon)\ \left(J_p A^{-1} J_p^T\right)\ \mathbf{F}_p(t+\epsilon) \\ \text{subject to} \quad & T(\dot{\mathbf{q}}^*) - T(\dot{\mathbf{q}}(t)) \ =\ \mathbf{q}^T(t+\epsilon)\ J_p^T\, \mathbf{F}_p(t+\epsilon) \\ & 0 \ \leq\ f_{pn_i}\ . \end{aligned} \tag{3.25}$$

Knowing $\dot{\vartheta}_p^*$ and $\dot{\mathbf{q}}^*$ the impact forces are

$$\mathbf{F}_p(t+\epsilon) = \left(J_p A^{-1} J_p^T\right)^{-1} \left(\dot{\vartheta}_p^* - \dot{J}_p\ \dot{\mathbf{q}}^* + J_p\ A^{-1}\dot{A}\ \dot{\mathbf{q}}^*\right)\ . \tag{3.26}$$

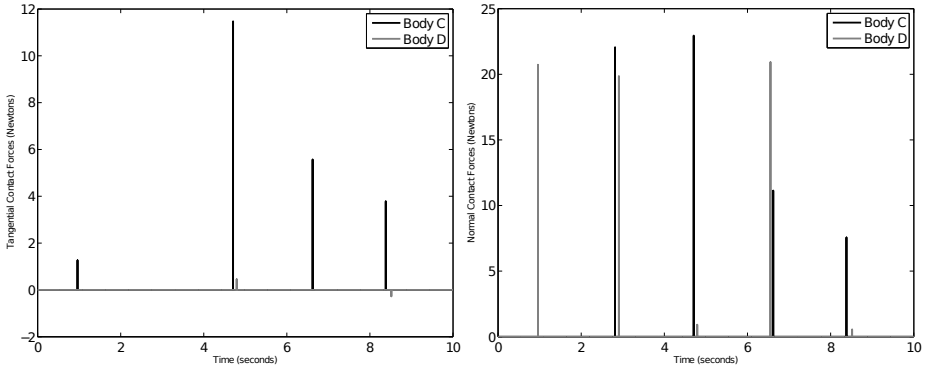

(a) (b)

Figure 3.6. Bicycle contact forces: $e_{n_i} = 1.0$, $e_* = 5.0$, (a) tangential, (b) normal.

These forces are substituted back into the equations of motion, and used to calculate the post-impact accelerations. The integrator restarts with the new states, and the simulation proceeds to the next impact event.

3.6 Impact Analysis of the Double Pendulum System

The benchmark case of the double pendulum is simulated to test the impact force calculations discussed in Section 3.2. The initial conditions of the double pendulum system for the simulation in Section 3.6.1 are given in Table 3.3.

Table 3.3. Physical properties of the double pendulum system

Parameter	**Value**
q_1	0 (initial)
q_2	0 (initial)
$\dot{q}_1$	0.0 s^{-1} (initial)
$\dot{q}_2$	0.0 s^{-1} (initial)

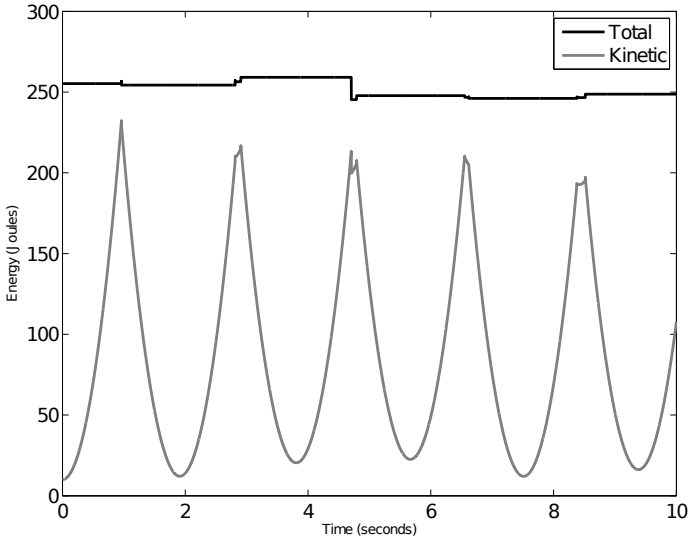

Figure 3.7. Bicycle energy: $e_{n_i} = 1.0$, $e_* = 5.0$.

3.6.1 Double Pendulum with Low Coefficient of Restitution

The coefficient of restitution is set to 0.0, simulating a sticky or muddy surface. The resulting trajectory is given in Figure 3.8a. The mechanism comes to rest shortly after the first impact, with no rebound. The impact and contact forces, and energy are plotted in Figure 3.9b, Figure 3.9a, and Figure 3.8b.

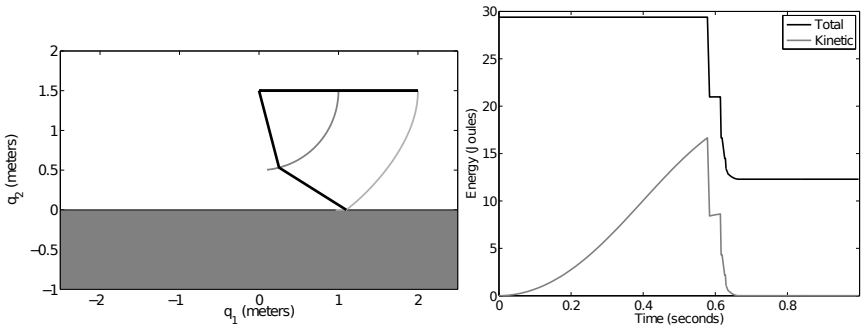

(a) (b)

Figure 3.8. Double pendulum trajectory: $e_{n_i} = 0.0$, $e_* = 0.5$, (a) trajectory, (b) energy.

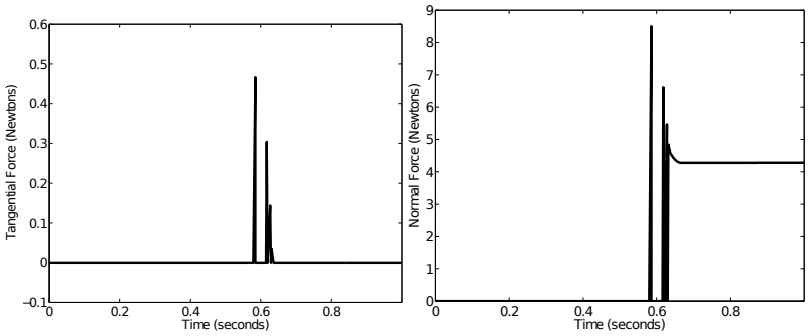

(a) (b)

Figure 3.9. Double pendulum contact forces, $e_{n_i} = 0.0$, $e_* = 0.5$, (a) tangential, (b) normal.

3.7 Impact Analysis of the Planar Bicycle System

The planar bicycle system is simulated to investigate the calculation of post impact velocities and impact forces on a multiple contact system with friction. The results of each simulation run consist of trajectory, contact force, and energy plots. The simulation is run for 5 seconds.

A wedge of slope 20 degrees representing the ground is depicted as a gray region. The coefficient of restitution of the wedge is specified. The bicycle is drawn at the initial and final configurations, and at impact events. The plotted trajectory corresponds to the geometric center of the rigid bar coupling the two masses. The initial conditions and simulation parameters are given for the planar bicycle system in this section in Table 3.4.

The bicycle system is simulated with varying coefficients of restitution, with the results given in Section 3.7.1, Section 3.7.2, and Section 3.7.3.

3.7.1 Bicycle System with High Coefficient of Restitution

The COR is set to 0.75 to approximate an elastic surface. The parameter $e_* = 0.5$ enforces that at least half of all kinetic energy is lost at each impact.

Table 3.4. Initial conditions for bicycle simulation

Parameter	Value
q_1	5 meters
q_2	5 meters
q_3	0°
q_4	0°
q_5	0°
$\dot{q}_1$	0 meters/second
$\dot{q}_2$	0 meters/second
$\dot{q}_3$	0
$\dot{q}_4$	0
$\dot{q}_5$	0
d_1	0.5 meters
d_2	0.25 meters

The trajectory is plotted in Figure 3.10a. The mechanism bounces several times down the wedge, traveling much further than in later tests with lower CORs.

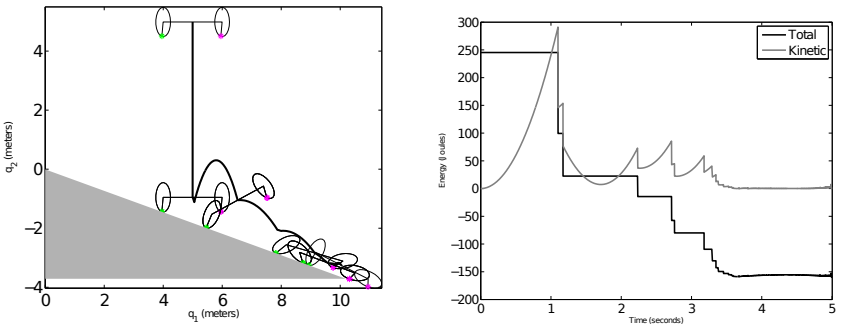

(a) (b)

Figure 3.10. Bicycle simulation with a coefficient of restitution of 0.75, (a) trajectory, (b) energy.

The impact and contact forces are given in Figure 3.11b. The peaks from each impact are shown. The total and kinetic energy are plotted in Figure 3.10b. At each impact, approximately half of the kinetic energy is lost. The energy is regained during the ballis-

tic phases as the bicycle travels down the wedge. After several bounces, the mechanism transitions from rebounding impact to rolling contact. This occurs after approximately 3.5 seconds. The forces given in Figure 3.11 chatter while in rolling contact, hence the solid regions. The chattering is caused by a combination of using a rough approximation of the contact points between the ground and the ellipse shaped wheels of the mechanism, and coarse integrator tolerances set in an effort to reduce computation time.

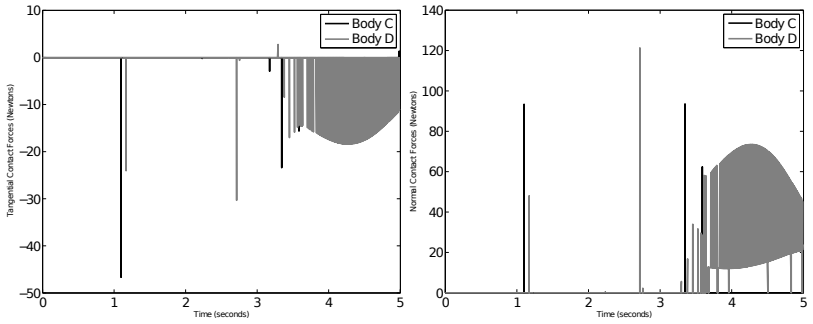

(a) (b)

Figure 3.11. Contact/impact forces for bicycle simulation, $e_{n_i} = 0.75$, (a) tangential, (b) normal.

3.7.2 Bicycle System with Moderate Coefficient of Restitution

The simulation is run with the surface coefficient of restitution decreased to 0.5. The resulting trajectory is shown in Figure 3.12a. The mechanism bounces fewer times than in the previous example. In addition, the transition to rolling contact occurs sooner. The total and kinetic energy is plotted in Figure 3.12b.

The impact and contact forces are given in Figure 3.13. Chattering in the contact forces is again present after the transition of the mechanism from impact to rolling contact.

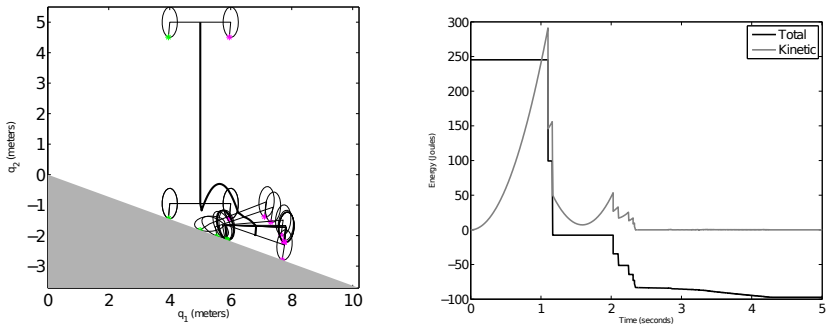

(a) (b)

Figure 3.12. Bicycle simulation with a coefficient of restitution of 0.5, (a) trajectory, (b) energy.

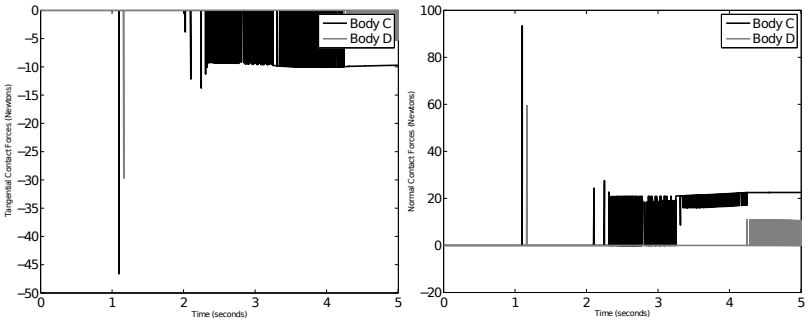

(a) (b)

Figure 3.13. Contact/impact forces for bicycle simulation, $e_{n_i} = 0.5$, (a) tangential, (b) normal.

3.7.3 Bicycle System with Low Coefficient of Restitution

The coefficient of restitution is lowered to 0.25, simulating a soft or sandy surface. The resulting trajectory is given in Figure 3.14a. After the initial impact, the mechanism slides and rolls, coming to rest at a short distance down the wedge. The kinetic and potential energies are plotted in Figure 3.14b. The impact and contact forces, and energy are plotted in Figure 3.15. The chattering during rolling contact is present, as in the previous examples. The magnitudes of the impact forces increase as the COR decreases, as more energy is lost to impact.

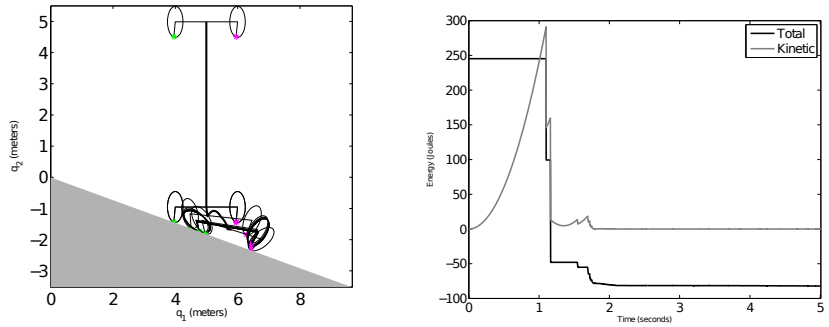

(a) (b)

Figure 3.14. Bicycle simulation with a coefficient of restitution of 0.25, (a) trajectory, (b) energy.

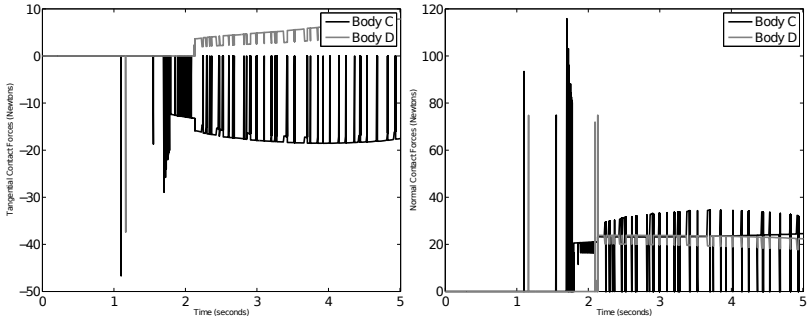

(a) (b)

Figure 3.15. Contact/impact forces for bicycle simulation, $e_{n_i} = 0.25$, (a) tangential, (b) normal.

CHAPTER 4

OBLIQUE IMPACTS

Jumping robots frequently impact the ground at oblique angles. The contact models developed in this research must consider the feasibility of post impact velocities and forces when impacting at oblique angles. Consider the double pendulum system in Figure 2.3, resolving the effects of contact and impact involves the use of the equations of motion, also discussed in Section 2.1:

$$A(\mathbf{q})\,\ddot{\mathbf{q}} \;+\; \mathbf{b}(\mathbf{q},\dot{\mathbf{q}}) \;+\; \mathbf{g}(\mathbf{q}) \;=\; J^{T}(\mathbf{q})\,\mathbf{F} \;+\; \boldsymbol{\Gamma} \tag{4.1}$$

where $\mathbf{q} \in \mathbb{R}^{n}$ contains the generalized/joint coordinates and $\dot{\mathbf{q}}$ and $\ddot{\mathbf{q}}$ contain their time derivatives, generalized speeds and accelerations. Terms $\mathbf{b} \in \mathbb{R}^{n}$, $\mathbf{g} \in \mathbb{R}^{n}$, $\mathbf{F} \in \mathbb{R}^{p}$, and $\boldsymbol{\Gamma} \in \mathbb{R}^{n}$ are the velocity, gravity, impact and/or contact, and other forces where $p \leq n$. Terms $J^{T} \in \mathbb{R}^{n\times m}$ and $A \in \mathbb{R}^{n\times n}$ are the Jacobian and inertia matrices respectively.

The complementarity conditions provide a framework for determining the system's post-impact/contact velocities. However, they only define feasible regions for the post-impact/contact velocities, so some other condition must be imposed in order to resolve the post-impact velocities [26]. This additional condition can be formulated as a dissipation principle that minimizes some quantity, energy dissipated [12, 26] or kinetic energy for example [11, 42, 51].

The difference here is that the dissipation principle in this work considers the feasibility of a priori choices of the coefficients of restitution and friction and determines feasible values if they are not. The regions for slipping and sticking, defined by the static and dynamic coefficients of friction, are dependent on the incidence angle of the impact [52]. In addition, articles in the literature discuss the finding that the COR depends on the orienta-

tion of the impacting bodies [26,53] as well as on vibrations induced by the impact [54,55]. Addressing this feasibility in the dissipation principle ensures that a feasible post-impact velocity can be found which thereby facilitates the simulation of oblique impacts.

In the complementarity problem approach, there are defined regions for sticking, slipping, and the transition between them [14]. The transition region is often referred to as the *stick-slip boundary*. The characteristics of the stick-slip boundary have been debated and new models, both continuous and discontinuous, have been proposed in the literature to describe the relationships between the coefficient of friction, forces, and velocities at this boundary. It is argued in [26] that the discontinuity cannot be eliminated. Alternately, smoothing is attempted to facilitate numerical integration of the equations of motion, [41, 44, 45, 56, 57].

In the complementarity conditions [13], there is a discontinuous change in the coefficient of friction, μ, as it jumps between the static, μ_s, and dynamic, μ_d, coefficients of friction. This results in a discontinuous change in the friction forces. Herein, this discontinuity is smoothed using the Karnopp model [44]. The Karnopp model is chosen in this research because of its lack of complexity, and its experimental validation [45]. As it is a static model, no additional system states are added for integration. Other friction models exist [45, 58–66], and can be substituted into the simulations presented in this work with little effort.

The feasible region imposed by the tangential velocity and coefficient of friction defined by the complementarity conditions is nonconvex, although it is contiguous. The boundary of the feasible region is examined by expressing it in terms of post-impact velocities. The shape of this bounding curve varies with surface orientation, implying that the coefficient of friction may change depending on surface orientation; its shape also changes depending on the COR. This possibility for change is applied to the dynamic coefficient

of friction in the dissipation principle discussed in Section 4.1. Further discussion of the modeling of oblique impacts is in [22, 25].

4.1 Dissipation Principle

The maximum dissipation principle is used to resolve the post-impact tangential velocities when slipping occurs. It is a minimization of the post-impact kinetic energy, as discussed in [11, 26, 51].

The proposed dissipation principle is based on examining the no-slip condition in the first relation of (3.4) and the impulsive forces in (3.13):

$$\frac{\|\mathbf{p}_{t_i}\|}{|p_{n_i}|} \leq \mu_i(\vartheta(t+\epsilon)) \tag{4.2}$$

where the static coefficient of friction has been replaced by a general one, and

$$p_{n_i} \geq 0 \tag{4.3}$$

for $i \in \{1, \ldots, m\}$. Recall from (3.13) that both $\mathbf{p}_{t_i}$ and p_{n_i} are functions of only $\vartheta(t+\epsilon)$ and thus (4.2) gives μ as a function of $\vartheta(t+\epsilon)$. A different μ_i is allowed for each contact point. Note that μ_i might be a function of all post-impact tangential velocities, not only the i^{th} one.

The relation in (4.2) can be examined to determine the feasible coefficient of friction μ_i and for a desired post-impact tangential velocity.

Since the feasible regions change so drastically with α it is desirable to ensure a feasible result, as opposed to using a blind guess of the dynamic coefficient of friction.

The coefficient of friction in relation to the post impact tangential velocity is shown in Figure 4.1. The main curve depicts the relation given in (4.2), and the shaded region on the right depicts the region where (4.3) is violated. The line at μ_f is defined by the solution for (4.2) where $v_t = 0$.

Two non-contiguous feasible regions of μ and v_t are at the bottom on the graph, with an upper limit of μ_f.

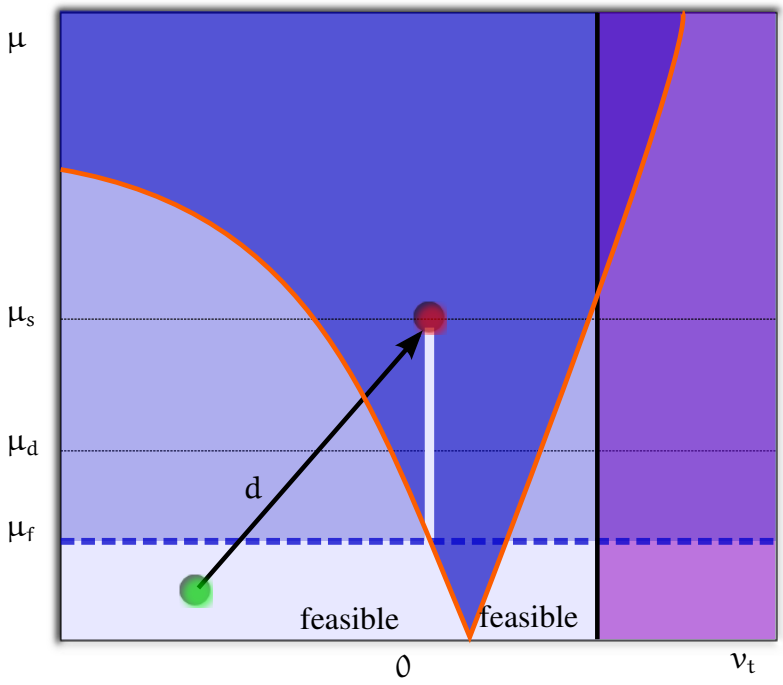

Figure 4.1. Coefficient of friction versus tangential velocity, maximum dissipation optimization.

A feasible solution for post impact tangential velocities is obtained by minimizing the distance from the known solution to the no-slip solution defined as

$$\mathbf{d} = \begin{bmatrix} \mu_s \\ 0 \\ 0 \\ \mu_s \\ 0 \\ 0 \\ \vdots \end{bmatrix} - \begin{bmatrix} \mu_1 \\ v_{t_{11}}(t+\epsilon) \\ v_{t_{12}}(t+\epsilon) \\ \mu_2 \\ v_{t_{21}}(t+\epsilon) \\ v_{t_{22}}(t+\epsilon) \\ \vdots \end{bmatrix} \tag{4.4}$$

subject to a complementary condition which allows expressions for the nonconvex feasible region as,

$$\min_{\left(v_{t_i}(t+\epsilon)\right)} \qquad \text{obj} := \mathbf{d}^T \mathbf{d} \tag{4.5}$$

$$\text{subject to} \qquad \mathbf{p}_{t_i}^T \mathbf{p}_{t_i} - \mu_i^2 p_{n_i}^2 \leq 0 \tag{4.6}$$

$$0 \leq p_{n_i} \tag{4.7}$$

for $i \in \{1, \ldots, m\}$, and where

$$\mathbf{p} = \left(JA^{-1}J^T\right)^{-1} \left(\vartheta(t+\epsilon) - \vartheta(t)\right) \tag{4.8}$$

$$\mu_{min_i} = \min\left(\mu_d,\ \mu_{f_i}\right) \tag{4.9}$$

$$\mu_i = \mu_{min_i} + \left(\mu_s - \mu_{min_i}\right) e^{-\left(\frac{\|v_{t_i}\|}{v_s}\right)^a} \tag{4.10}$$

The objective function in (4.5) has inconsistent units so it is assumed that the velocities are normalized by 1 with the appropriate units in order to make them unit-less. The desire is to maintain the value of the velocity so that the objective function will minimize them similarly to a maximum dissipation principle. The decision variables are also listed in (4.5).

The definition in (4.8) shows how the impulsive forces are calculated in terms of the decision variables. The constraint in (4.9) insures that the lower of μ_d and μ_{f_i} is used in the Karnopp friction model in (4.10) [44, 45]. Both of these values are known before starting the optimization; μ_{f_i} corresponds to the point where all of the $\boldsymbol{v}_{t_i} = \mathbf{0}$. In this work $v_s = 1.4 \times 10^{-4} m/s^2$ and $a = 1$ so that when $\|\boldsymbol{v}_{t_i}\| \approx 1 \times 10^{-3}$, $\mu_i \approx \mu_{min_i}$; also note that when $\boldsymbol{v}_{t_i} \approx \mathbf{0}$, $\mu_i \approx \mu_s$. This model eliminates the discontinuity between the forces specified using the static and dynamic coefficients of friction. The expression in (4.6) implements (4.2).

Figure 4.2 corresponds to $\alpha = 0$ for a single impact point and shows that (4.2) has a shape similar to a friction cone. Different curves are drawn for $0 \leq e_{n_i} \leq 1$ in order to examine the effect of a changing COR, which was experimentally observed in [53]. The μ above the curves correspond to sticking and those below the curves correspond to slipping. However, the complementarity conditions and the requirement that $p_{n_i} \geq 0$ impose further constraints on the feasible regions for slipping and sticking.

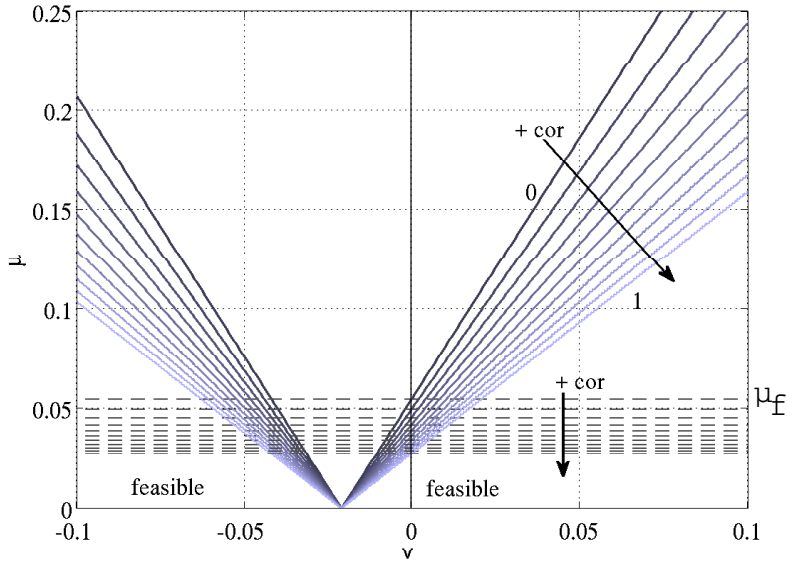

Figure 4.2. Coefficient of friction versus tangential velocity, $\alpha = 0$..

In Fig. 4.2 the entire region shown is feasible with respect to the $p_{n_i} \geq 0$ constraint. The complementarity conditions state that the feasible region for sticking is constrained to the $v = 0$ line above the desired COR curve. All μ less than the value of the intercept between the curve(s) and the $v = 0$ line define the feasible slipping μ. This region is upper bounded by the horizontal dashed lines Fig. 4.2, one for each value of the COR. *The value of* μ *at this line is denoted* $\mu_{f_i}(\mathbf{v}_{t_i}, \mathrm{COR})$ *and is shown on the far right of Fig. 4.2 for only one line*. A different μ_{f_i} can exist for each impact point.

Therefore the regions labeled "feasible" show the possible post-impact final velocities if the contact point slips; if not, the $v = 0$ line above the curve is the feasible region. Although the feasible regions are connected, the overall feasible region is nonconvex because of the single line representing the feasible region for sticking, which represents the discontinuity between the static and dynamic coefficients of friction. In Fig. 4.2, the initial static and dynamic coefficients of friction are $\mu_s = 0.5$ and $\mu_d = 0.25$. The figure shows that the chosen μ_s is feasible for $v = 0$. However, the chosen μ_d is infeasible when $v \neq 0$ for all values of the COR.

It is interesting to examine how the feasible regions change for different inclinations of the wedge. The cases for $\alpha \in \{15°, 30°, 45°\}$ are given in Figure 4.3 which show that the curves become nonlinear and can acquire asymptotes as α increases. The difference between Figures 4.2 and 4.3, 4.4, and 4.5 is that the latter show a dark area representing an infeasible region caused by the constraint $p_{n_i} > 0$. The boundary of this infeasible region becomes lighter with increasing COR.

In Figure 4.3, α is increased to 15. The curve for the up-slope tangential velocity $v_{t_i} < 0$ approaches a limit of $\mu = 1.5$ which is different behavior than examined in Figure 4.2. The down-slope tangential velocity approaches the same limit, except for a regain of $0 < v_{t_i} < 1$, where μ approaches infinity. The most dramatic change occurs when $\alpha = 45°$ in Fig. 4.5 where a zero tangential velocity is infeasible.

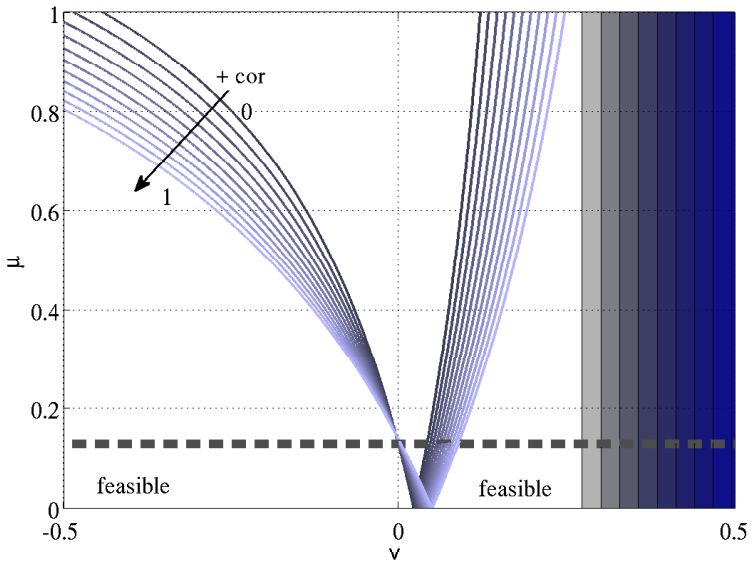

Figure 4.3. Coefficient of friction versus tangential velocity, $\alpha = 15°$.

Once the tangential velocities are known, the tangential CORs are found as

$$e_{t_{ij}} = \frac{v_{t_{ij}}(t+\epsilon)}{v_{t_{ij}}(t)} \tag{4.11}$$

If $v_{t_{ij}}(t) = 0$ and $v_{t_{ij}}(t+\epsilon) \neq 0$ then at this stage $v_{t_{ij}}(t)$ is set equal to $v_{t_{ij}}(t+\epsilon)$ and $e_{t_{ij}}$ is set equal to one.

4.2 Oblique Impact Example: Planar Bicycle System

Here the effect of an oblique impact is considered by assuming that the ground can tilt. The model used to illustrate this is the planar bicycle model discussed in Section 2.4.

The bicycle simulations are similar to those of the double pendulum in Section 2.3. The bicycle mechanism is comprised of two ellipsoidal wheels joined by a rigid bar. The mechanism has two possible contact points, instead of a single point. The bicycle drops on an inclined wedge, providing a robust analysis of multiple oblique impacts. The post impact

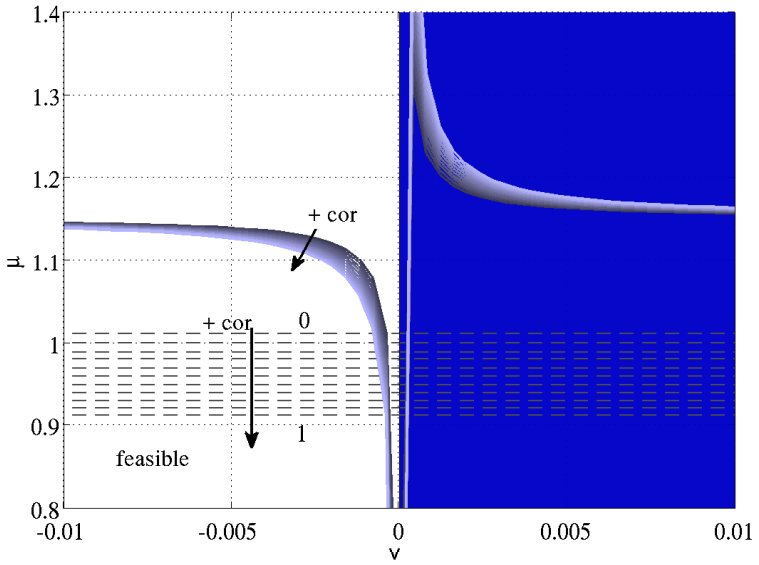

Figure 4.4. Coefficient of friction versus tangential velocity, $\alpha = 30°$.

tangential velocities of points in contact or impact are determined using the maximum dissipation principle discussed in Section 4.1.

The physical properties of the bicycle in Figure 2.4 are given in Table 2.2. The parameters of the bicycle simulations in this section are detailed in Table 4.1. Note that the parameter $\dot{q}_1$ is equal to 2 meters per second in Figure 4.6.

In Figure 4.8 the ground is horizontal with $\alpha = 0°$. The feasible μ for the first impact near $t \approx 1$ in Figure 4.8 shows that μ_s is feasible while μ_d is not. Thus $\mu = \mu_s$ at the first impact in Figure 4.8. As the bicycle settles down into rolling contact after 2.5s, the simulation begins to chatter as each wheel alternately bounces on the surface. Overall the impact/contact point sticks to the ground more often than not.

As the wedge angle increases, the bicycle bounces down the infinite wedge gaining kinetic energy; the trajectory for $\alpha = 0°$ is shown in Figure 4.6, and for $\alpha = 15°$ is shown in Figure 4.7. The line represents the path of the centerpoint of the bar connecting the wheels. The bicycle is drawn at its initial and final positions as well as at impact events. This case

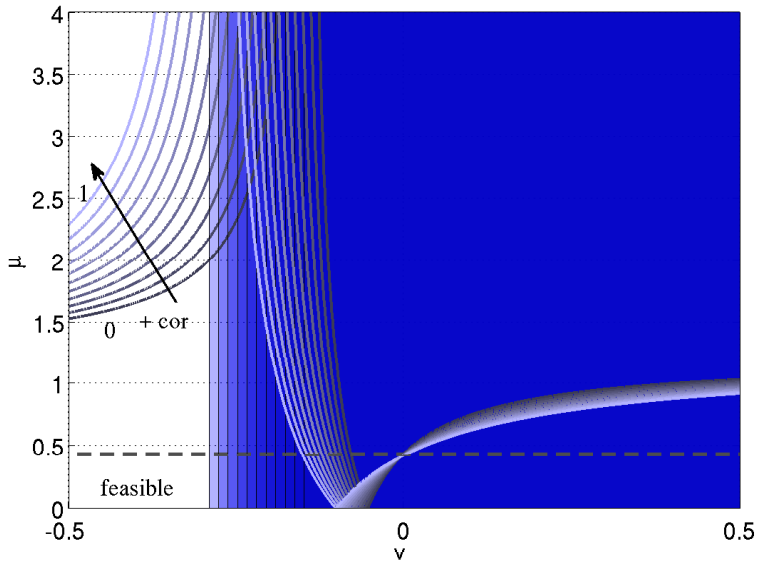

Figure 4.5. Coefficient of friction versus tangential velocity, $\alpha = 45°$.

corresponds to Figure 4.9. The feasible μ for the first impact is shown in Figure 4.9 and indicates that once again μ_s is feasible so that $\mu = \mu_s$ for the first impact in Figure 4.9. As the bicycle bounces down the wedge without settling into contact, the contact/impact point alternates sticks most often. Similar results are obtained in Figure 4.10 for $\alpha = 30°$. The first impact corresponds to Figure 4.10 where $\mu = \mu_s$ is feasible.

When $\alpha = 45°$, Figure 4.11 predicts that sticking is infeasible at the first impact, and this is proved true in Figure 4.11 where $\mu \leq 0.25$ at the first bounce. The remaining impacts slip more often than they stick and there is chattering at the end of the run. In all of these simulations it turns out that either the impact/contact point sticks, or the μ_s is feasible so other values for μ_d do not appear.

Table 4.1. Initial conditions for bicycle simulation

Parameter	Value
q_1	5 meters
q_2	5 meters
q_3	0°
q_4	0°
q_5	0°
$\dot{q}_1$	0 meters/second
$\dot{q}_2$	0 meters/second
$\dot{q}_3$	0
$\dot{q}_4$	0
$\dot{q}_5$	0
d_1	0.5 meters
d_2	0.25 meters

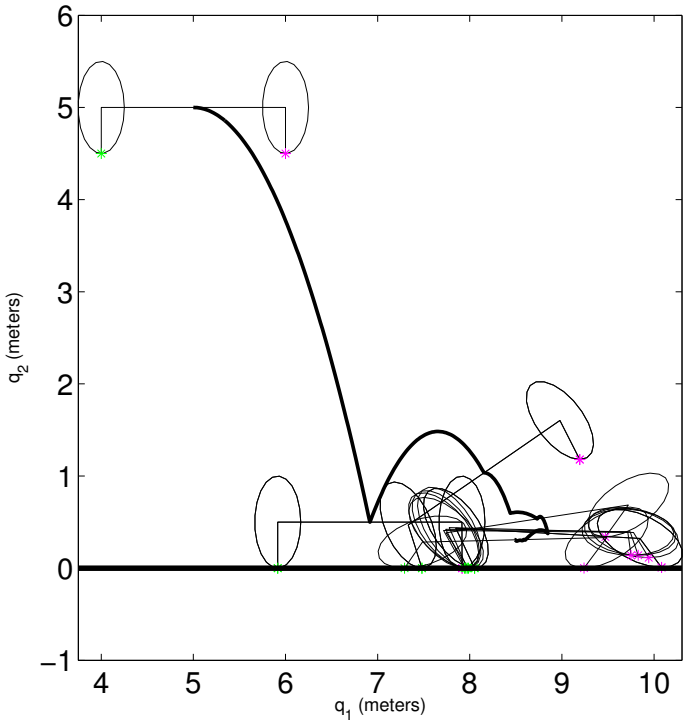

Figure 4.6. Bicycle trajectory for $\alpha = 0$.

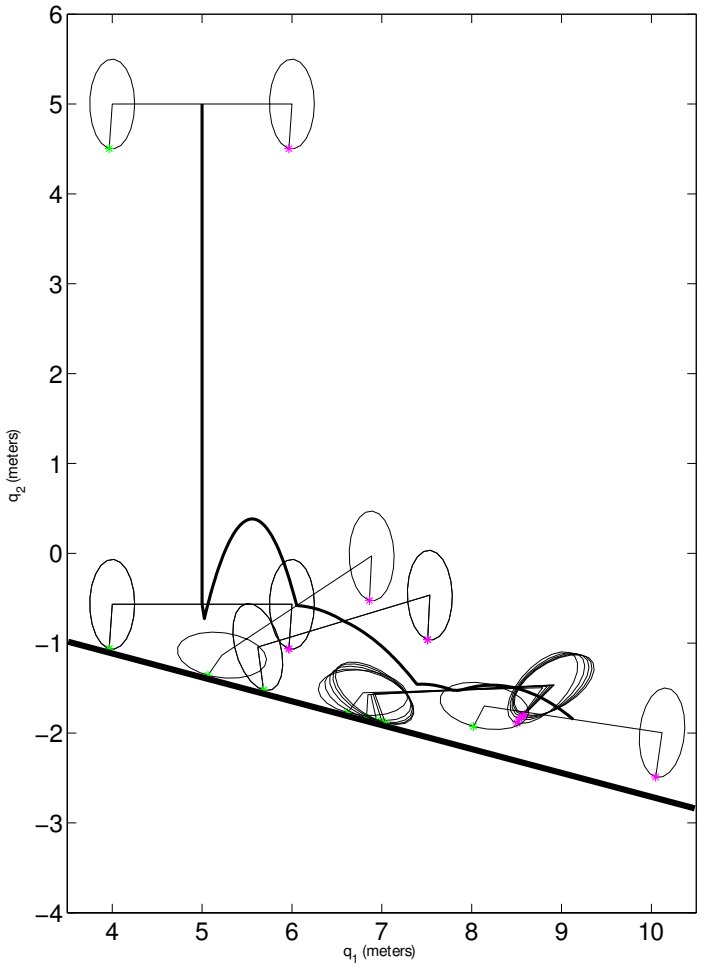

Figure 4.7. Bicycle trajectory for $\alpha = 15$.

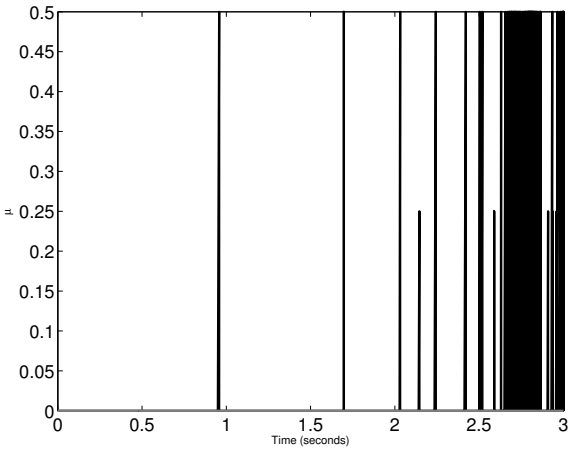

Figure 4.8. Coefficient of friction versus time, $\alpha = 0$.

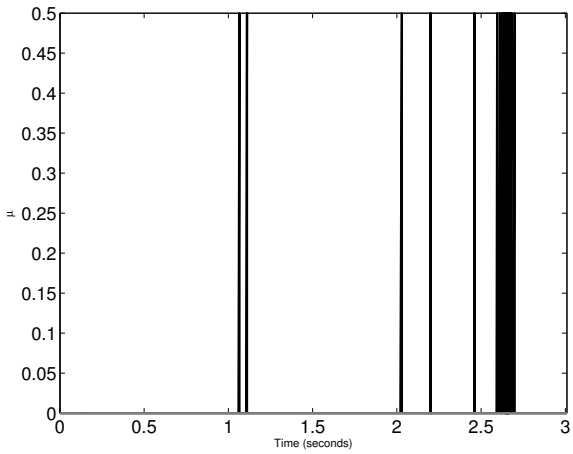

Figure 4.9. Coefficient of friction versus time, $\alpha = 15$.

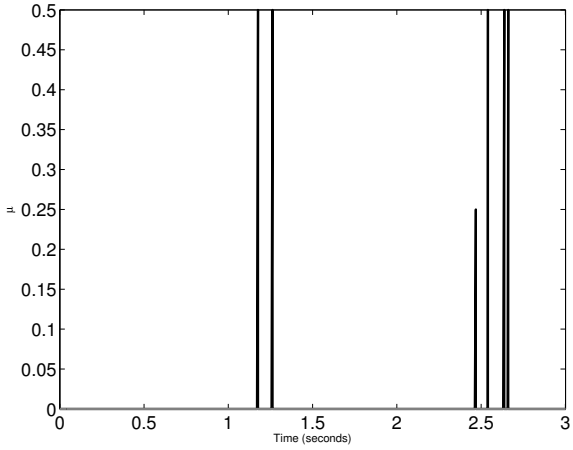

Figure 4.10. Coefficient of friction versus time, $\alpha = 30$.

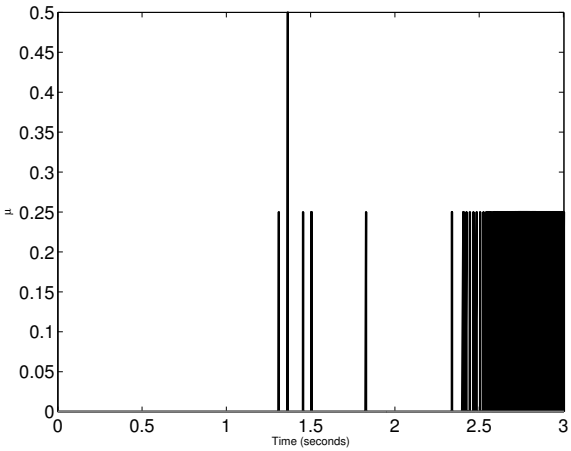

Figure 4.11. Coefficient of friction versus time, $\alpha = 45$.

CHAPTER 5

ENERGY CONSISTENCY

Using the complementarity conditions in Section 3.1, it is possible that a system can gain energy from an impact event [8–15]. In [67, 68], multiple discrete models were compared using rigid kinematic chains and they found that the energetic COR defined in [34, 35], discussed earlier, yielded the most energetically consistent results; however, only a single impact point was considered. In addition to the energetic COR, the approach in this research uses an *energy-modifying* COR to adjust the post-impact energy [24, 69]. A similar approach was discussed in [28] but was not formally expressed in terms of an energy-modifying COR. The idea is also similar to that of the *dissipation index* described in [70], but not identical.

The coefficients of restitution (CORs) (3.7) indirectly determine the amount of energy the system loses as a result of an impact. Some authors have considered relationships between the CORs and the system energy, for example [31, 38] for a single impact point, and [28] for multiple impact points assuming all CORs are equal. Rather than rely on these assumptions and limitations, it is desired to directly control the energy using a specified energetic COR e_*, similar to that in [35,71], and the energy-modifying COR, $\tilde{e}$. In [35,71], the energetic COR defines how much energy is lost in a single impact and usually has a value such that $0 \leq e_* \leq 1$.

Herein, energy consistency refers to the ability to control the amount of energy lost or gained from an impact, illustrated in Figure 5.1. The ability to control energy losses is useful for simulating different levels of dissipation between the impacting surfaces without modeling or tracking their deformations. This could be used to model walking in sand,

which can deform and dissipate a large amount of energy, without modeling all of the complexities of the surface deformation. The approach used in this work is a general methodology for hard and soft impacts when it is reasonable to neglect surface deformation.

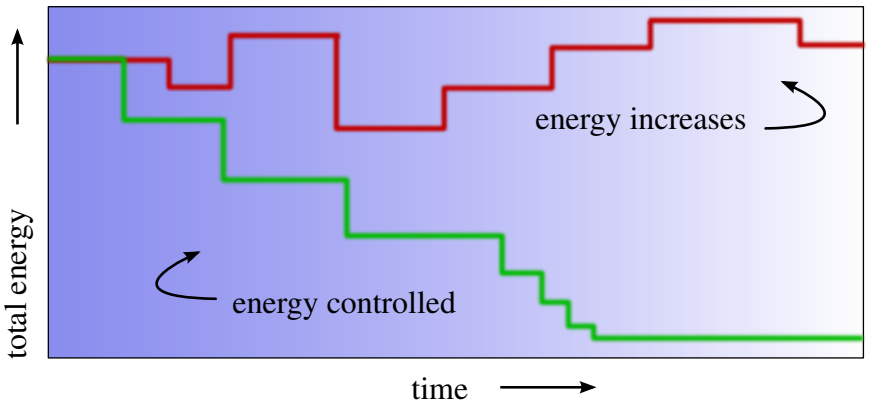

Figure 5.1. Energy consistency in simulation of a dynamic system impacting a surface.

5.1 Energetic coefficient of restitution

The desired energy loss is specified using the energetic coefficient of restitution, e_*, and the actual post-impact velocity is modified using the energy-modifying COR $\tilde{e}$. The post-impact energy is desired to be equal or less than that of the pre-impact energy. That is, $0 \leq \tilde{e} \leq 1$.

The use of e_* and $\tilde{e}$ in energy management is examined using the *Work-Energy Theorem* [50]. In classical impact modeling it is assumed that the configuration does not change during the interval $[t, t+\epsilon]$ therefore

$$T(\dot{\mathbf{q}}(t+\epsilon)) \;=\; T(\dot{\mathbf{q}}(t)) \;+\; W_\epsilon \tag{5.1}$$

where T represents kinetic energy, and W_ϵ is the work done on the system during the interval $[t, t+\epsilon]$.

In classical impact analysis, it is also assumed that impulsive forces dominate in affecting the state of the system during $[t, t+\epsilon]$. Therefore any change in kinetic energy from W_ϵ is attributed to work done by impulsive forces generated by unilateral nonpenetration constraints and friction forces.

A comparison of the kinetic energy before and after impact is expressed as

$$\tilde{e}^2\, \dot{\mathbf{q}}^T(t+\epsilon)\, A\, \dot{\mathbf{q}}(t+\epsilon) \;\leq\; e_*\, \dot{\mathbf{q}}^T(t)\, A\, \dot{\mathbf{q}}(t) \tag{5.2}$$

which can be solved for the $\tilde{e}$. The scaled velocities are designated as $\dot{\mathbf{q}}^*$,

$$\dot{\mathbf{q}}^* \;=\; \tilde{e}\, \dot{\mathbf{q}}(t+\epsilon) \;=\; \tilde{e}\, \left[I - \bar{J}J\right] \;+\; \tilde{e}\, \bar{J}\, E\, J\, \dot{\mathbf{q}}(t) \tag{5.3}$$

which corresponds to

$$\tilde{e}\, \left(J\, A^{-1} J^T\right)^{-1} (E - I)\, \underbrace{J\, \dot{\mathbf{q}}(t)}_{\vartheta(t)} \;=\; \tilde{e}\, \mathbf{p}\,. \tag{5.4}$$

Note that since $\tilde{e}$ multiplies the entire impulsive force vector, it does not change the state of sticking or slipping for the system. However, realize that the entire vector of generalized speeds is scaled, not just the velocities of the impact points, so this energy adjustment should be used sparingly.

5.2 Energy Analysis of the Double Pendulum System

The benchmark case of the double pendulum system is simulated to demonstrate the use of the energetic coefficient of restitution. Three cases where this parameter is varied are presented. The results demonstrate that the energy attenuation method ameliorates increases in kinetic energy at some impacts. The initial configuration for all simulations of the double pendulum system in this section are in Table 5.1.

The double pendulum is configured with minimal energy control in Section 5.2.1. This does not allow any energy increase at impact, but does not specify an energy loss

Table 5.1. Initial configuration of the double pendulum system

Parameter	Value
q_1	0.0 (initial)
q_2	0.0 (initial)
$\dot{q}_1$	0.0 s^{-1} (initial)
$\dot{q}_2$	0.0 s^{-1} (initial)

either. In Section 5.2.2, the energetic coefficient of restitution is decreased to a moderate level, forcing a specific energy loss at each impact. A sandy or muddy surface is approximated in Section 5.2.3, where the coefficient of restitution is lowered while a moderate energetic coefficient of restitution is used.

5.2.1 Double Pendulum with Minimum Energy Control

Setting the energetic COR equal to 1 prevents the energy increase as shown in Figure 5.2b. Since this is a perfectly elastic collision, the energy losses are caused by friction in the tangential direction. Comparing Figure 5.2b and Figure 3.4, the first impact is identical, but the second one is prevented from increasing the energy by the energy-modifying COR. The later energy increase at around 6 seconds in Figure 3.4 is also prevented in Figure 5.2b. In this case the normal forces in Figure 5.3b are positive, as they should be. The pendulum does not come to rest so only impact forces exist. The trajectory is shown in Figure 5.2a.

5.2.2 Double Pendulum with Moderate Energy Control

In this case the energetic COR has been reduced by half. It is assumed that the surface interaction extracts at least half of the pre-impact energy from the system, as though the surface is damped. In this case the mechanism comes to rest within 10 seconds as shown in Figure 5.4a.

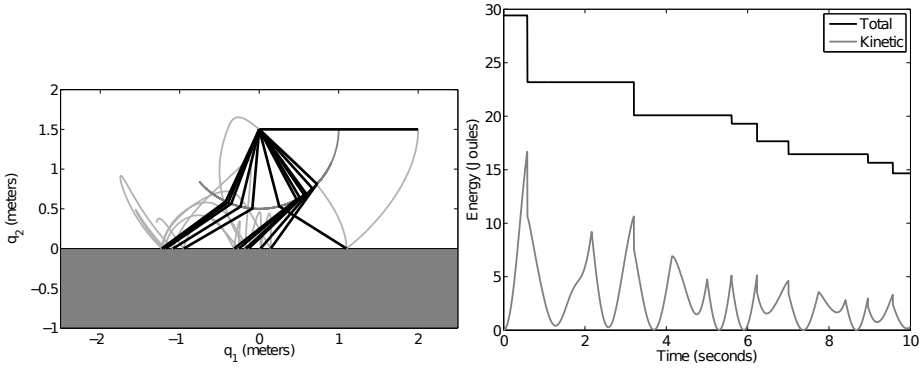

(a) (b)

Figure 5.2. Double pendulum simulation: $e_{n_i} = 1$, $e_* = 1$, (a) trajectory, (b) energy.

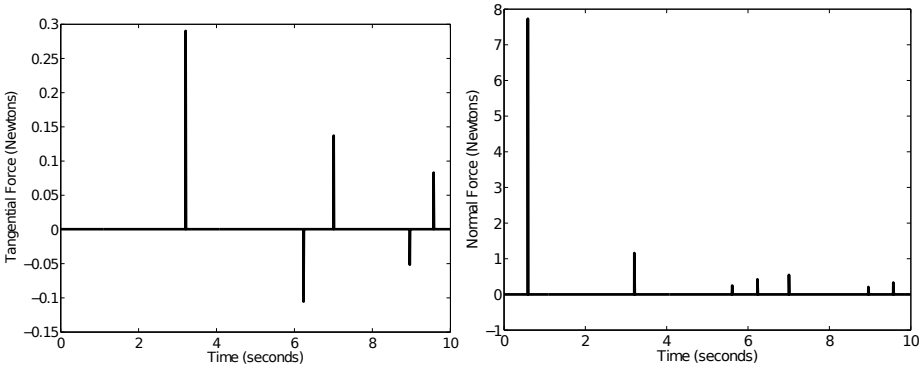

(a) (b)

Figure 5.3. Double pendulum contact forces: $e_{n_i} = 1$, $e_* = 1$, (a) tangential, (b) normal.

The kinetic energy drops by approximately half at each rebound until it comes to rest, see Figure 5.4b. When the pendulum comes to rest, the normal force reaches a constant level in Figure 5.5b as does the tangential force required to keep the tip from slipping in Figure 5.5a.

Figure 5.5a illustrates slip-reversals as well as the stick-slip transition as the pendulum comes to rest. The slip-reversal is indicated by the change in sign of the tangential forces as the pendulum comes to rest. The stick-slip transition is evident because of the small tangential forces which jump up to a large value as the pendulum comes to rest.

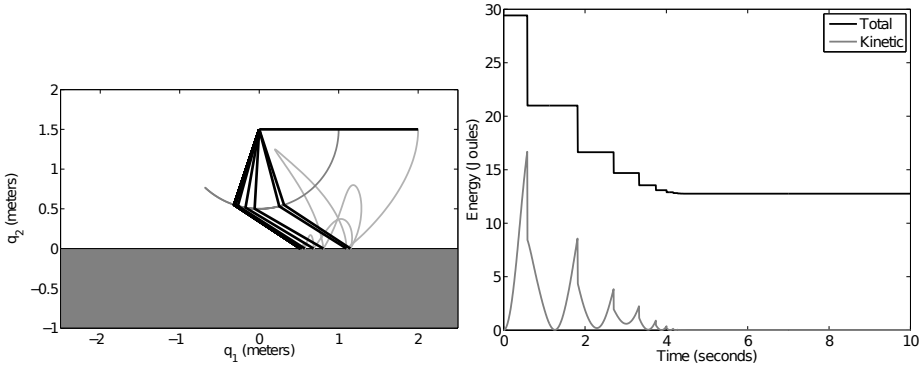

(a) (b)

Figure 5.4. Double pendulum simulation: $e_{n_i} = 1$, $e_* = 0.5$, (a) trajectory, (b) energy.

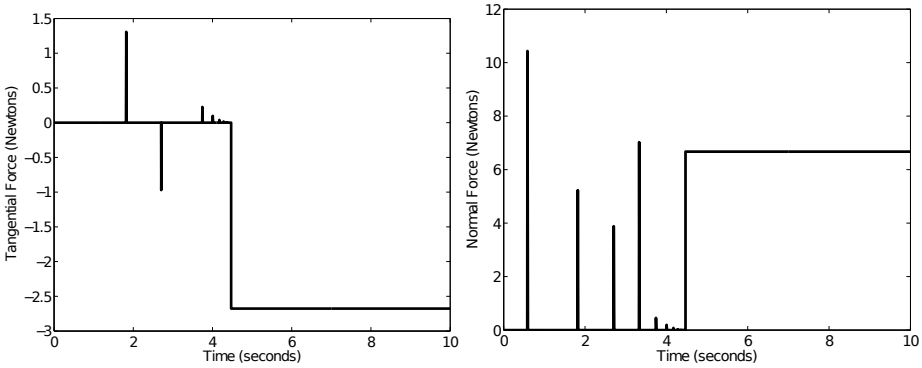

(a) (b)

Figure 5.5. Double pendulum contact forces: $e_{n_i} = 1$, $e_* = 0.5$, (a) tangential, (b) normal.

5.2.3 Double Pendulum with Moderate Energy Control, Low Coefficient of Restitution

This case is meant to show nearly plastic behavior where most energy is lost in the impact. This case, $e_{n_i} = 0.1$, was chosen because the case where $e_{n_i} = 0$ has multiple slip reversals that create so many events that it slows the simulation down significantly. In this case, the pendulum quickly comes to rest after two rebounds as shown in Figure 5.6a. The rest condition is indicated by the constant energy, normal force, and tangential force towards the ends of Figure 5.6b, Figure 5.7b, and Figure 5.7a. Figure 5.7a indicates the slip reversals occurring near the time when the system comes to rest.

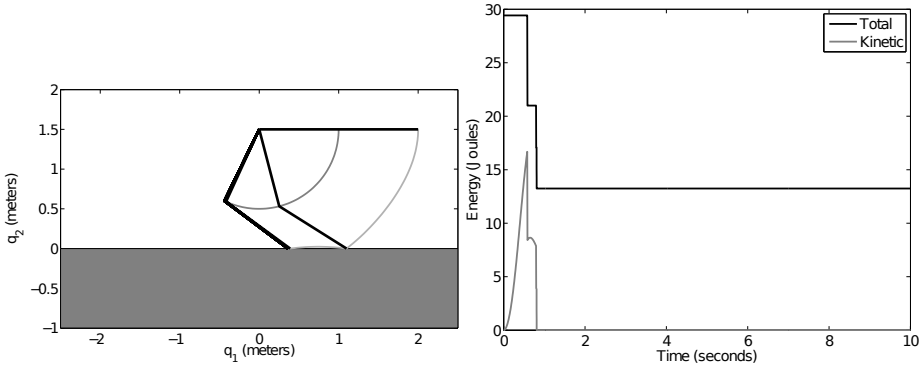

(a) (b)

Figure 5.6. Double pendulum simulation: $e_{n_i} = 0.1$, $e_* = 0.5$, (a) trajectory, (b) energy.

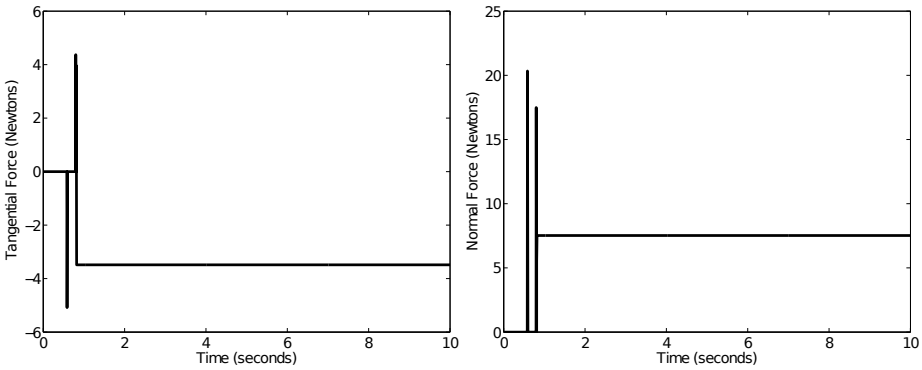

(a) (b)

Figure 5.7. Double pendulum contact forces: $e_{n_i} = 0.1$, $e_* = 0.5$, (a) tangential, (b) normal.

As with the double pendulum benchmark, an analysis of the planar bicycle system is performed with varying energetic coefficients of restitution. Section 5.3.1 is a simulation with a surface with a high coefficient of restitution, Section 5.3.2 uses a moderate coefficient of restitution, and Section 5.3.3 approximates a sandy or muddy surface with a low coefficient of restitution.

5.3 Energy Analysis of the Planar Bicycle System

The planar bicycle system is analyzed under varying energetic coefficients of restitution to illustrate the effects of velocity attenuation on the system behavior. Table 5.2 has the initial conditions, and parameters for the simulations in Section 5.3.1, Section 5.3.2, and Section 5.3.3.

Table 5.2. Initial conditions for bicycle simulation

Parameter	Value
q_1	5 meters
q_2	5 meters
q_3	0°
q_4	0°
q_5	0°
$\dot{q}_1$	2 meters/second
$\dot{q}_2$	0 meters/second
$\dot{q}_3$	0
$\dot{q}_4$	0
$\dot{q}_5$	0
d_1	0.5
d_2	0.5

5.3.1 Bicycle Mechanism with Energy Control, High Coefficient of Restitution

The simulation presented in Section 3.4.2 is rerun with an energetic coefficient of restitution of 0.95. The resulting trajectory is plotted in Figure 5.8a.

The normal and tangential contact forces are given in Figure 5.9b and Figure 5.9a. The total and kinetic energy is given in Figure 5.8b. Compare this to Figure 3.7, which has the same high coefficient of restitution, but no energy control.

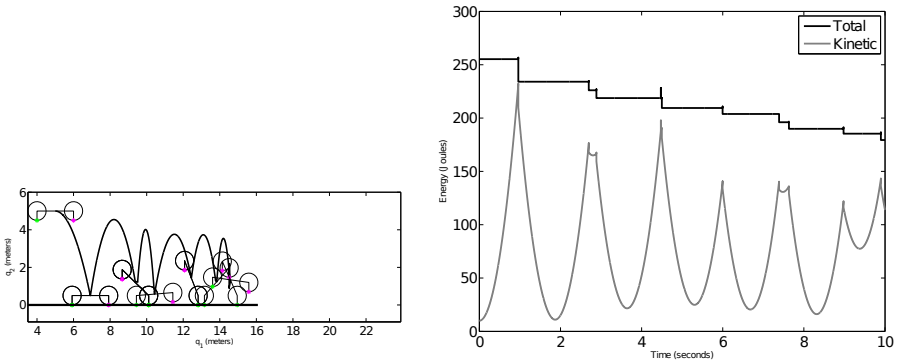

(a) (b)

Figure 5.8. Bicycle simulation: $e_{n_i} = 1.0$, $e_* = 0.95$, (a) trajectory, (b) energy.

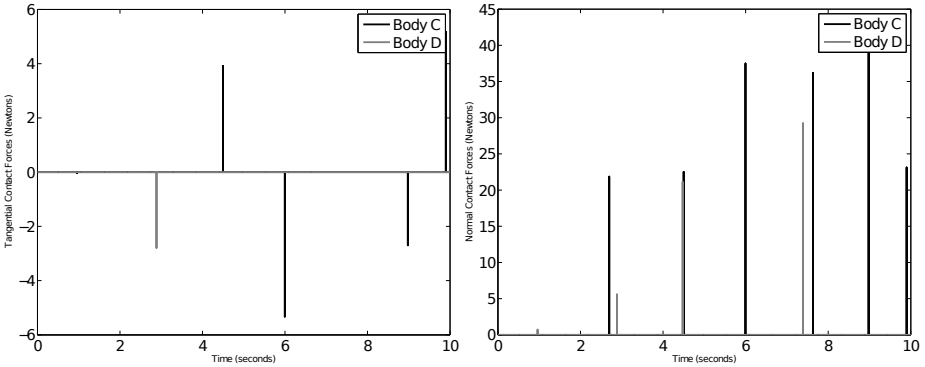

(a) (b)

Figure 5.9. Bicycle contact forces: $e_{n_i} = 1.0$, $e_* = 0.95$, (a) tangential, (b) normal.

5.3.2 Bicycle Mechanism with Energy Control, Moderate Coefficient of Restitution

The simulation presented in Section 5.3.1 is rerun with a coefficient of restitution of 0.5. The resulting trajectory is plotted in Figure 5.10a.

The normal and tangential contact forces are given in Figure 5.11b and Figure 5.11a. The total and kinetic energy is given in Figure 5.10b.

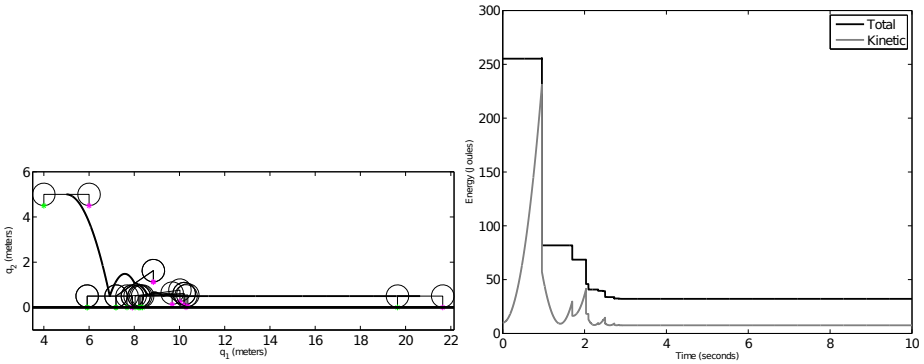

(a) (b)

Figure 5.10. Bicycle simulation: $e_{n_i} = 0.5$, $e_* = 1.0$, (a) trajectory, (b) energy.

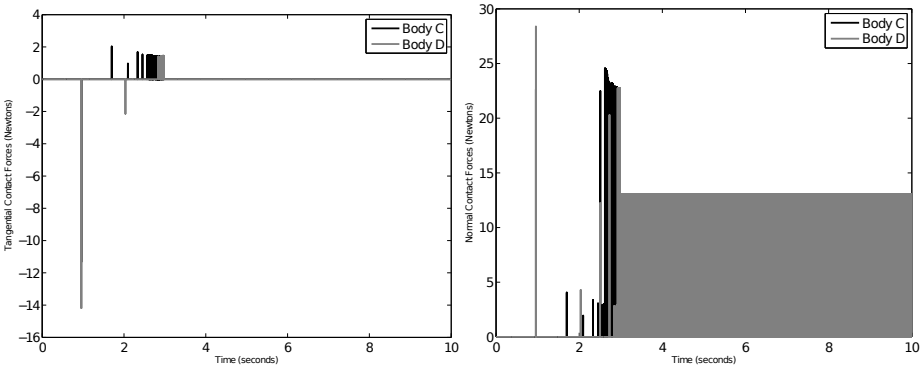

(a) (b)

Figure 5.11. Bicycle contact forces: $e_{n_i} = 0.5$, $e_* = 1.0$, (a) tangential, (b) normal.

5.3.3 Bicycle Mechanism with Low Coefficient of Restitution

This case represents a perfectly plastic collision in order to investigate the energy issue when rolling. As expected, the bicycle hits with no rebound, and begins to roll as shown in Figure 5.12a.

The energy is constant after impact as shown in Figure 5.12b. Again this suggests additional friction forces that must be considered. Another possible way to address this, rather than stick-slip tangential forces, would be to reduce the energy-modifying COR.

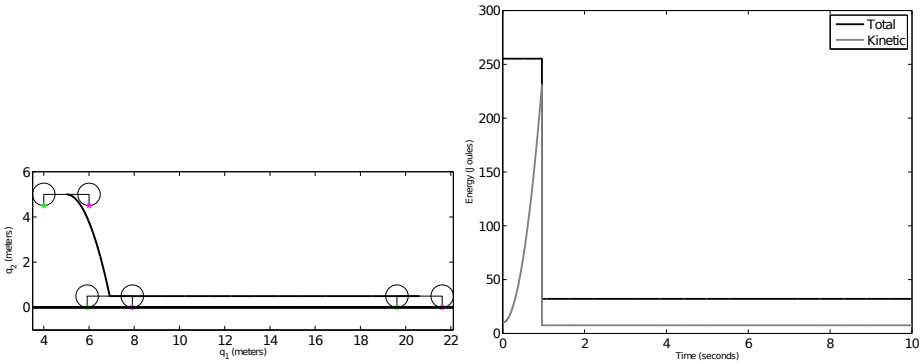

(a) (b)

Figure 5.12. Bicycle simulation: $e_{n_i} = 0.0$, $e_* = 1.0$, (a) trajectory, (b) energy.

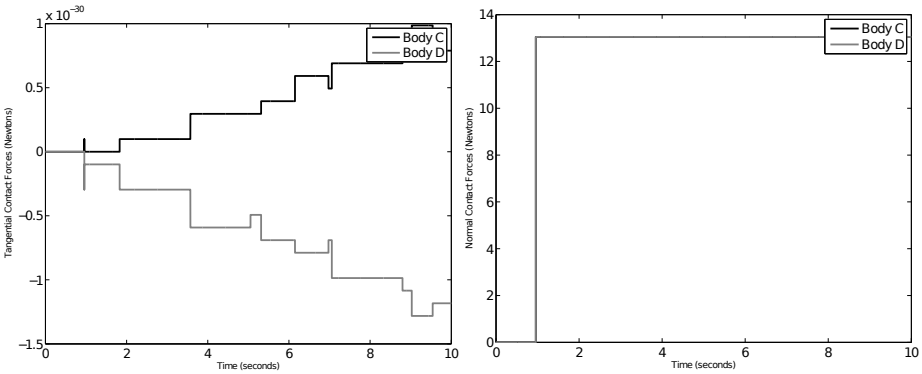

(a) (b)

Figure 5.13. Bicycle contact forces: $e_{n_i} = 0.0$, $e_* = 1.0$, (a) tangential, (b) normal.

The bicycle wheels roll with a constant speed after reaching the surface. This is caused by the tangential forces acting on the wheels being approximately zero, as seen in Figure 5.13a. These low tangential forces do not remove energy from the system. The normal contact forces are given in Figure 5.13b.

5.4 Alternate Energy Control Method

The method to obtain a feasible solution for post impact tangential velocities is discussed in Section 4.1 [25]. The optimization to obtain these velocities is modified to in-

clude an additional constraint for kinetic energy. Kinetic energy should decrease or remain constant after an impact event. However, in common impact models, kinetic energy can sometimes increase after an impact event [8–15]. In the work in [24, 25], an energetic coefficient of restitution is used along with a velocity attenuation method to decrease the post impact kinetic energy, if needed.

The tangential velocity optimization minimizes the distance from the known solution to the no-slip solution , defined as

$$\mathbf{d} = \begin{bmatrix} \mu_s \\ 0 \\ 0 \\ \mu_s \\ 0 \\ 0 \\ \vdots \end{bmatrix} - \begin{bmatrix} \mu_1 \\ v_{t_{11}}(t+\epsilon) \\ v_{t_{12}}(t+\epsilon) \\ \mu_2 \\ v_{t_{21}}(t+\epsilon) \\ v_{t_{22}}(t+\epsilon) \\ \vdots \end{bmatrix} \tag{5.5}$$

subject to a complementary condition which allows expressions for the nonconvex feasible region as,

$$\min_{(v_{t_i}(t+\epsilon))} \qquad \text{obj} := \begin{bmatrix} \mu_s - \mu_1 \\ -v_t(t+\epsilon) \end{bmatrix}^T \begin{bmatrix} \mu_s - \mu_1 \\ -v_t(t+\epsilon) \end{bmatrix} \tag{5.6}$$

$$\text{subject to} \qquad \mathbf{p}_{t_i}^T \, \mathbf{p}_{t_i} - \mu_i^2 \, p_{n_i}^2 \leq 0 \tag{5.7}$$

$$0 \leq p_{n_i} \tag{5.8}$$

$$0 \leq T^* - T \tag{5.9}$$

for $i \in \{1, \ldots, m\}$, and where

$$\mathbf{p} = \left(JA^{-1}J^T\right)^{-1} \left(\vartheta(t+\epsilon) - \vartheta(t)\right) \tag{5.10}$$

$$\mu_{min_i} = \min\left(\mu_d,\ \mu_{f_i}\right) \tag{5.11}$$

$$\mu_i = \mu_{min_i} + \left(\mu_s - \mu_{min_i}\right) e^{-\left(\frac{\|v_{t_i}\|}{v_s}\right)^a} \tag{5.12}$$

$$T^* = e_* \dot{\mathbf{q}}^T(t)\, A\, \dot{\mathbf{q}}(t) \tag{5.13}$$

$$T = \dot{\mathbf{q}}^T(t)\, A\, \dot{\mathbf{q}}(t) \tag{5.14}$$

μ_f is discussed in detail in Section 4.1 [25], and is the value of μ where $v_t = 0$ according to (5.7). μ_s and μ_d are the static and dynamic coefficients of friction. The values v_s and a define the shape of the curve in (5.12). The parameter e_* is the energetic coefficient of restitution [24], and controls the minimum amount of kinetic energy lost during impact events.

5.5 Alternate Energy Analysis of the Double Pendulum System

Two simulations of the double pendulum system [25] were run to compare the system behavior with and without an energy constraint in the post impact tangential velocity optimization, as discussed in Section 5.4. The simulation run times of both cases are in Table 2.4. The inclusion of an energy constraint in the post impact tangential velocity optimization results in an increase in CPU time.

The parameters of the double pendulum simulation are given in Table 5.3. The integrator step is not a time value for a fixed step integrator, but the maximum time interval to save system states as output. A value of 1 is chosen for e_* to enforce that kinetic energy after an impact is less than or equal to the kinetic energy before impact.

Table 5.3. System parameters

Parameter	Value
Coeffient Of Restitution	1.0
e_*	1.0
μ_s	0.74
μ_d	0.57
T_{final}	5.0 seconds
q_1	$\pi/4$ (initial)
q_2	$-3\pi/4$ (initial)
$\dot{q}_1$	0.0 s^{-1} (initial)
$\dot{q}_2$	0.0 s^{-1} (initial)
Integrator step	0.01 seconds
Absolute integrator error	10^{-9}
Relative integrator error	10^{-8}

A simulation of the double pendulum system run without any energy control is presented in Figure 5.14. Its trajectory is in Figure 5.14b, and energies are shown in Figure 5.14a. The first impact, at approximately $t = 0.5$ seconds, exhibits an increase in kinetic energy. Subsequent impacts do not gain energy, as the kinetic energy increase does not occur during every impact.

A comparison of simulated trajectories run with energy control is given in Figure 5.15. Figure 5.15a plots the trajectory of the case with a velocity attenuation scheme [24], but without an energy constraint in the post impact tangential velocity optimization. Figure 5.15b plots the trajectory with an energy constraint included in the optimization, as described in (5.6 – 5.14). The behavior of the system is identical for both cases until the final bounces. The end of the pendulum impacts multiple times in close proximity to $-0.5N_1$ meters in the energy constrained case.

The difference in the trajectories in Figure 5.15 is explained by the energy plots in Figure 5.16. The total, kinetic, and potential energy is plotted for the case without an energy constraint in Figure 5.16a. The energies for the energy constrained case are shown

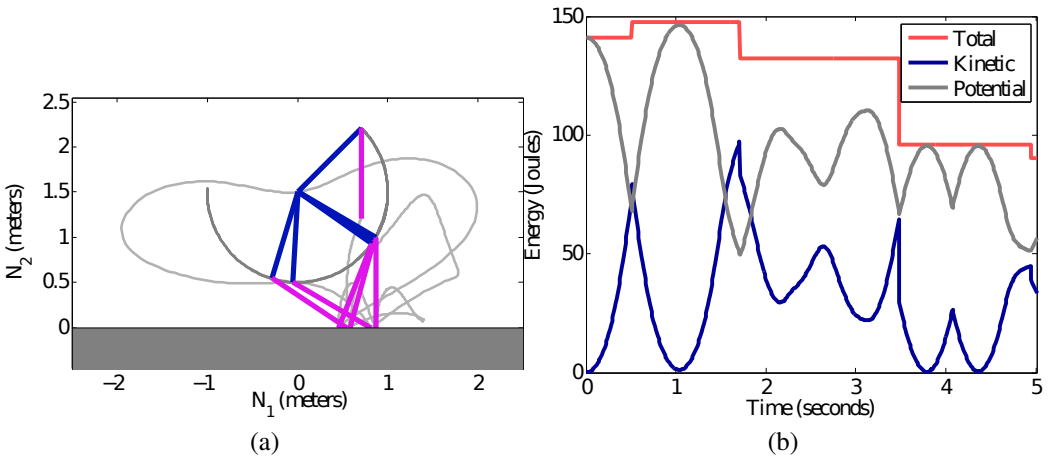

Figure 5.14. Simulation of double pendulum system without energy control, (a) trajectory, (b) energy.

in Figure 5.16b. The difference in the two simulations is evident at the impact that occurs at approximately 3.25 seconds. The system loses more kinetic energy during the impact at this time for the energy constrained case. With this loss in kinetic energy, the behavior of the system is altered. Both cases are valid, but a different solution for the post impact tangential velocity is found during an impact in the simulation with energy as a constraint in the optimization.

In the simulation run without energy control, shown in Figure 5.14b, a gain in post impact kinetic energy is present at approximately $t = 0.5$ seconds. The gain is most evident when considering the total energy plot. In the simulations run with energy control, no gains in kinetic energy occur. The impact at approximately $t = 0.5$ seconds has a gain in energy, but it is limited by both the velocity attenuation and energy constraint methods. The two energy limiting methods obtain the similar results for post impact velocities on the first bounce, where an energy gain would otherwise occur.

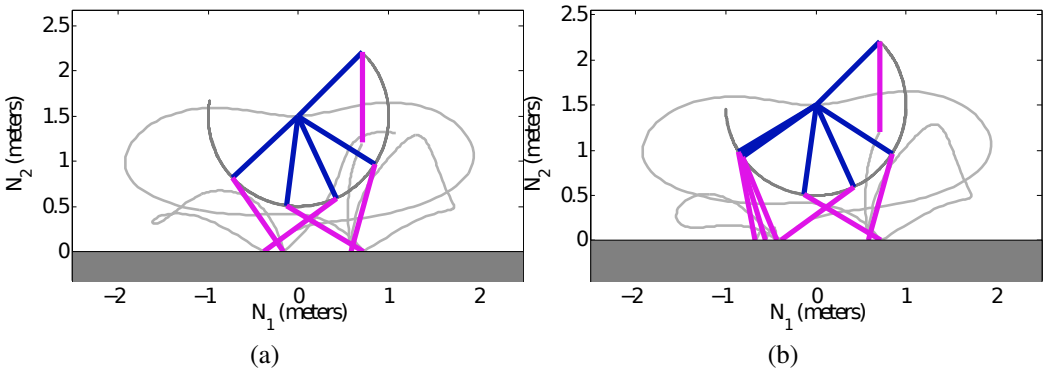

Figure 5.15. Simulated double pendulum trajectories with energy control, (a) with velocity attenuation, (b) with energy constraint.

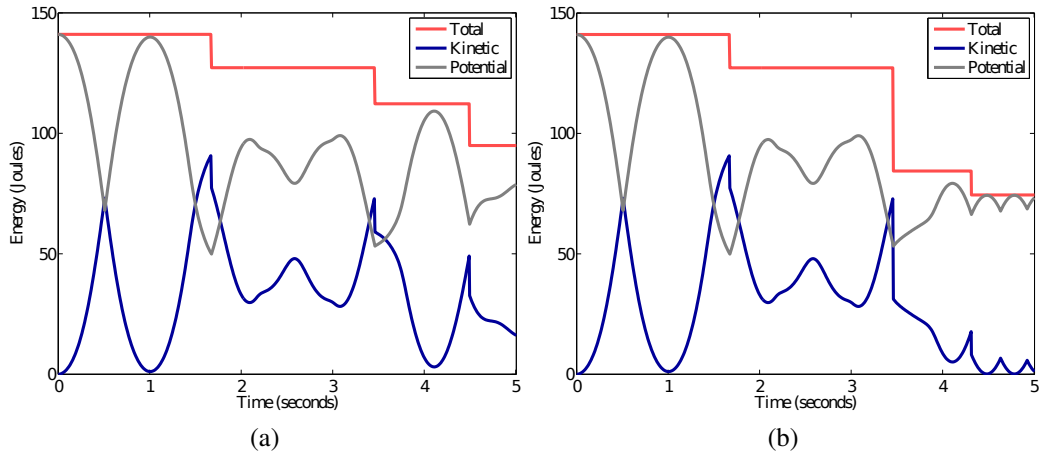

Figure 5.16. Simulated double pendulum energies with energy control, (a) with velocity attenuation, (b) with energy constraint.

The velocity attenuation method is only applied at impacts where there is an increase in energy. Adding a constraint for energy enforces energy consistency at every impact event, obviating the need for an additional check. The energy constraint can be altered to limit the post impact kinetic energy to a desired level. However, the precise amount of energy loss at each impact is not known, and cannot be predicted with either method. In the energy constraint method, specific tangential velocities to achieve a desired drop in post impact kinetic energy can be obtained within the optimization. This is an alternative to attenuating all post impact velocities only when the post impact kinetic energy is higher than desired.

The additional CPU time required by the method including the energy constraint in the optimization can be improved. In addition, this work examined a simple benchmark case where only a single impact is involved; other differences may appear for a more complex system with multiple impact points. The results presented here represent a preliminary investigation. Further investigation into improving the optimization will be performed in the future by the Robotics, Biomechanics, and Dynamics Systems lab at the University of Texas at Arlington.

CHAPTER 6

CONFIGURATION OPTIMIZATION FOR AGILE JUMPING

Jumping is considered in this work in the research into agility. Jumping itself involves large abrupt changes in trajectory, and is closely tied to the ability of a robot to produce large accelerations. The ability to jump influences the ability to run, or otherwise travel through a challenging environment in an agile manner. A method to improve the jumping performance of a single leg jumping robot is presented in this chapter. Through optimization of the initial configuration of the robot before a jump, the performance and agility of the robot can be increased both during the stance and ballistic phases of a jumping cycle.

Examples of jumping robot control found in the literature neglect the limits on joint torques from both actuator saturation and the limits of tangential forces at the contacts to prevent slip. Commanding maximum joint torques and allowing the robot to slip causes stumbling, which severely degrades jumping performance. For example, the trajectory during the stance phase can be optimized as such to minimize energy usage, which in turn minimizes actuator torques [72, 73]. Heuristic methods, such as fuzzy control can be used to optimize periodic gaits and help transition mechanisms to an energy saving gallop [74], but these controllers neglect to directly consider the dynamic properties of the mechanism in closed form.

The method presented here not only prevents slipping by taking into account limits in actuator torques and contact forces, but also improves the jump performance by placing the robot in a desirable configuration before executing a jump. The jumping robot simulations used in this research take into account contact characteristics such as rebound and slip

[22, 24, 75]. Hybrid dynamic simulation is used to model contact as a series of impacts, stopping and restarting integration during contact events.

As agility is the ability of a mechanism to rapidly change trajectory, a measure of the capability of a mechanism to accelerate can quantify the agility of a mechanism in a particular posture or configuration. Maximizing the acceleration capability affects the agility of a mechanism. The Dynamic Capability Equations (DCE) [48, 76, 77] are used to obtain a closed form solution to the acceleration capability of a mechanism. The DCE can be transformed to obtain the capability in a desired direction, as discussed in Section 6.1. In this work, the directional DCE are used in an optimization to calculate the best initial configuration for a given mechanism to accelerate and take off in a desired direction.

6.1 Directional DCE

The directional DCE describe acceleration capability in a particular direction. They are derived from the equations of motion. Rearranging and grouping terms in the equations of motion (2.1) leads to

$$\mathsf{E}\,\dot{\vartheta}_{\mathsf{A}} \;+\; \boldsymbol{\mu} \;+\; \mathbf{g} \;=\; \Upsilon \tag{6.1}$$

where $\mathsf{E} = \mathsf{G}^{-\mathsf{T}}\mathsf{A}\mathsf{J}_{\mathsf{A}}^{-1}$ is the inertial term, $\boldsymbol{\mu} = \mathsf{G}^{-\mathsf{T}}(\mathbf{b} - \mathsf{A}\mathsf{J}_{\mathsf{A}}^{-1}\,\dot{\mathsf{J}}_{\mathsf{A}}\dot{\mathbf{q}})$ contains the velocity forces, and $\mathbf{g} = \mathsf{G}^{-\mathsf{T}}\mathbf{g}$ is the gravity force. The actuator bounds are

$$-\Upsilon_{\text{bound}} \;\leq\; \Upsilon \;\leq\; \Upsilon_{\text{bound}} \tag{6.2}$$

with Υ_{bound} containing the torque limits on the actuators. Each relation in (6.2) is considered independently. (6.1) is substituted into (6.2) yielding

$$-\Upsilon_{\text{bound}} \;\leq\; \mathsf{E}\,\mathsf{R}_{\mathsf{x}}\,\dot{\vartheta}_{\mathsf{Ax}} \;+\; \boldsymbol{\mu} \;+\; \mathbf{g} \;\leq\; \Upsilon_{\text{bound}}\,. \tag{6.3}$$

In this work, the capability to accelerate the end-effector in a particular direction, such as the x-direction denoted $\dot{v}_x$, is examined. Thus a rotation matrix R_x is used to orient $\dot{\vartheta}_A = R_x\,\dot{\vartheta}_{Ax}$ such that the first element of $\dot{\vartheta}_{Ax}$ points in the desired direction.

Isolating $\dot{v}_x$ in (6.3) yields

$$E_x\dot{v}_x \leq \Upsilon_{bound} - \mu - g - E_r\dot{\vartheta}_r \equiv \Upsilon_{upper} \tag{6.4}$$

$$E_x\dot{v}_x \geq -\Upsilon_{bound} - \mu - g - E_r\dot{\vartheta}_r \equiv \Upsilon_{lower} \tag{6.5}$$

where E_x is the column of E associated with $\dot{v}_x$, E_r contains the remaining columns of E, and $\dot{\vartheta}_r$ contains all accelerations except $\dot{v}_x$. All terms other than the one of interest, $\dot{v}_x$, are considered to shift the torque bounds. The new bounds are defined as Υ_{upper} and Υ_{lower}. Now the *directional* DCE can be obtained as,

$$\mathbb{A}\,|\dot{v}_x| \;\leq\; \mathbb{T} \;=\; \begin{bmatrix} \Upsilon_{upper} \\ -\Upsilon_{lower} \end{bmatrix} \tag{6.6}$$

where $\mathbb{A} \in \mathbb{R}^{2n\times 1}$ and $\mathbb{A}_i = \mathbb{A}_{i+n} = \|E_{x_i}\|$, and where $\mathbb{A}_i$ is the ith row of $\mathbb{A}$ and E_{x_i} is the ith row of E. The details for determining (6.6) can be found in [48, 78]. The extent of *acceleration capability* in the x-direction is the largest value of $|\dot{v}_x|$ which satisfies all inequalities in (6.6). The function $|\dot{v}_x|$ is nonholonomic because it is discontinuous and defined in terms of inequalities.

Although $\dot{v}_{x_i}$ is the x-direction acceleration capability, because of the presence of absolute value terms in $\mathbb{A}$, this capability may apply to either the positive or negative x-directions. This signifies that, in this form, the capability calculated from these equations gives the lowest available guaranteed acceleration along the x-axis. For each set of capability equations, exactly half of them apply to each direction, i.e. half apply to $+$x-direction accelerations, and half apply to $-$x-direction accelerations. The sign of E_{x_i}, before taking the absolute value, indicates in which direction each particular capability equation applies.

Therefore, the only equations of interest are those which indicate the acceleration capability in the direction of the desired task, which in this treatment is the $+x$-direction. The gradient of (6.6), which will be used to determine the nullspace motion, will only consider those equations from (6.6) with SIGN(E_{x_i})> 0.

6.2 Configuration Optimization

The simulation discussed in this work concentrates on the state of the robot at the end of the stance phase, right before a jump. The configuration at this transition point is optimized offline, with the result substituted as the initial system configuration.

$$\min_{(\mathbf{q_i(t)})} \quad \text{obj} := \dot{v}_x^{-1} \tag{6.7}$$

$$\text{subject to} \quad \Upsilon_{\mathbf{lower}} \leq \Upsilon_{\mathbf{bound}} \leq \Upsilon_{\mathbf{upper}} \tag{6.8}$$

$$\mathbf{q_{lower}} \leq \mathbf{q} \leq \mathbf{q_{upper}} \tag{6.9}$$

$$H_k = 0 \tag{6.10}$$

$$-K_k \leq 0 \tag{6.11}$$

where H are the heights of the contact points, and K are heights of all of the joints and body centers on the mechanism, all projected in the direction normal to the ground, N_2. Joint limits are also enforced in the configuration space for this optimization. The heights of the k contact points and other points on the mechanism are included as constraints in the optimization to find feasible configurations that result in the entire mechanism being above the ground.

The computed torque method [23] is used to control the trajectory of the geometric center of the robot body while in contact with the ground. Actuator saturation limits are enforced in the controller torque outputs. A single jump along an arbitrary direction is

desired. The dynamic capability equations along this arbitrary direction are solved. The joint torque limits and contact point maximum forces are dependent on the configuration of the robot. The gradient of this solution is used to resolve a small change in configuration to maximize acceleration capability in a desired direction.

The configuration is resolved until maximum potential performance is achieved, then the mechanism jumps. The improved configuration allows the robot to jump further along the desired direction, while minimizing slipping of the contact point.

6.3 Characterization of Acceleration Capability

The acceleration capability field in the configuration space of q_8 and q_9 is shown in Figure 6.1. The parameter q_8 is the angle of the femur, and q_9 is the angle of the tibia, as shown in Figure 2.5. In this example, the coxa angle is held at zero, approximating a planar mechanism. This illustrates the field that the optimization in which (6.7) operates. Higher color saturation represents increasing acceleration capability. The regions of high capability are not contiguous, meaning that the optimized configuration can be dependent on the initial guess configuration.

A series of jumping simulations with random configurations are tested to illustrate the correlation between acceleration capability and stance phase duration. The stance phase of a jump is the period of time where the robot is in contact with the ground before jumping. This period is important in that the robot can control its trajectory. Alterations in trajectory are not possible once the robot leaves the ground. The increasing of the stance phase is an important component of agility, and the impact of the acceleration capability is shown in this section.

As in Figure 6.1, only the final two configuration parameters are varied in the simulations. Figure 6.2 illustrates all the configurations tested. The points labeled “timeout” oc-

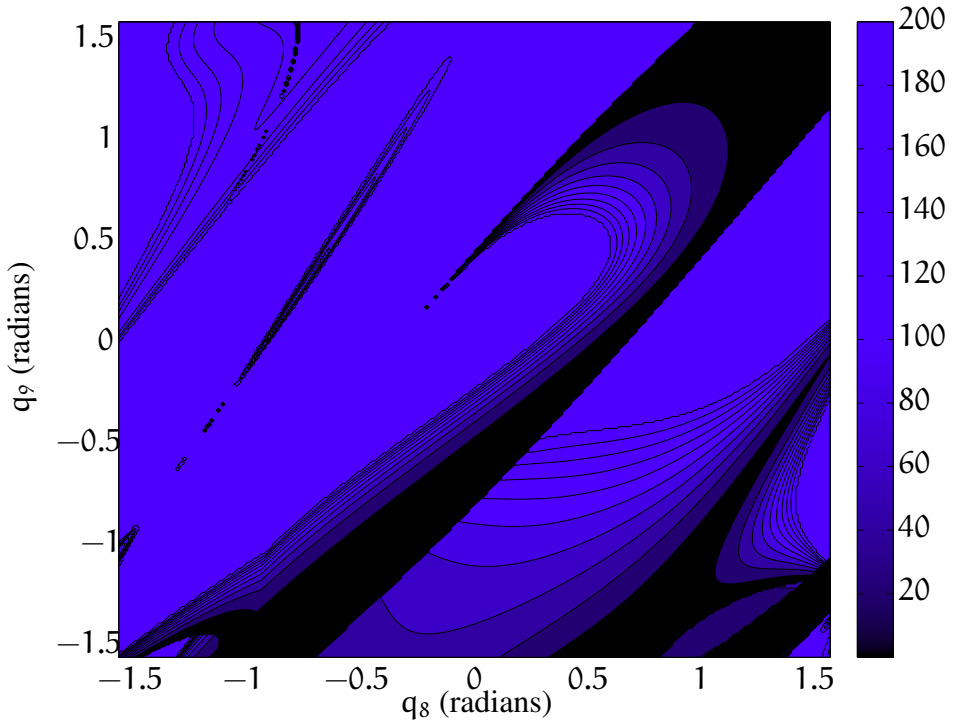

Figure 6.1. Acceleration capability in configuration space for the jumping leg.

curred for configurations that resulted in a simulation that could not produce a jump within 30 minutes of wall time (elapsed time). These were configurations that resulted in dynamics that were difficult to integrate. The data points labeled "jumped" are for configurations that resulted in a successful jump, except that the stance phase duration was approximately zero. These configurations allowed the robot to jump, but not with as much performance as with the configurations marked as "filtered". The filtered data points resulted in a successful jump, and the robot remained in contact with the ground for a nonzero duration. The filtered data points are used to produce the plot in Figure 6.3.

The duration of the stance phase before a jump versus acceleration capability is shown in Figure 6.3. The stance phase duration increases as acceleration capability increases. This relationship is apparent in simulations where the acceleration capability of

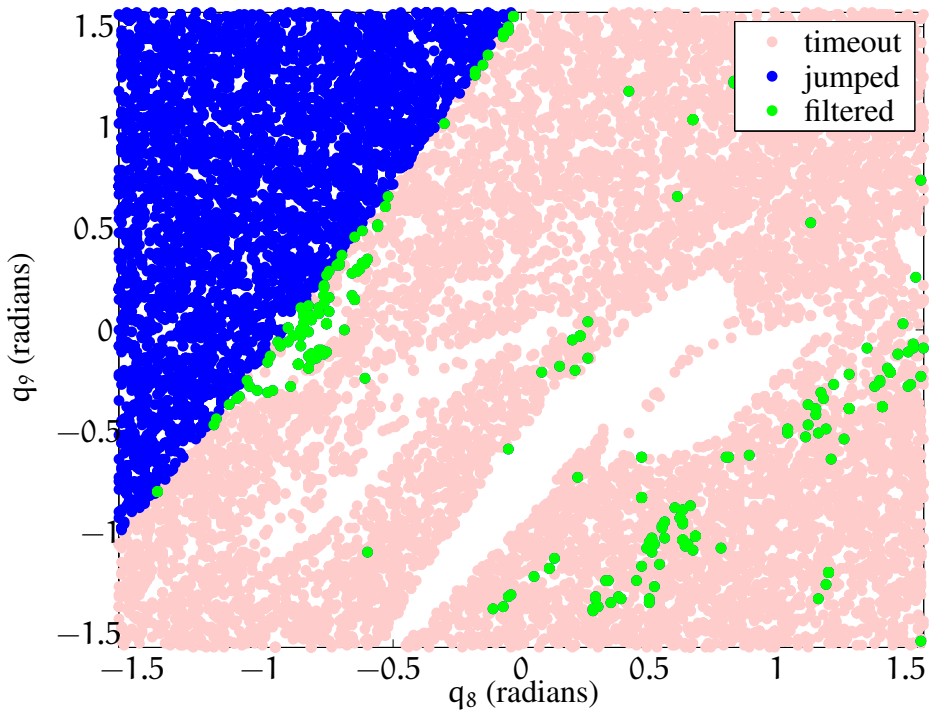

Figure 6.2. Total configuration space sampling.

the initial configuration is less than 200 m/s^2. The majority of the data follow a linear function in this region.

Figure 6.4 details all the quasi-planar configurations of the jumping leg where a jump occurred. The color of the data point corresponds to the duration that the robot remains in contact before leaving the ground during a jump. The size of the data point is related to the acceleration capability of that particular configuration. The acceleration capability of all configurations as shown in Figure 6.1 applies here.

6.4 Configuration Optimization Results

This section presents the results of the configuration optimization discussed in Section 6.2. Initial configurations are given in their respective sections, and all initial velocities

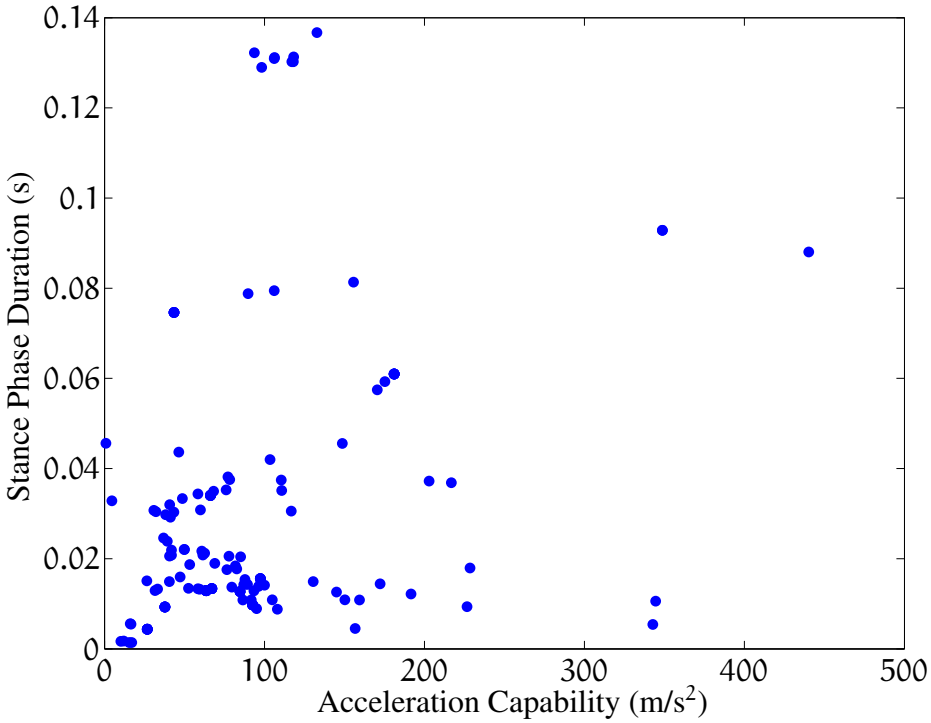

Figure 6.3. Stance phase duration versus acceleration capability.

are zero. The physical properties of the jumping leg are shown in Table 2.3. Parameters of the dynamic simulation of the jumping leg model are given in Table 6.1.

In both simulations, the jumping robot is stabilized to a single point 5 meters away, in the desired direction of the configuration optimization. Control is only active when the mechanism is in contact with the ground. During the flight phase, the robot becomes passive. The absolute position errors of the simulations in Section 6.4.2 and Section 6.4.3 are plotted in Figure 6.5. The optimized configuration tracks towards the fixed goal point better than the arbitrary guess configuration, showing improved performance for the optimized initial configuration. The error plotted in Figure 6.5 is the absolute position error, which is the distance of the center of mass of the body to the goal point. A lower position error corresponds to the robot being closer to the goal.

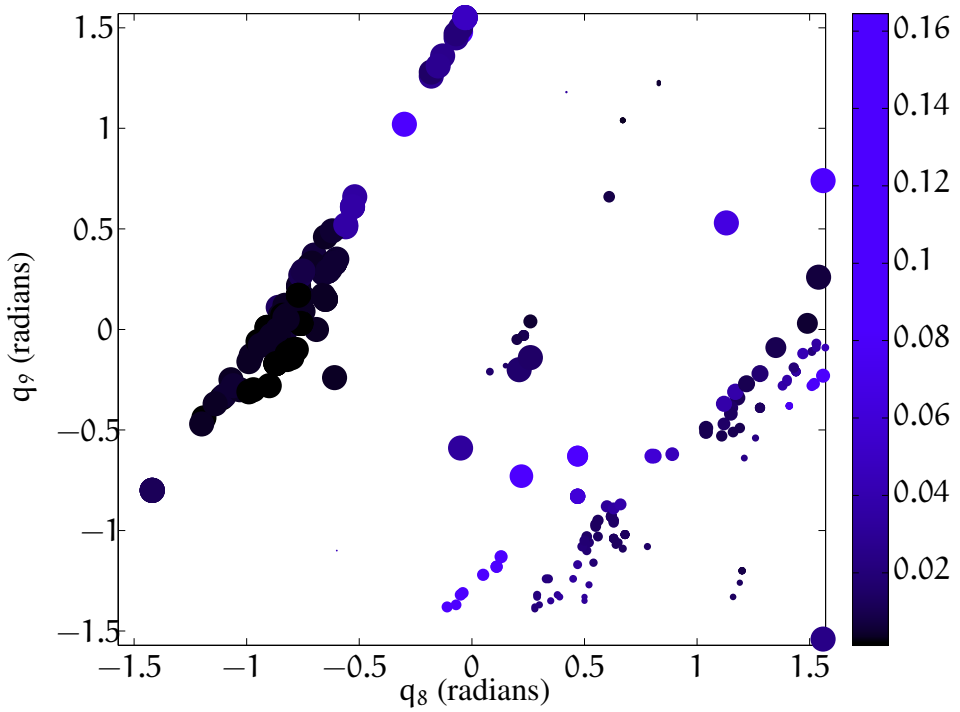

Figure 6.4. Stance phase duration and acceleration capability in the partial configuration space.

6.4.1 Example Optimization

The optimization in (6.7) is used to calculate an optimized initial configuration, given an arbitrary initial guess. A desired jumping direction of

$$[-\cos(\pi/4)N_1, \sin(\pi/4)N_2]\,, \tag{6.12}$$

is used in all cases presented in this section. The configurations for each of the simulations in Section 6.4.2 and Section 6.4.3 are shown in Table 6.2. All values are in radians unless otherwise noted. The initial guess configuration is illustrated in Figure 6.6. The femur and tibia motor angles are chosen intuitively in an effort to maximize the jump performance by bringing the leg under the body. The leg is positioned approximately such that the line from the endpoint of the leg to the center of mass of the body is in the same direction as the desired direction.

Table 6.1. Parameters for jumping leg simulations

Parameter	Symbol	Value
Coefficient of restitution	E	0.0
Energetic coefficient of restitution	e_*	1.0
Static coefficient of friction	μ_s	0.5
Dynamic coefficient of friction	μ_d	0.25
Maximum actuator torque	Υ_{max}	2.5 N-m
Absolute integrator error	E_{abs}	$1e-4$
Relative integrator error	E_{rel}	$1e-3$
Integration step length	t_{int}	0.001 seconds

Table 6.2. Initial and optimized configurations for jumping leg simulations

	q_1	q_2	q_3	q_4	q_5	q_6	q_7	q_8	q_9
Initial guess	0 m	0.17 m	0 m	0	0	0	0	0.09	−0.61
Optimized	0 m	0.18 m	0 m	0.52	−0.5	−0.46	0.15	0.03	0.67

The optimization finds a new initial configuration, as shown in Figure 6.7. The body is rotated, allowing a nonzero angle for the coxa. The acceleration capability is increased by the inclusion of a third actuator into the jump. The initial guess only allows contributions to the jumping motion from the femur and tibia actuators, as the coxa is angled at zero.

6.4.2 Jump with a Non-optimized Initial Configuration

As a benchmark test, the jumping leg robot is simulated with an arbitrary initial configuration guess. The values of the configuration are given in Table 6.2, with the computation time in Table 2.4. The simulated contact forces and actuator torques are presented in Figure 6.8. The mechanism is in contact briefly several times through the run. Actuator torques are near saturation, as there is not enough acceleration capability for an immediate full jump.

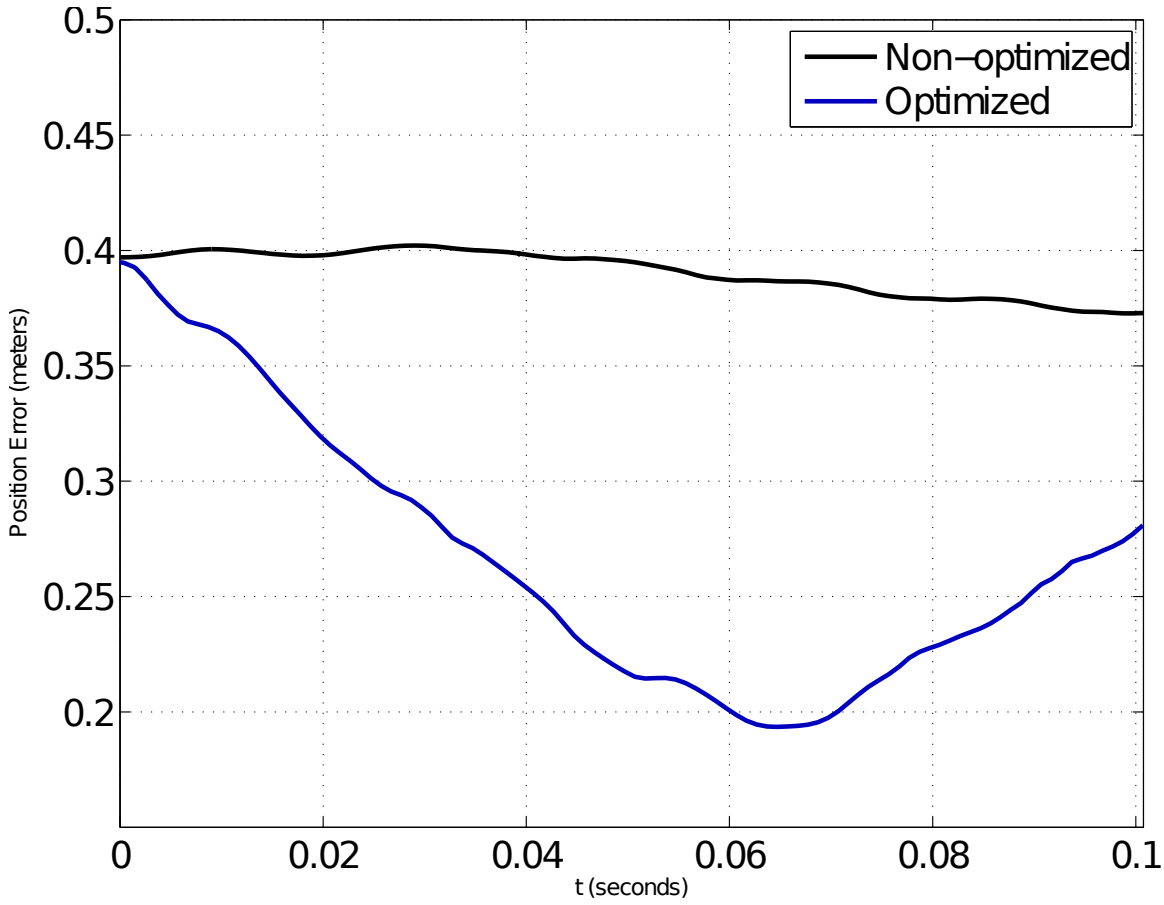

Figure 6.5. Absolute position error for jump simulations..

The simulated motor angles are presented in Figure 6.9. High amplitude oscillations are present, as the joint mounted spring constant is low. The spring rate must be kept low in order to not dominate the actuator torques.

The heights of the body center and leg endpoint versus time are graphed in Figure 6.9. The endpoint leaves the ground several times, but the body center is displaced only 2 centimeters. The joint springs retract the leg, pulling the mechanism out of contact before it can jump. The diminished acceleration capability contributes to this. The trajectory of the body center, projected in the N_1, N_2 plane, is shown in Figure 6.10. The motion

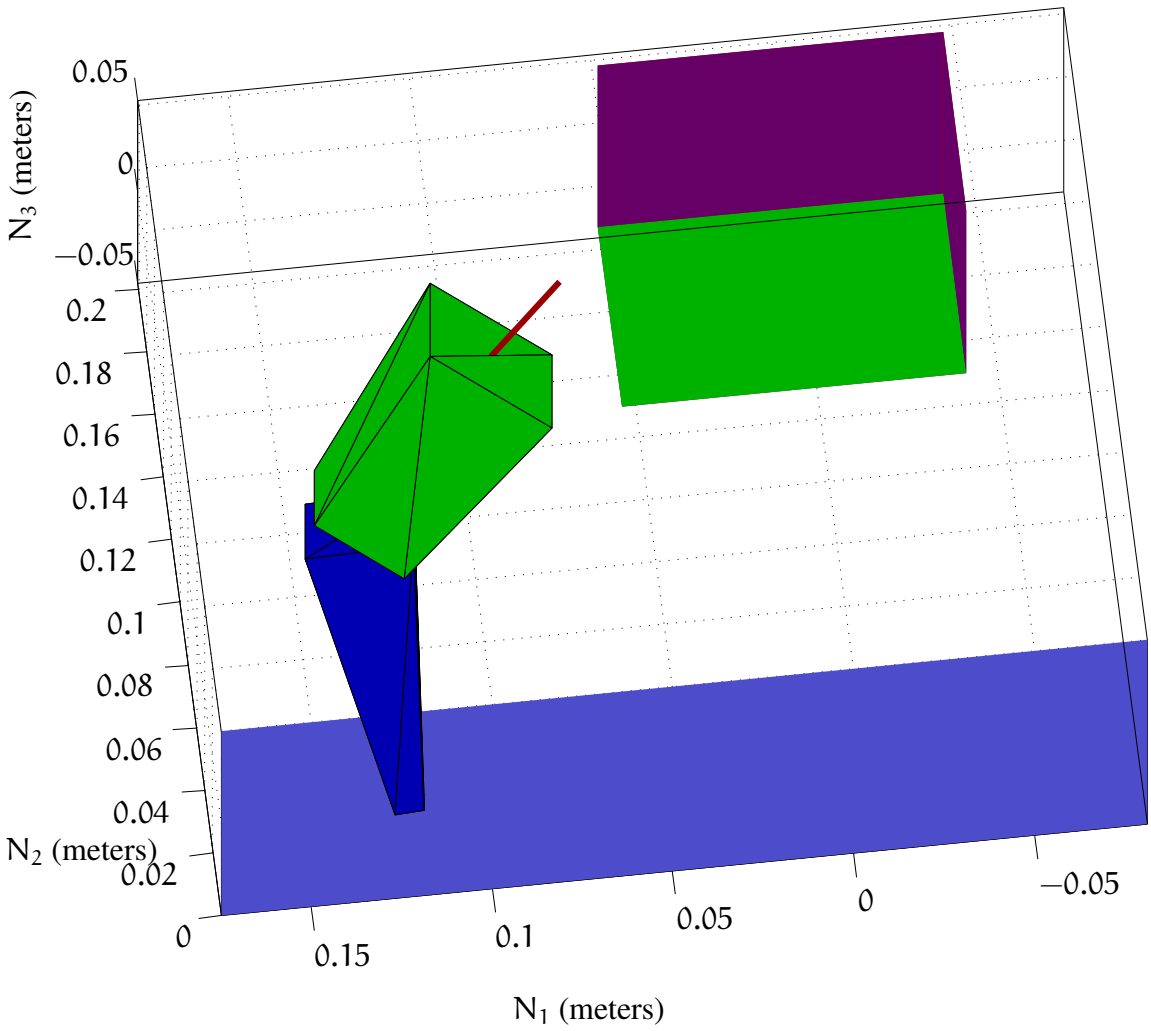

Figure 6.6. Initial, non-optimized configuration of jumping leg mechanism.

initially starts at the left, near $q_1 = 0N_1$, and the mechanism proceeds in $-N_1$ without gaining significant displacement in the vertical direction, N_2.

6.4.3 Jump with an Optimized Initial Configuration

The jumping robot simulation is run with the optimized initial configuration given in Table 6.2. The simulated contact forces and motor torques are plotted in Figure 6.11. The mechanism is in contact only briefly, lifting off the ground immediately.

The motor angles are shown in Figure 6.12. Oscillations are present because of the low spring coefficients. The heights of the body mass center and leg endpoint are given in Figure 6.12. The endpoint leaves the ground and remains airborne for the duration of the simulation. The body center displacement in the vertical direction is approximately 40 centimeters.

The trajectory of the body center, neglecting motion in N_3, is shown in Figure 6.13. The simulated trajectory tracks along the desired direction, with a slight deviation from the parabolic motion of the passive mechanism during the flight phase.

The robot jumping simulations in this section show that an optimized configuration improves the trajectory tracking performance and jumping height. An arbitrary initial guess does not result in a successful jump, even when intuitively chosen to position the robot along the desired line of action. Furthermore, the optimization puts the robot in a configuration that gives a mechanical advantage to all actuators, not just the distal two actuators as in the quasi-planar case.

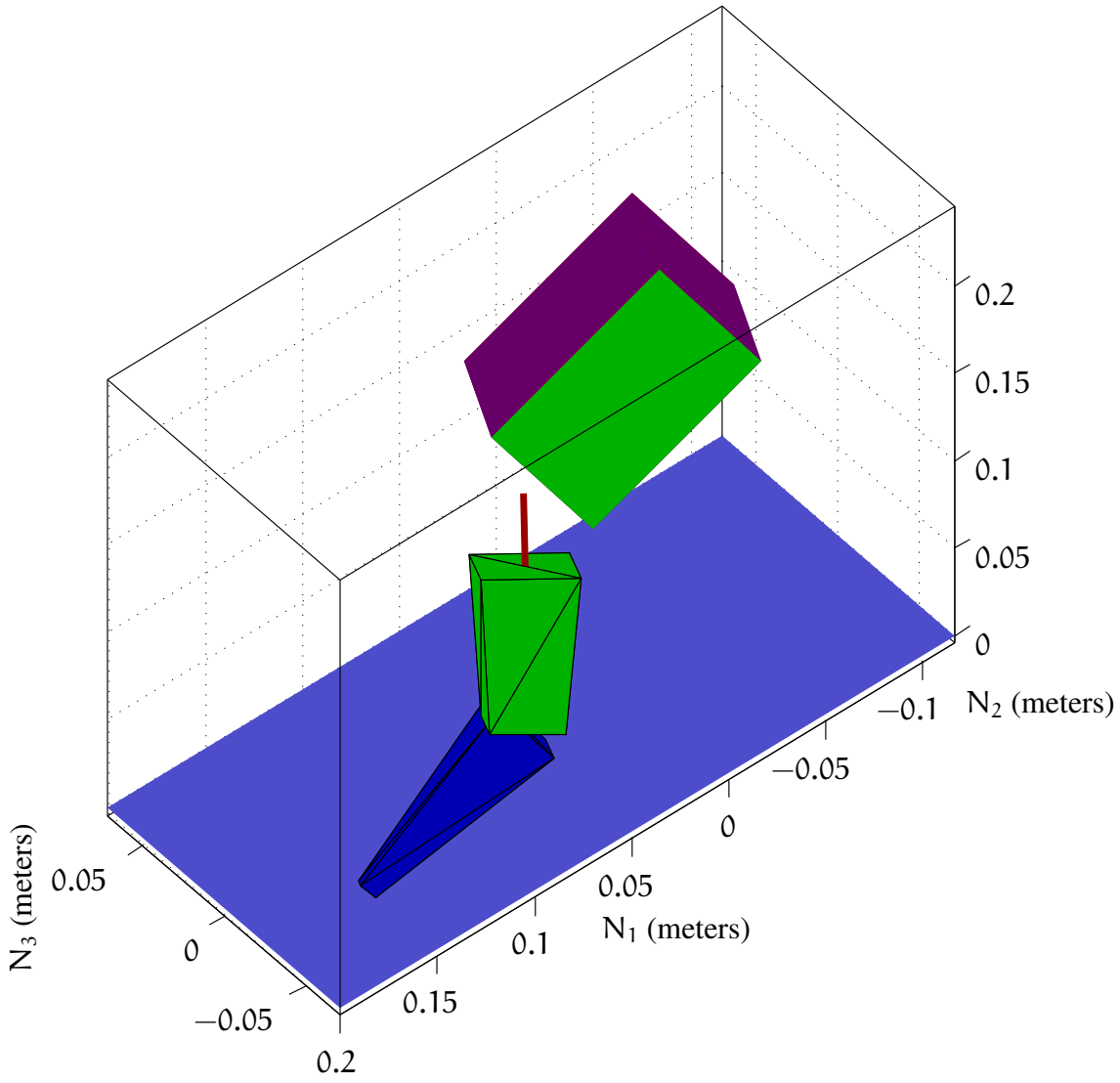

Figure 6.7. Optimized initial configuration of jumping leg mechanism.

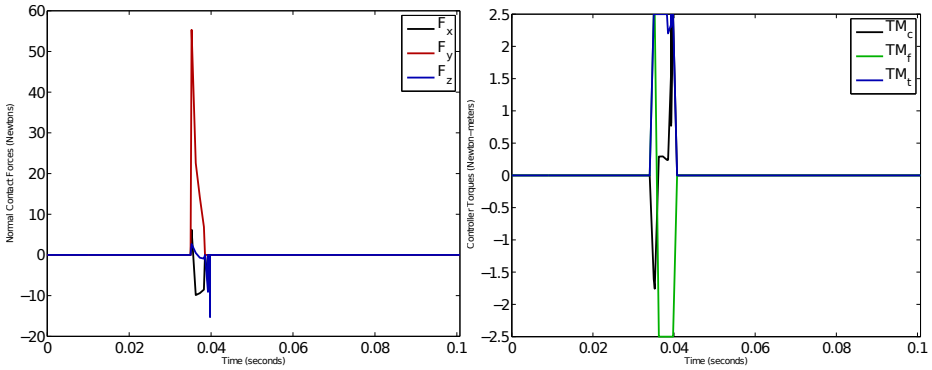

(a) (b)

Figure 6.8. Jump simulation with a non-optimized initial configuration (a) contact forces, (b) motor torques.

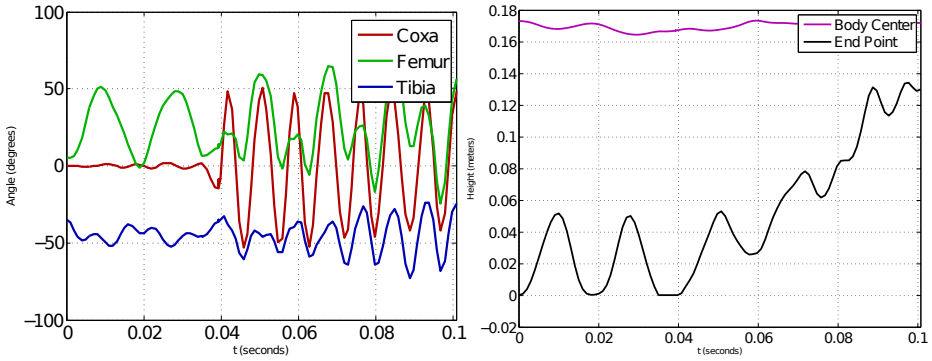

(a) (b)

Figure 6.9. Non-optimized initial configuration (a) motor angles, (b) body center and leg endpoint heights.

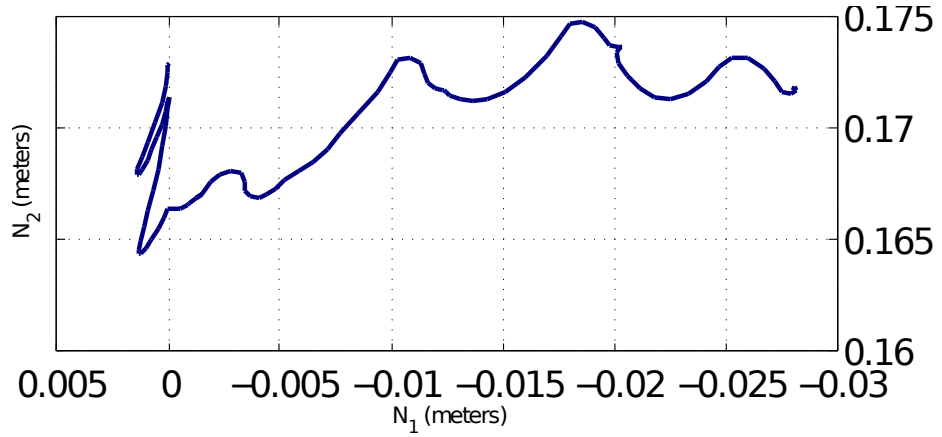

Figure 6.10. Body center trajectory for non-optimized jump simulation.

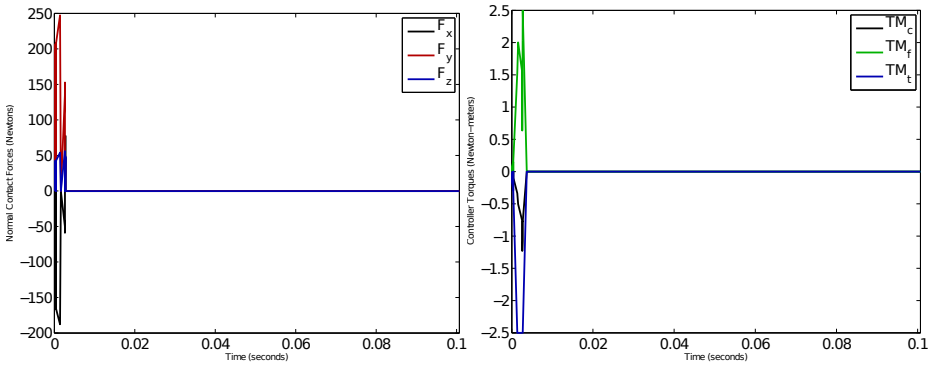

(a) (b)

Figure 6.11. Jump simulation with an optimized initial configuration (a) contact forces, (b) motor torques.

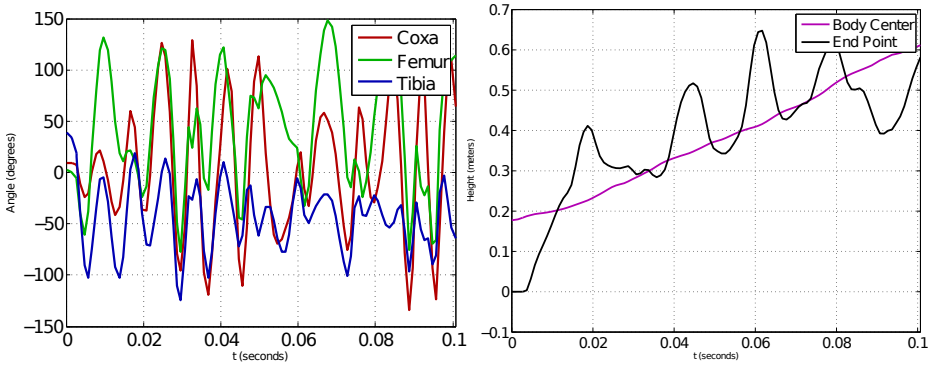

(a) (b)

Figure 6.12. (a) Motor angles, and (b) body center and leg endpoint heights, for optimized jump simulation.

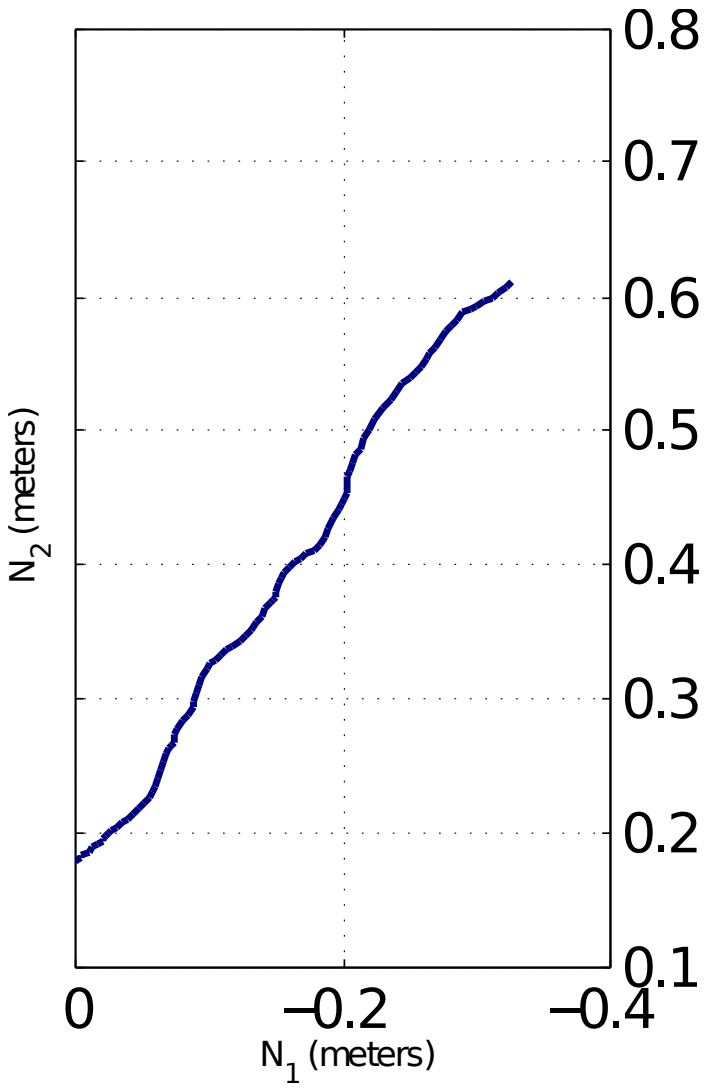

Figure 6.13. Body center trajectory for optimized jump simulation.

CHAPTER 7

CONCLUSION

The study of agility is important in the greater field of research into robot motion. Improvements to robot agility directly improve existing robot locomotion methods. Ground contact interaction is important in the investigation of agility, and was a major focus in this work. Two components of contact modeling were developed here, the modeling of oblique impacts, and energy consistency. Specifically, a new maximum energy dissipation optimization for finding post impact states was used to model oblique impacts. The problem of energy consistency was addressed through a novel method of attenuating post impact generalized speeds, or putting energy as a constraint into the optimization used to initially solve for these speeds.

The contact modeling developed in this work exhibits reasonable behavior and advances the ability to research agility through the simulation of multibody systems. In researching oblique impact, the relationship between feasible coefficients of friction and velocities as related through impulsive forces was discovered. These methods improved the behavior of multibody systems, giving simulations a reasonable approximation of reality.

A system that optimized the initial configuration of a single robot leg to specifically increase its jumping agility was developed to initially investigate agility. Further work into the characterization of configuration and acceleration capability and its impact on stance phase duration was researched, and a preliminary study was performed. It was established that there is a correlation between the acceleration capability of a configuration, and the duration of the stance phase when its used as the initial configuration of a jump. This result directly addressed the original hypothesis that an increase in agility (i.e. acceleration

capability) increases the ground contact duration for a controlled legged mechanism. The research presented herein established the tools required to further research agility in legged robots, and produced preliminary results with which to base further study.

Further investigation into the relationship between acceleration capability and stance phase duration is suggested as future work. The current simulation of the jumping leg robot can be extended to cover the full jumping cycle, not just stance phase. Jumping is only part of agility, and it is recommended to expand study into running, walking, and any other motion with rapidly changing trajectories.

Future work can be performed in relation to the contact modeling and simulation methods used to research agility. The contact model can be expanded to model multiple contacts per body, including situations with indeterminate contact. Alternate friction models can be substituted into the simulation to alter the general behavior, or improve results for different scenarios. The contact model can be modified to consider surface contacts, which introduces contact and impact moments, instead of only forces from point contact. A full contact model considering surface to surface contact, or a full geometric contact model can also be realized. Where polygonal or other geometric models of multiple complex surfaces in multipoint contact and impact can be simulated. Additionally, systems of compliant bodies can also be simulated. All of these models can be used to advance the overall study of agility and how it relates to robots.

APPENDIX A

ANALYSIS OF THE SIMULATION OF A MASS SPRING FRICTION SYSTEM

Several methods of integration are commonly used in the simulation of dynamic systems with friction. In this chapter, two methods of integration are analyzed using a computer simulation of a mass spring damper system, similar to a one degree of freedom model of an automotive suspension. The results in simulation for the two methods are compared, showing that the two integration schemes produce similar results.

A.1 Introduction

Presented here is an analysis of a benchmark dynamic system with friction. Dynamic systems are nonlinear, especially when contact and impact with friction are involved. Large changes in velocity are typical as contact states change. When considering friction it is critical to find when the velocity equals zero in order to assess whether the system will stick or slip in accordance with the Coulomb friction law. These zero velocity events occur at non-regular intervals and it is critical to catch them in order to accurately simulate the behavior predicted by the model. Here two different approaches are used to locate zero velocity events. One uses a linear projection forward in time to estimate when the velocity can be considered equal to zero. The other uses a search scheme that converges to the time of the zero velocity event to within some specified tolerance.

The projection method discussed in [79] is more suited for fixed step integration schemes, as opposed to adaptive ones. This is because adaptive schemes automatically change the step size during the numerical integration, but the current step size is difficult to obtain in order to use it for a projection. In a fixed step integration the step size is constant and thus always known. The search scheme is more suited for adaptive integration because it changes the step size during each iteration in order to locate the zero crossing event to within the specified tolerance. Since the adaptive integration also changes the step size it is easier to combine with the search scheme. In addition, adaptive integration schemes refine

the step size as the system approaches large changes in state, in order to fully capture its fast and slow dynamics [80–83].

The projection method estimates the current acceleration, based upon the friction force, which is multiplied by the fixed step size to obtain the change in velocity to add to the current velocity. This establishes a minimum velocity based on the integration step size to predict that the velocity will likely go to zero during the next integration step. With this prediction, the capture of the point in contact is enforced; where capture is defined as the transition from a sliding to sticking contact state.

Adaptive integrators, such as Matlab's ODE45 [81], include the ability to stop integration at a designated time before the end of a step. Termed event functions, these functions watch for a zero crossing of designated states, and halt integration at the temporal instant of the crossing to within a desired tolerance. While not exact, the adaptive nature of the integrator allows it to stop at the event with a high degree of accuracy.

This chapter is organized as follows: motivations for this work and the methods used are in Section A.3, and simulation results are presented in Section A.4. Concluding remarks are in Section A.5.

A.2 Problem Description

A benchmark system is simulated here to demonstrate that an event based adaptive integration produces results similar to a fixed step integration with prediction of zero crossings of velocity. The two approaches considered herein are discussed in [24] and [79]. The problem developed in this work is similar to a one degree of freedom vehicle model. A large mass is suspended above the ground by a spring and damper system in typical vehicle models. The shape of the ground varies as the vehicle drives over uneven terrain. The displacement of the distal end of the spring is varied to approximate driving over bumps.

The model developed here is the same in that regard, and the only difference between the model used in this work and a vehicle model is that gravity is neglected. That is, the mass spring damper system is on a frictionless horizontal surface. The system is illustrated in Figure A.1.

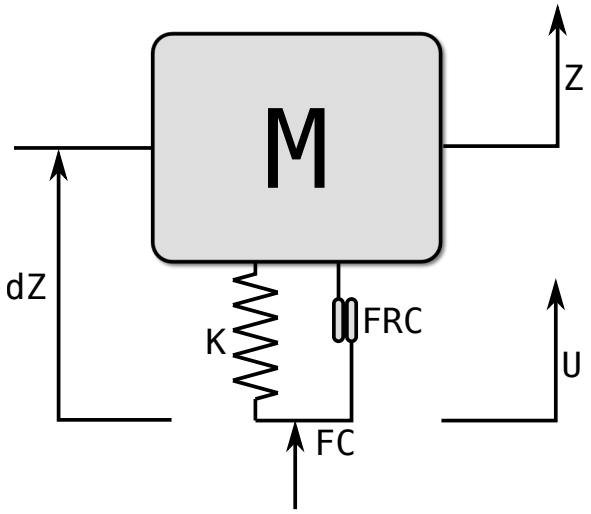

Figure A.1. Mass-Spring-Friction system.

The block is the main object of the diagram, and its mass is denoted as M. The values Z and U are positions of the center of mass of the block and distal end of the spring and damper, respectively. These positions are relative to fixed points in the inertial reference frame. The parameter dZ is the difference between Z and U. The term FRC describes the friction force occurring at the damper. The velocity at this damper is dVs, and K is the spring constant. The forcing function acts on the spring and damper in parallel, and is denoted as FC in Figure A.1. An exciting function displaces the spring directly, which results in a force acting on the block [79]. The parameters of the block system are in Table A.1; all values are from [79]. The integrator parameters are in Table A.2.

Table A.1. System parameters

Parameter	**Name**	**Value**	**Units**
Mass of block	M	1/386	$lbfs^2/in$
Spring constant	K	2	lbf/in
Static coefficient of friction	μ_s	0.3	
Dynamic coefficient of friction	μ_d	0.2	

Table A.2. Integrator parameters

Parameter	**value**
Integration step (total)	0.01
Absolute error	$1.0e-5$
Relative error	$1.0e-4$

A.3 Methods

The dynamic equations of the block system were generated using Autolev [27]. Autolev produced Matlab code that was subsequently modified to add the friction and integration methods. Two integration schemes were used to solve the dynamic equations for the block system. The first integration scheme used was a fixed step size, fourth order Runge-Kutta numerical integrator [79]. The second scheme is a hybrid dynamic approach [22, 24, 25, 69, 75, 84] which uses ODE45, an adaptive step fourth/fifth order integrator provided as part of the Matlab software suite. The adaptive step size simulation presented here used the event function feature to stop and start integration at points in time where the velocity of the friction damper reaches zero.

A Coulomb friction model [24, 82, 85–88] was employed in both simulations presented in this work. This model states that

$$\mu = \mu_s \qquad \text{if } v_t = 0 \tag{A.1}$$

and

$$\mu = \mu_d \qquad \text{if } v_t \neq 0 \tag{A.2}$$

where μ is the coefficient of friction, and μ_s and μ_d are the static and dynamic coefficients of friction respectively.

Complementarity conditions [89] are used in method 2, discussed in more detail in [24, 25, 69, 75]. The conditions govern the post impact velocities and forces of the block as its contact state changes. The friction damper of the block remains in a constant state of contact, and the block itself is on a frictionless surface. The damper transitions between states of sticking and slipping.

The acceleration of the block is computed with the equations of motion, and integrated to solve for velocity and position. The results of this calculation are presented in Section A.4.

A.4 Results

Dynamic systems with friction are chaotic, making integration a challenge. It is difficult to exactly match system states between different simulations, and experimental data. While the simulation is deterministic, small differences in initial conditions, integration setup, and model parameters can cause large changes in the states of a dynamic simulation. The simulation data in the two cases presented herein are similar, though not identical to the original work in [79].

The positions of the block, U, Z, and dZ, are plotted for all cases in Figure A.2. The term dZs appears in the plots in [79], and is synonymous with dZ. Figure A.2a is from [79]. The simulated positions of the block, solved using the fixed step 4^{th} order Runge-Kutta integrator are shown in Figure A.2b. The purpose for the simulation in Figure A.2b is to recreate the data in Figure A.2a using the same computational platform as was used for the simulations obtained using the approach discussed in [22, 24, 25, 69, 75, 84]. The general behavior matches, but the amplitude and position of the peaks is not identical. For

example, the amplitudes of U and Z in the fixed step case in Figure A.2b match the original work from [79]. The difference between these two positions, dZ is also similar. The main cause of these discrepancies is the difference between the estimated forcing function used in Figure A.2b and the original used to generate Figure A.2a. Given these differences, Figure A.2b will be used as the basis for comparison between the different approaches for finding zero crossings.

The simulation shown in Figure A.2c uses the adaptive step size, event driven integration scheme. The exact positions with respect to time change as compared to the fixed step integrator simulation, but the general behavior of the system remains the same. The amplitude of Z is smaller in Figure A.2c, as compared to Figure A.2b. This is because the adaptive integration can determine the length of a stick or slip event with greater temporal resolution, as compared to assuming their duration is a multiple of a fixed time step. In addition, the damper might not stick at each zero crossing, as assumed in the projection approach, and this situation can be determined by using the contact force calculations used in the event function. The maximum displacement of the difference in position dZ is smaller. The forcing function U is identical for both methods.

The slipping and sticking of the damper is investigated in Figure A.3. Plots of the velocity dVs for all cases are included in Figure A.3. dVs is the time derivative of dZ and is represented by the light blue line in Figure A.3a, taken from [79]; dVs equaling zero indicates a zero crossing.

Figure A.3b shows the velocity of the damper, as simulated using the fixed step 4^{th} order Runge-Kutta integrator. The damper velocity in Figure A.3b goes to zero periodically. The zero crossing threshold, as discussed in [79], enforces sticking where the velocity is near zero, but it can miss a crossing if the velocity is too large. Still, the velocity in Figure A.3b has similar characteristics as that in Figure A.3a.

The relative velocity of the damper, as simulated using the adaptive step size, event driven integration scheme, is given in Figure A.3c. In this case, the damper sticks only briefly, resulting in a higher maximum velocity. The damper does stick, but is less likely to stick than in the previous case. The relative velocity of the damper in Figure A.3c remains at zero during the zero crossings for less time as compared to Figure A.3b; the system simulated using the fixed step method sticks more often, and for a longer duration. The velocity of the damper must not necessarily capture, (i.e. stick), at every zero crossing. The zero crossing detection of the first method enforces that the velocity become zero for at least one integrator step, when in fact the velocity of the damper can remain at zero for a smaller length of time. The duration of these events is small because of the adaptive step sizing. In areas where the acceleration is high, the duration of sticking is near instantaneous.

A.5 Conclusion

Two methods of modeling and simulating a sliding block with friction were presented in this paper. The methods were compared in simulation, showing that they produce similar results. Dynamic systems are often chaotic, and producing identical results is difficult, even for trivial benchmark cases. Matching results in simulation is a greater challenge. Although these simulations might not mimic reality, they do predict experimentally observed behaviors in general.

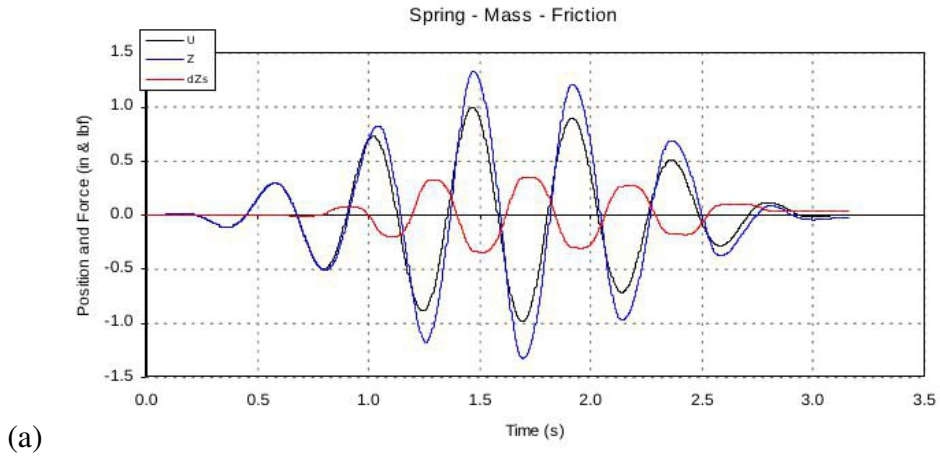

(a)

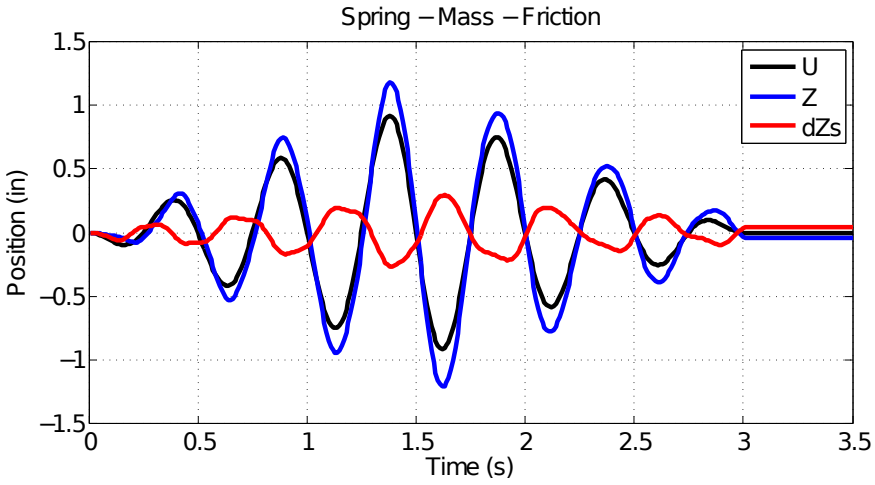

(b)

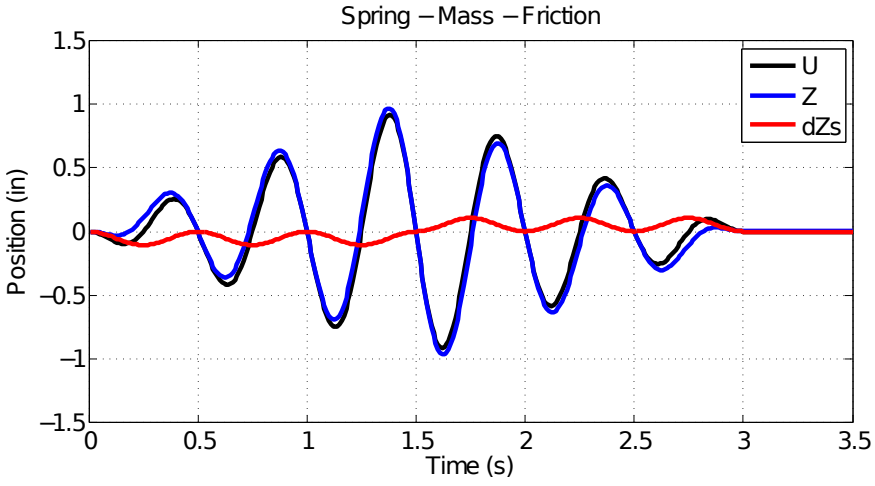

(c)

Figure A.2. Simulated block, (a) original simulation, (b) rk4, and (c) ODE45 integrators..

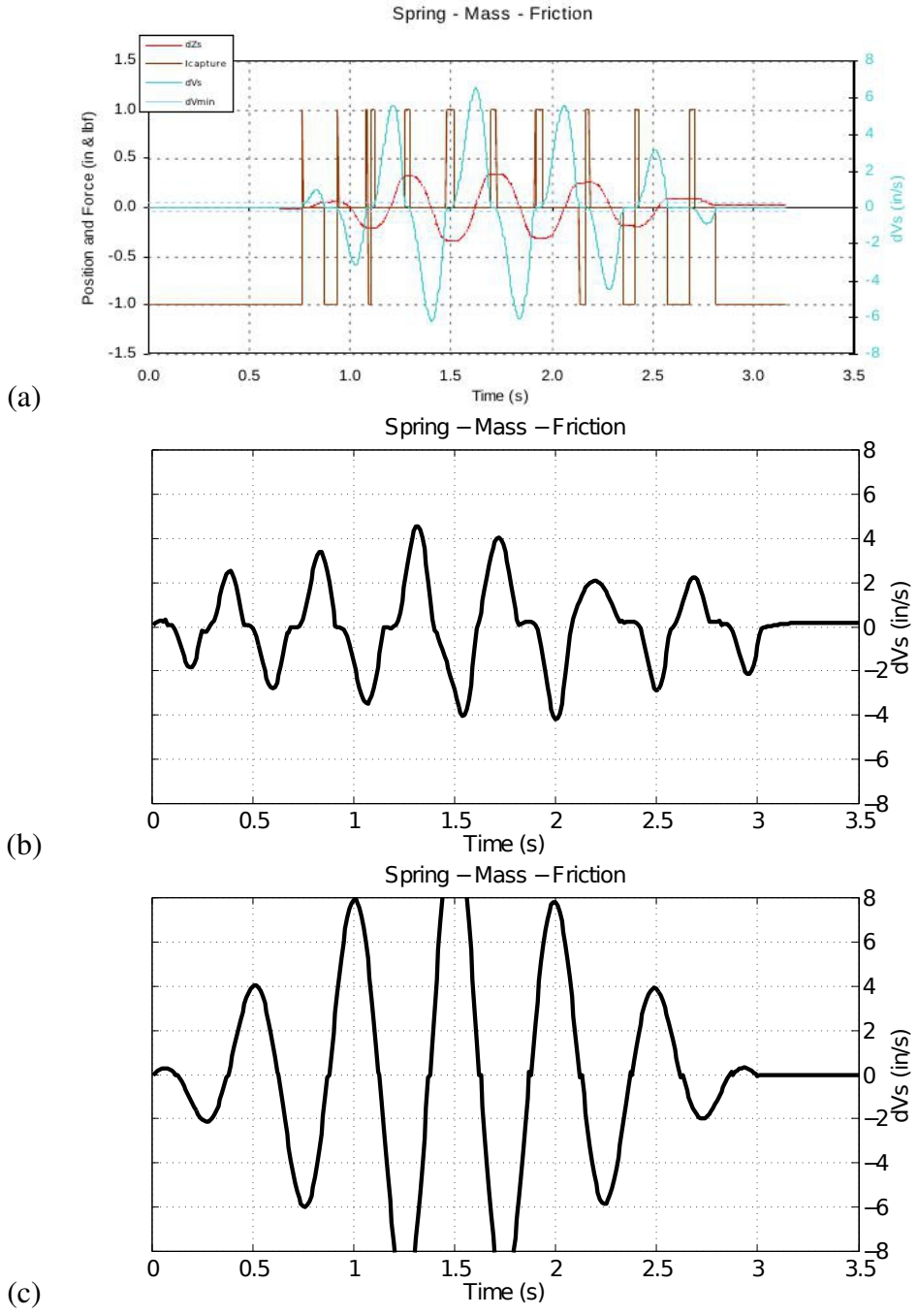

Figure A.3. Simulated block velocity, (a) original simulation, (b) rk4, and (c) ODE45 integrator..

REFERENCES

[1] S. geul Lee and C. hyun Cho, "On-line control algorithm of a quadruped walking robot with quasi-static model," vol. 3, Kyongju, South Korea, 1999, pp. 1645–1650.

[2] S.-H. Park and G.-J. Chung, "Quasi-static obstacle crossing of an animal type four-legged walking machine," *Robotica*, vol. 18, no. 5, pp. 519–533, 2000.

[3] C. C. Phipps, B. E. Shores, and M. A. Minor, "Design and quasi-static locomotion analysis of the rolling disk biped hybrid robot," *IEEE Transactions on Robotics*, vol. 24, no. 6, pp. 1302–1314, 2008.

[4] R. Altendorfer, N. Moore, H. Komsuoglu, M. Buehler, H. B. Brown Jr., D. Mcmordie, U. Saranli, R. Full, and D. E. Koditschek, "RHex: A biologically inspired hexapod runner," *Autonomous Robots*, vol. 11, no. 3, pp. 207–213, 2001.

[5] U. Saranli, M. Buehler, and D. E. Koditschek, "RHex: A simple and highly mobile hexapod robot," *International Journal of Robotics Research*, vol. 20, no. 7, pp. 616–631, 2001.

[6] S. Kim, J. E. Clark, and M. R. Cutkosky, "isprawl: Design and tuning for high-speed autonomous open-loop running," *The International Journal of Robotics Research*, vol. 25, no. 9, pp. 903–912, 2006.

[7] U. Saranli, A. A. Rizzi, and D. E. Koditschek, "Model-based dynamic self-righting maneuvers for a hexapedal robot," *International Journal of Robotics Research*, vol. 23, no. 9, pp. 903–918, 2004.

[8] E. T. Whittaker, *A Treatise on the Analytical Dynamics of Particles and Rigid Bodies*, 2nd ed. Cambridge University Press, 1917.

[9] M. T. Mason and Y. Wang, "On the inconsistency of rigid-body frictional planar mechanics," in *Proceedings of the 1988 IEEE International Conference on Robotics and Automation*, Philadelphia, PA, USA, 1988, pp. 524–528.

[10] W. Stronge, "Unraveling paradoxical theories for rigid body collisions," *Journal of Applied Mechanics, Transactions ASME*, vol. 58, no. 4, pp. 1049–1055, 1991.

[11] B. Brogliato, A. ten Dam, L. Paoli, F. Génot, and M. Abadie, "Numerical simulation of finite dimensional multibody nonsmooth mechanical systems," *Applied Mechanics Reviews*, vol. 55, no. 2, pp. 107–149, Mar. 2002.

[12] G. Gilardi and I. Sharf, "Literature survey of contact dynamics modelling," *Mechanism and Machine Theory*, vol. 37, no. 10, pp. 1213–1239, Oct. 2002.

[13] S. Djerassi, "Collision with friction; part A: Newton's hypothesis," *Multibody System Dynamics*, vol. 21, no. 1, pp. 37–54, 2009.

[14] ——, "Collision with friction; part B: Poisson's and stornge's hypotheses," *Multibody System Dynamics*, vol. 21, no. 1, pp. 55–70, 2009.

[15] ——, "Stronge's hypothesis-based solution to the planar collision-with-friction problem," *Multibody System Dynamics*, vol. 24, no. 4, pp. 493–515, 2010.

[16] A. Gollu and P. Varaiya, "Hybrid dynamical systems," vol. 3, Tampa, FL, USA, 1989, pp. 2708–2712.

[17] R. B. Gillespie, V. Patoglu, I. I. Hussein, and E. R. Westervelt, "On-line symbolic constraint embedding for simulation of hybrid dynamical systems," *Multibody System Dynamics*, vol. 14, no. 3-4, pp. 387–417, Nov. 2005.

[18] D. Baraff, "Analytical methods for dynamic simulation of non-penetrating bodies," *Computer Graphics*, vol. 23, no. 3, pp. 223–232, July 1989.

[19] F. Pfeiffer and C. Glocker, *Multibody Dynamics with Unilateral Contacts*, ser. Wiley Series in Nonlinear Science. John Wiley & Sons, Inc., 1996.

[20] C. Glocker and C. Studer, "Formulation and preparation for numerical evaluation of linear complentarity systems in dynamics," *Multibody System Dynamics*, vol. 13, no. 4, pp. 447–463, May 2005.

[21] I. Sharf and Y. Zhang, "A contact force solution for non-colliding contact dynamics simulation," *Multibody System Dynamics*, vol. 16, no. 3, pp. 263–290, Oct. 2006.

[22] D. M. Flickinger and A. Bowling, "Impact forces in the simulation of simultaneous impacts and contacts in multibody systems with friction," in *Proceedings of the IEEE/RSJ International Conference on Intelligent Robots and Systems (IROS)*, Oct. 2009.

[23] J. J. Craig, *Introduction to Robotics: Mechanics and Control*, 2nd ed. Addison-Wesley Publishing Company, 1989.

[24] A. Bowling, D. M. Flickinger, and S. Harmeyer, "Energetically consistent simulation of simultaneous impacts and contacts in multibody systems with friction," *Multibody System Dynamics*, vol. 22, no. 1, pp. 27–45, Aug. 2009.

[25] D. M. Flickinger and A. Bowling, "Simultaneous oblique impacts and contacts in multibody systems with friction," *Multibody System Dynamics*, vol. 23, no. 3, pp. 249–261, Mar. 2010.

[26] D. E. Stewart, "Rigid-body dynamics with friction and impact," *SIAM Review*, vol. 42, no. 1, pp. 3–39, 2000.

[27] D. Levinson, "Use of AUTOLEV for kinematical analysis of robots," *AIAA Guidance, Navigation and Control Conference*, pp. 644–644, 1990.

[28] C. Glocker, "An introduction to impacts," in *Nonsmooth Mechanics of Solids*, ser. CISM Courses and Lectures. Springer-Verlag, Wien, New York, 2006, vol. 485, pp. 45–102.

[29] J. C. Trinkle, "Formulation of multibody dynamics as complementarity problems," vol. 5 A, Chicago, IL, United states, 2003, pp. 361–370.

[30] G. Gilardi and I. Sharf, "Literature survey of contact dynamics modeling," *Mechanism and Machine Theory*, vol. 37, no. 10, pp. 1213–1239, March 2002.

[31] H. M. Lankarani and P. E. Nikravesh, "A contact force model with hysterisis damping for impact analysis of multibody systems," *Journal of Mechanical Design, Transactions of the ASME*, vol. 112, pp. 369 – 376, September 1990.

[32] Y. Gonthier, J. Mcphee, C. Lange, and J. PiedbŒuf, "A regularized contact model with asymmetric damping and dwell-time dependent friction," *Multibody System Dynamics*, vol. 11, no. 3, pp. 209–233, Apr. 2004.

[33] P. Flores, J. Ambròsio, and J. P. Claro, "Dynamic analysis for planar multibody mechanical systems with lubricated joints," *MultiBody System Dynamics*, vol. 12, no. 1, pp. 47–74, Aug. 2004.

[34] W. J. Stronge, "Friction in collisions: Resolution of a paradox," *Journal of Applied Physics*, vol. 69, pp. 610–612, January 1991.

[35] ——, *Impact Mechanics*. Cambridge University Press, 2000, pp. 173-200.

[36] R. Brach, "Friction, restitution, and energy loss in planar collisions," *Journal of Applied Mechanics, Transactions of the ASME*, vol. 51, no. 1, pp. 164–170, March 1984.

[37] ——, *Mechanical Impact Dynamics: Rigid Body Collisions*. John Wiley & Sons, 1991.

[38] ——, "Formulation of rigid body impact problems using generalized coordinates," *International Journal of Engineering Science*, vol. 36, no. 1, pp. 61–71, January 1998.

[39] B. Brogliato, *Nonsmooth Mechanics: Models, Dynamics and Control*. Springer-Verlag London Limited, 1999, p. 128.

[40] V. Becker and T. Schwager, "Coefficient of tangential restitution for the linear dashpot model," *Physical Review E*, vol. 77, no. 1, pp. 011 304–1 – 011 304–12, January 2008.

[41] P. Flores, J. Ambrosio, J. C. P. Claro, and H. M. Lankarani, "Influence of the contact-impact force model on the dynamic response of multi-body systems," *Proceedings*

of the Institution of Mechanical Engineers, Part K: Journal of Multi-body Dynamics, vol. 220, no. 1, pp. 21–34, 2006.

[42] S. A. Modarres Najafabadi, J. Kovecses, and J. Angeles, "Impacts in multibody systems: Modeling and experiments," *Multibody System Dynamics*, vol. 20, no. 2, pp. 163–176, 2008.

[43] B. Brogliato, *Nonsmooth Mechanics: Models, Dynamics and Control*, 2nd ed. Springer-Verlag London Limited, 1999.

[44] D. Karnopp, "Computer simulation of stick-slip friction in mechanical dynamic systems," *Journal of Dynamic Systems, Measurement and Control, Transactions of the ASME*, vol. 107, no. 1, pp. 100–103, Mar. 1985.

[45] D. A. H. Jr. and B. Friedland, "On the modeling and simulation of friction," *Journal of Dynamic Systems, Measurement and Control, Transactions of the ASME*, vol. 113, no. 3, pp. 354–362, Sept. 1991.

[46] I. Han and B. J. Gilmore, "Multi-body impact motion with friction-analysis, simulation, and experimental validation," *Journal of Mechanical Design, Transactions of the ASME*, vol. 115, no. 3, pp. 412–422, Sept. 1993.

[47] T. Mouri, T. Yamada, A. IWAI, N. Mimura, and Y. Funahashi, "Identification of contact conditions from contaminated data of contact force and moment," in *Proceedings IEEE International Conference on Robotics and Automation*, vol. 1, May 2001, pp. 597–603.

[48] A. Bowling, "Dynamic performance, mobility, and agility of multi-legged robots," *ASME Journal of Dynamic Systems, Measurement and Control, Transactions of the ASME*, vol. 128, no. 4, pp. 765–777, Dec. 2006.

[49] K. Youcef-Toumi and D. A. Gutz, "Impact and force control: Modeling and experiments," *Journal of Dynamic Systems, Measurement, and Control, Transactions of the ASME*, vol. 116, no. 1, pp. 89–98, March 1994.

[50] H. Baruh, *Analytical Dynamics*, 1st ed. WCB MacGraw-Hill, 1999.

[51] J. J. Moreau, "Numerical aspects of the sweeping process," *Computer Methods in Applied Mechanics and Engineering*, vol. 177, no. 3-4, pp. 329 – 349, July 1999.

[52] T. Liu, M. Y. Wang, and K. H. Low, "Non-jamming conditions in multi-contact rigid-body dynamics," *Multibody System Dynamics*, vol. 22, no. 3, pp. 269–295, Oct. 2009.

[53] D. Stoianovici and Y. Hurmuzlu, "A critical study of the applicability of rigid body collision theory," *ASME Journal of Applied Mechanics*, vol. 63, no. 2, pp. 307–316, June 1996.

[54] Y. Hurmuzlu, "An energy based coefficient of restitution for planar impacts of slender bars with massive external surfaces," *ASME Journal of Applied Mechanics*, vol. 65, no. 4, pp. 952–952, December 1998.

[55] H.-J. Kim, W.-S. Yoo, J.-K. Ok, and D.-W. Kang, "Parameter identification of damping models in multibody dynamic simulation of mechanical systems," *Multibody System Dynamics*, June 2009.

[56] J. Ambrósio and P. Verissimo, "Improved bushing models for general multibody systems and vehicle dynamics," *Multibody System Dynamics*, June 2009.

[57] Y. Aoustin and A. Formal'Skii, "Ball on a beam: Stabilization under saturated input control with large basin of attraction," *Multibody System Dynamics*, vol. 21, no. 1, pp. 71–89, 2009.

[58] P. R. Dahl, "SOLID FRICTION DAMPING OF MECHANICAL VIBRATIONS." *AIAA Journal*, vol. 14, no. 12, pp. 1675–1682, 1976.

[59] C. Canudas de Wit, H. Olsson, K. J. Astrom, and P. Lischinsky, "A new model for control of systems with friction," *Automatic Control, IEEE Transactions on*, vol. 40, no. 3, pp. 419–425, Mar. 1995.

[60] H. Olsson, K. J. Astrom, C. C. D. Wit, M. Gafvert, and P. Lischinsky, "Friction models and friction compensation," *European Journal of Control*, vol. 4, no. 3, pp. 176–195, 1998.

[61] J. Swevers, F. A. Bender, C. G. Ganseman, and T. Prajogo, "Integrated friction model structure with improved presliding behavior for accurate friction compensation," *IEEE Transactions on Automatic Control*, vol. 45, no. 4, pp. 675–686, 2000.

[62] P. Dupont, B. Armstrong, and V. Hayward, "Elasto-plastic friction model: contact compliance and stiction," vol. 2, Chicago, IL, USA, 2000, pp. 1072–1077.

[63] P. Dupont, V. Hayward, B. Armstrong, and F. Altpeter, "Single state elastoplastic friction models," *IEEE Transactions on Automatic Control*, vol. 47, no. 5, pp. 787–792, 2002.

[64] V. Lampaert, J. Swevers, and F. Al-Bender, "Modification of the leuven integrated friction model structure," *IEEE Transactions on Automatic Control*, vol. 47, no. 4, pp. 683–687, 2002.

[65] F. Al-Bender, V. Lampaert, and J. Swevers, "The generalized maxwell-slip model: A novel model for friction simulation and compensation," *IEEE Transactions on Automatic Control*, vol. 50, no. 11, pp. 1883–1887, 2005.

[66] V. Hayward, B. S. R. Armstrong, F. Altpeter, and P. E. Dupont, "Discrete-time elasto-plastic friction estimation," *IEEE Transactions on Control Systems Technology*, vol. 17, no. 3, pp. 688–696, 2009.

[67] Y. Hurmuzlu and D. B. Marghitu, "Rigid body collisions of planar kinematic chains with multiple contact points," *The International Journal of Robotics Research*, vol. 13, pp. 82–92, February 1994.

[68] D. B. Marghitu and Y. Hurmuzlu, "Three-dimensional rigid body collisions with multiple contact points," *ASME Journal of Applied Mechanics*, vol. 62, pp. 725–732, March 1994.

[69] A. Bowling, D. M. Flickinger, and S. Harmeyer, "Energetically consistent collisions in the simulation of multibody systems," in *Proceedings IEEE International Conference on Robotics and Automation (ICRA)*, May 2009, pp. 4049–4056, kobe, Japan.

[70] B. Brogliato, *Nonsmooth Mechanics: Models, Dynamics and Control*. Springer-Verlag London Limited, 1999, p. 198.

[71] W. Yao, B. Chen, and C. Liu, "Energetic coefficient of restitution for planar impact in multi-rigid-body systems with friction," *International Journal of Impact Engineering*, vol. 31, no. 3, pp. 255–265, Mar. 2005.

[72] Q. Guo, C. J. B. MacNab, and J. K. Pieper, "Hopping on even ground and up stairs with a single articulated leg," *Journal of Intelligent and Robotic Systems: Theory and Applications*, vol. 53, no. 4, pp. 331–358, 2008.

[73] Q. Guo, C. Macnab, and J. Pieper, "Hopping with nearly-passive flight phases," Chengdu, China, 2008, pp. 743–748.

[74] L. R. Palmer, D. E. Orin, D. W. Marhefka, J. P. Schmiedeler, and K. J. Waldron, "Intelligent control of an experimental articulated leg for a galloping machine," vol. 3, Taipei, Taiwan, 2003, pp. 3821–3827.

[75] D. M. Flickinger and A. Bowling, "Simultaneous oblique impacts and contacts in multibody systems with friction," in *Proceedings of the IEEE/ASME International Conference on Advanced Intelligent Mechatronics (AIM)*, July 2009, pp. 1613–1618, Singapore.

[76] A. Bowling and O. Khatib, "Robot acceleration capability: The actuation efficiency measure," in *Proceedings of the IEEE Conference on Robotics and Automation*, vol. 4, Apr. 2000, pp. 3970–3975, San Francisco, California, USA.

[77] A. Bowling and S. Harmeyer, "Dynamic performance as a criterion for redundant manipulator control," *ASME Journal of Dynamic Systems, Measurement and Control, Transactions of the ASME*, 2006, In progress.

[78] A. Bowling and O. Khatib, "The dynamic capability equations: A new tool for analyzing manipulator dynamic performance," *IEEE Transactions on Robotics*, vol. 21, no. 1, pp. 115–123, Feb. 2005.

[79] B. Woods, "Coulomb friction between two moving bodies including static and dynamic motion," Feb. 2005, unpublished.

[80] G. M. Hulbert and I. Jang, "Automatic time step control algorithms for structural dynamics," *Computer Methods in Applied Mechanics and Engineering*, vol. 126, no. 1-2, pp. 155–178, 1995.

[81] L. F. Shampine and M. W. Reichelt, "The MATLAB ODE suite," *SIAM Journal on Scientific Computing*, vol. 18, no. 1, pp. 1–1, 1997.

[82] D. Stewart and J. C. Trinkle, "Implicit time-stepping scheme for rigid body dynamics with coulomb friction," vol. 1, San Francisco, CA, USA, 2000, pp. 162–169.

[83] S. Chen and D. A. Tortorelli, "An energy-conserving and filtering method for stiff nonlinear multibody dynamics," *Multibody System Dynamics*, vol. 10, no. 4, pp. 341–362, 2003.

[84] D. M. Flickinger and A. Bowling, "Coupling of the coefficient of restitution and coulomb friction under rigid impacts with varying incidence angle and tangential velocity," in *Proceedings of Multibody Dynamics*, June 2009.

[85] F. JL and B. DE, "SIMULATION OF A MOBILE EQUIPMENT HYDRAULIC CONTROL SYSTEM," *ASME*, 1969.

[86] J. R. Knibloe and R. H. Wagoner, "Experimental investigation and finite element modeling of hemispherically stretched steel sheet," *Metallurgical transactions. A, Physical metallurgy and materials science*, vol. 20 A, no. 8, pp. 1509–1521, 1989.

[87] M. J. Saran and R. H. Wagoner, "Consistent implicit formulation for nonlinear finite element modeling with contact and friction. part I. theory," *Journal of Applied Mechanics, Transactions ASME*, vol. 58, no. 2, pp. 499–506, 1991.

[88] W. Son, K. Kim, N. M. Amato, and J. C. Trinkle, "A generalized framework for interactive dynamic simulation for multirigid bodies," *IEEE Transactions on Systems, Man, and Cybernetics, Part B: Cybernetics*, vol. 34, no. 2, pp. 912–924, 2004.

[89] J.-S. Pang and J. Trinkle, "Complementarity formulations and existence of solutions of dynamic multi-rigid-body contact problems with coulomb friction," *Mathematical Programming*, vol. 73, pp. 199–226, 1996.

BIOGRAPHICAL STATEMENT

Daniel Montrallo Flickinger, a product of the 1980s, grew up in Chatsworth, California. Starting college at age 16, he began studying computer science, and then mechanical engineering at the University of Utah in Salt Lake City. Daniel married Mable Richey in 2000, and graduated with a Bachelors in Science in Mechanical Engineering in 2003.

Continuing at the University of Utah, Daniel specialized in trajectory planning, coordination and autonomous teleoperation of multiple mobile robots, and completed a Masters of Science in Mechanical Engineering in 2006. After a two year detour at the University of Notre Dame, Daniel and Mable settled in Arlington, Texas in 2008. His daughter, Oriana, was born in 2009. Furthering his studies in Mechanical Engineering, Daniel completed a PhD in Mechanical Engineering from the University of Texas at Arlington in 2011.

Daniel's favorite pizza is pineapple-mushroom, favorite engine is the Mercedes-Benz OM617, and favorite Muppet is Waldorf.